Adsorption, Field Adsorption, and Field Evaporation

by

Kashi Nath

Submitted in partial fulfillment of the requirements

for the degree of Doctor of Philosophy

at

Dalhousie University

Halifax, Nova Scotia, Canada

Fall, 1986

TO MY PARENTS

TABLE OF CONTENTS

LIST OF FIGURES AND TABLES

ABSTRACT

The van der Waals constants C_3 and the coefficients for the long range part of the substrate-mediated dispersion energy between two identical adparticles have been calculated for the rare gases and hydrogen on 20 semiconductors, using the experimental data for their dynamic dielectric functions.

The adsorption of the rare gas atoms on metal surfaces can be greatly enhanced by strong electric fields, such as those occurring at field ion emission tips. The field induced charge transfer can be so large that above critical fields of several volts per angstrom desorption of positively charged rare gas ions, such as He^+, Ne^+, Ne^{++}, etc., occurs. An ASED-MO (Atom Superposition and Electron Delocalization-Molecular Orbital) cluster programme, suitably modified to include electric field effects, has been used to calculate potential energy curves, binding and activation energies, bond-lengths, and charge transfers of He, Ne, and Ar field-adsorbed on a W(111) surface.

The one-electron potential energy is also evaluated to facilitate the calculation of the ionization probabilities and eventually the ion yield at the field ion emission tip. A detailed procedure to calculate three-centre Coulomb integrals over the Slater orbitals is given for this purpose.

Adsorption, field adsorption, dissociation, etc., of H_2 and H_3 onto W(111) have also been studied. The most probable configuration and the adsorption site have been found. Vibrational frequencies are determined for the adsorbed species as a function of electric field strength.

In very strong fields, the field ion tips themselves evaporate. Effects of field penetration, Friedel oscillations, polarization, and hyperpolarization are investigated.

ACKNOWLEDGEMENTS

The work presented in this thesis was carried out under the supervision of Dr. H. J. Kreuzer. I would like to express my sincere gratitude to him for his valuable and generous guidance. His interest and encouragement throughout have been greatly appreciated.

It is pleasure to acknowledge the help of Dr. Z. W. Gortel for discussions on the theory of semiconductors, and of Dr. A. B. Anderson for discussions on the analysis of the molecular orbitals and for the ASED-MO computer code.

Thanks are also due to Drs. D. J. W. Geldart, S. H. Payne, G. Gumbs, R. J. Boyd, D. Tomanek and J. Peters for many useful discussions and help with various matters.

The pleasant and friendly environment of the Physics Department at Dalhousie has been very much appreciated. Mrs. R. Allen and Mrs. B. Trim have been very helpful during the preparation of this manuscript. The Dalhousie Computer Centre has been generous in allocating computer time.

Finally, I am grateful to my wife Meena for her patience, help and encouragement during the time devoted to this project.

This work was carried out with the financial assistance of a Dalhousie Killam Memorial Fellowship.

INTRODUCTION

A brief account of the contents of this thesis is given in this introduction. Each chapter starts with a separate and detailed introduction. Part of the thesis is based on the recent work by Nath et al.[1-6]

In the last decade there has been increasing use of rare gases as probes of surface structure, reconstruction, defects, etc. Helium scattering and field ion microscopy are just two examples involving these gas atoms.

The long range attractive part of the interaction between a physisorbed gas atom and a solid is given by the van der Waals dispersion force, for which the energy of interaction is inversely proportional to the cube of the separation between the surface and the adsorbed particle (Dzyaloshinskii, Lifshitz and Pitaevskii, Ref.6, Chap.I), the proportionality constant being known as C_3. In this work, C_3 and the van der Waals constants for the long range part of the substrate-mediated dispersion energy (McLachlan, Ref.10, Chap.I) between two identical adparticles have been calculated for the rare gases and hydrogen on 20 semiconductors. The dynamic dielectric function used for this purpose has been calculated from the measured reflectivity data using a Kramers-Kronig analysis. For the dynamic polarizability of the adparticles, an approximate expression, given by Langhoff and Karplus (Ref.60, Chap.I), has been used. The results obtained for these van der Waals constants are similar to those for the metals and graphite. C_3 and other van der Waals constants help estimate the binding energy and equilibrium distance for the adsorbing particle on the substrate, provided one knows the repulsive part of the surface potential. The latter can be calculated by summing the two-body repulsion energy between the adparticle and the substrate atoms.

The field ion microscope (FIM) uses rare gases, ionized in strong fields, to image the surface atoms of the solids (see for example Müller and Tsong, Ref.1, Chap.III). Theory is not adequate to explain the adsorption phenomena of these gases in strong electric fields. An ASED-MO (Atom Superposition and Electron Delocalization - Molecular Orbital) cluster calculation of Anderson (Ref.15-18, Chap.II) has been used, in the present work, to obtain the binding energies, the bond-lengths and the charge transfers (in terms of the Mulliken (Ref.30, Chap.II) definition) of the adsorbed species on the metal. The results for the binding energies thus obtained are comparable to those obtained using the van der Waals constants C_3. The ASED-MO programme has been suitably modified, for the first time, to include the field effects such as the penetration of the field, Friedel oscillations, polarization, hyperpolarization (Forbes, Ref.4, Chap.II), etc. It is found that the activation energy increases many-fold in the presence of strong electric fields of several volts per angstrom and at the same time there is a considerable charge transfer to the adsorbed species. The distance of the (local) equilibrium position decreases about 30% before the activation energy barrier disappears completely at higher field strengths. The mixing of the p-orbitals of the rare gases (empty for He, and occupied for Ne and Ar) and the (partially occupied) d-band of the transition metal (tungsten) is one of the factors responsible for the binding of the rare gases on this metal. The increase in the total energy due to the unoccupied destabilizing orbitals has been taken care of by the two-body repulsion energy. ASED-MO is a modification of the extended Hückel molecular orbital theory (essentially due to Hoffmann (Ref.22, Chap.II)) mainly in the sense that the ASED-MO takes into account the electrostatic Coulomb repulsion due to the nuclei of the cluster atoms. The penetration of the field is based on the jellium model calculations of Schmickler and Henderson (Ref.27, Chap.II), of Gies and Gerhardts (Ref.28, Chap.II), and of Lang and Kohn (Ref.37, Chap.II). Their calculations are based directly on the Hohenberg-Kohn-Sham (Ref.36, Chap.II) density functional theory.

The one-electron potential energy curve has been obtained for a rare gas atom field-adsorbed on a tungsten cluster in order to consider WKB electron tunnelling rates (from the adatom to the cluster). The present calculations are compared to the results of model calculations which use a simple Coulomb-like potential for the adsorbed atom (Haydock and Kingham, Ref.10, Chap.II). Several three-centre Coulomb integrals are required for this purpose since the Slater orbitals (used as the basis function in the ASED-MO) are centered around different nuclei of the atoms of the cluster. Based on a prescription of Harris and Michels (Ref.31, Chap.II), a detailed procedure is given to evaluate these integrals.

Hydrogen is commonly observed in the FIM. Sometimes it is advantageous to mix a few atomic percent of hydrogen with the imaging gas. The field adsorption of H_2 and H_3 on a tungsten surface has also been considered, in the present work, in the ASED-MO formalism. As H_2 approaches from the gas phase to the metal surface, the H_2 physisorbs weakly with an energy barrier of about 1.5eV between this physisorbed precursor state and the chemisorption (or the dissociation) phase. Several equipotential contour maps are presented for the ground-state energy surface for different configurations of H_2 on the W(111) surface. Vibrational frequencies of H_2 are determined as a function of field strength. H_3 does not form in free space. However, the formation of the linear H_3 is possible in the vicinity of a surface with the binding energy of about 2.0eV. The formation and the dissociation of H_3 is discussed with and without the field. The adsorbed linear H_3 has the most stable configuration when the ratio of the distances between the outer H atoms and the inner H atoms (adjacent to the surface) is 0.75.

In very strong electric fields the FIM tips themselves evaporate. This phenomena is of particular interest in smoothening of the tips and also in obtaining the best image voltage. To conclude the present work, the mechanism of the field evaporation has also been considered theoretically. The inclusion of the electric field is not self-consistent, i.e., it does not take into account the distortion of the equipotential surfaces due to the presence of the field itself and due to the presence of the kinks, steps, edges, etc., on the surface. Nevertheless, the numerical results on field evaporation closely approximate the experimental results.

In summary, in this thesis, besides adsorption of rare gases and hydrogen on semiconductor surfaces, we discuss field adsorption - desorption phenomena in the framework of an ASED-MO cluster calculation in order to achieve insight into mechanisms which determine the surface structure in a FIM.

CHAPTER I

Van der Waals Interaction of Rare Gases and Hydrogen on Semiconductor Surfaces:

The simplest adsorption phenomena are connected with physisorption[1] of rare gases and hydrogen onto a variety of surfaces such as graphite, alkali halides and metals. Since the advent of helium scattering[2-4] as a surface probe there has been a need for detailed calculations of the surface potential. Whereas the short range repulsion of this potential must be obtained from detailed microscopic models, such as cluster or local density functional calculations,[5] its long range attractive part can be described by the van der Waals dispersion force as[6,7]

$$V(z) = - C_3/z^3 \tag{1.1}$$

where

$$C_3 = \frac{\hbar}{4\pi} \int_0^\infty \alpha(i\omega) \frac{\varepsilon(i\omega)-1}{\varepsilon(i\omega)+1} \, d\omega \quad . \tag{1.2}$$

Here α is the polarizability of the adsorbing particle and ε is the dielectric function of the solid, both taken at imaginary frequencies.

In obtaining equation (1.2) from the general expression of Dzyaloshinskii et al.[6] for the force of attraction between two dielectrics separated by a third (the distance of separation assumed to be much less than the corresponding wavelength of dipole transitions), use has been made of the fact that the medium containing the adsorbing particle is rarefied, so that its dielectric function is close to unity.[8,9]

McLachlan[10] obtains the same expression (1.2) for C_3, using an image-dipole approach. He has also determined the long range part of the substrate-mediated dispersion energy between two identical adparticles

$$V_2(\mathbf{r}_1,\mathbf{r}_2) = C_{s1}\,\frac{2 + 3\cos 2\phi + 3\cos 2\theta}{6\,|\mathbf{r}-\mathbf{r}'_1|^3\,|\mathbf{r}_1-\mathbf{r}_2|^3} - C_{s2}\,\frac{1}{|\mathbf{r}'_1-\mathbf{r}_2|^6} \tag{1.3}$$

where $\mathbf{r}_1$ and $\mathbf{r}_2$ are the positions of the two particles above the surface, $\mathbf{r}'_1$ is the position of the image of particle "1", θ is the angle between $(\mathbf{r}_1-\mathbf{r}_2)$ and the surface, and ϕ is the angle between $(\mathbf{r}'_1-\mathbf{r}_2)$ and the surface (see Fig.1.1). The coefficients C_{s1} and C_{s2} are given by

$$C_{s1} = \frac{3\hbar}{\pi}\int_0^\infty \alpha^2(i\omega)\,\frac{\varepsilon(i\omega)-1}{\varepsilon(i\omega)+1}\,d\omega \tag{1.4}$$

and

$$C_{s2} = \frac{3\hbar}{\pi}\int_0^\infty \alpha^2(i\omega)\left[\frac{\varepsilon(i\omega)-1}{\varepsilon(i\omega)+1}\right]^2 d\omega \quad . \tag{1.5}$$

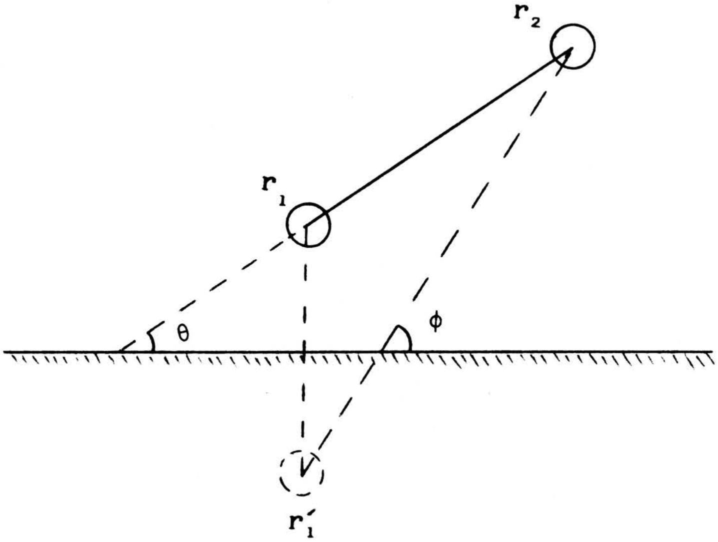

Fig.1.1: As mentioned in the text.

These van der Waals constants for the rare gases and hydrogen interacting with semiconductors have been calculated after evaluating the dielectric function from optical data on 20 different materials; these optical data are listed in Table 1.1. For anisotropic solids, such as CdSe, CdS, etc., where data are available for the electric vector **E** of the incident beam perpendicular and parallel to the **c**-axis of the hcp structure, $\varepsilon(i\omega)$ has been replaced by $\bar{\varepsilon}(i\omega)$ in equations (1.2), (1.4) and (1.5), following the prescription of Bruch and Watanabe:[11]

$$\bar{\varepsilon}(i\omega) = \sqrt{\varepsilon_{\perp}(i\omega)\ \varepsilon_{\parallel}(i\omega)} \quad . \tag{1.6}$$

Results are presented below and are compared with the values obtained by Vidali and Cole.[12] Recent analysis of the He-GaAs interaction by Laughlin[13] has also been used to estimate the binding energy.

a) <u>The dielectric function of semiconductors</u>:

The dielectric function of solids, $\varepsilon(i\omega)$, at the imaginary frequency, $i\omega$, can be calculated from the imaginary part, ε_2, of the dielectric function at the real frequency ω ($\varepsilon(\omega) = \varepsilon_1(\omega)+i\varepsilon_2(\omega)$) as:[14]

$$\varepsilon(i\omega) = 1 + \frac{2}{\pi}\int_0^{\infty} \frac{\omega'\,\varepsilon_2(\omega')}{\omega^2+\omega'^2}\,d\omega' \quad . \tag{1.7}$$

The real and imaginary parts of the dielectric functions of solids can be obtained experimentally by the Kramers-Kronig analysis of normal incidence reflectance data.[15-36] The Kramers-Kronig analysis of non-normal incidence reflection is also available.[37]

According to Phillip and Ehrenreich,[21] three spectral regions may be distinguished, as illustrated in Fig.1.2. The first region,

Table 1.1: Summary of optical data for semiconductors. R = reflectivity; $\varepsilon = \varepsilon_1 + i\varepsilon_2$ = dielectric function; $n + ik$ = refractive index; $\alpha = \frac{2\omega k}{c}$ = absorption coefficient.

Material	E_g (eV)	Temp(K)	Data	Frequency Range(eV)	Reference
Si	1.14	300	$R,\varepsilon_1,\varepsilon_2$	0 - 21	21
		300	$R,n,k,\alpha,\varepsilon_1,\varepsilon_2$	1.5 - 6	48
Ge	0.67	300	$R,\varepsilon_1,\varepsilon_2$	0 - 21	21
		300	R,n,k,α	0 - 10	16
		300	$R,n,k,\alpha,\varepsilon_1,\varepsilon_2$	1.5 - 6	48
GaP	2.26	300	$R,\varepsilon_1,\varepsilon_2$	0 - 25	21
		300	R,α,n	15 - 35	31
		300	$R,n,k,\alpha,\varepsilon_1,\varepsilon_2$	1.5 - 6	48
InP	1.35	300	$R,n,k,$	0 - 20	29
		300	R,α,n	15 - 35	31
		300	$R,n,k,\alpha,\varepsilon_1,\varepsilon_2$	1.5 - 6	48
GaAs	1.43	300	$R,\varepsilon_1,\varepsilon_2$	0 - 25	21
		300	R,α,n	15 - 35	31
		300	$R,n,k,\alpha,\varepsilon_1,\varepsilon_2$	1.5 - 6	48
InAs	0.35	300	$R,\varepsilon_1,\varepsilon_2$	0 - 25	21
		300	R,α,n	15 - 35	31
		300	$R,n,k,\alpha,\varepsilon_1,\varepsilon_2$	1.5 - 6	48
InSb	0.18	300	$R,\varepsilon_1,\varepsilon_2$	0 - 25	21
		300	R,α,n	15 - 35	31
		300	$R,n,k,\alpha,\varepsilon_1,\varepsilon_2$	1.5 - 6	48
MgO		100,300	R	6 - 29	33
		400	R	6 - 25	33
		100	ε_2	0 - 30	33
ZnO	3.2	300	$R,\varepsilon_1,\varepsilon_2$	1.5 - 25	33
		100,400	R	4 - 26	33
CdO		300	$R,\varepsilon_1,\varepsilon_2$	1 - 30	33
		100,400	R	4 - 30	33

Table 1.1 (continued):

Material	E_g (eV)	Temp(K)	Data	Frequency Range(eV)	Reference
ZnS	3.6	300	$R, \varepsilon_1, \varepsilon_2$	1.5 - 25	33
		100,400	R	4 - 25	33
		300	α(film)	55 - 150	30
		300	R,n,k	3 - 20	25
CdS	2.42	300	$R, \varepsilon_1, \varepsilon_2$	0.5 - 25	33
		100,400	R	4 - 25	33
		300	α(film)	40 - 150	30
		300	$R, \varepsilon_1, \varepsilon_2, \alpha$	0 - 20	26
		300	R,n,k	0 - 12	25
PbS	0.34 - 0.37	300	R,n,k	1 - 18	24
		300	α(film)	35 - 150	30
ZnSe		300	$R, \varepsilon_1, \varepsilon_2$	1.5 - 23	33
		100	R	4 - 23	33
		300	α(film)	35 - 150	30
		300	$R, \varepsilon_1, \varepsilon_2$	1 - 10	17
CdSe	1.74	300	$R, \varepsilon_1, \varepsilon_2$	0.5 - 23	33
		100,400	R	4 - 23	33
		300	α(film)	35 - 140	30
		300	R,n,k	0 -10	25
HgSe		12,300	R	4 -12	23
		2	R, ε_2	0 - 0.1	35
		95,300	R	0 - 0.1	35
		10 - 300	α, n, ε_1	0.05 - 0.25	47
PbSe	0.27	300	R	1 - 21	24
		300	n,k	0 - 15	24
ZnTe		300	$R, \varepsilon_1, \varepsilon_2$	1 - 25	33
		100,400	R	4 - 25	33
		300	α(film)	40 - 150	30
		300	R	2 - 23	22
		300	n,k	0 - 20	27

Table 1.1 (continued):

Material	E_g (eV)	Temp(K)	Data	Frequency Range(eV)	Reference
CdTe	1.45	300	$R, \varepsilon_1, \varepsilon_2$	0.5 - 25	33
		100,400	R	4 -23	33
		300	n,k	0 - 20	27
		300	α(film)	40 - 150	30
		115	R	2 - 8.5	36
		300	R	2 - 23	22
		300	ε_2	0 - 9	28
		15	R	2 - 8	32
HgTe		12,300	R	4 - 12	23
		115	R	2 - 8.5	36
		10	R	2 - 9	32
		300	R(arb. unit)	2 - 23	22
	-0.3 - 0.15	8 - 300	$R, \varepsilon_1, \varepsilon_2$	0.01 - 0.1	34
		300	n, ε_1	0.05 - 0.15	47
SnTe	0.18	300	R,n,k	1 - 20	24
PbTe	0.3	300	$R, n, k, \varepsilon_1, \varepsilon_2$	0.5 - 17	24
		300	α(film)	35 - 150	30
$Cd_xHg_{1-x}Te$		115	R	2 - 8.5	36

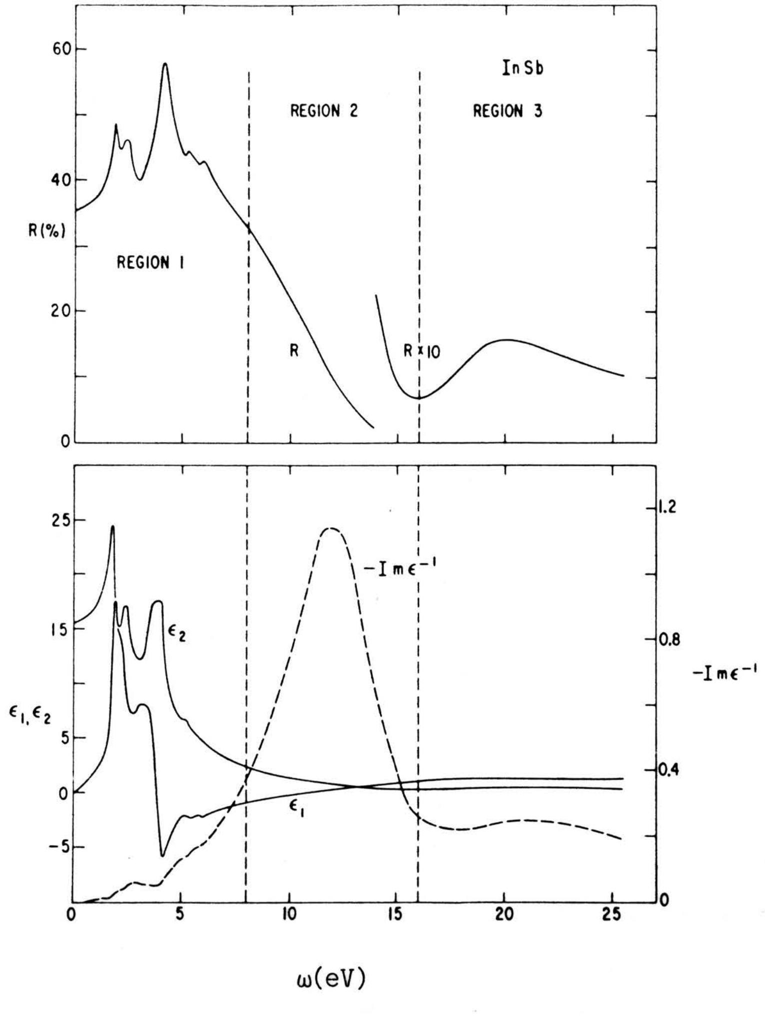

Fig.1.2: The spectral dependence R, the real and imaginary parts of the dielectric constant, ε_1 and ε_2, and the energy-loss function, $-\mathrm{Im}\,\varepsilon^{-1}$, for InSb (from Phillip and Ehrenreich[21]).

extending to about 8 to 10 eV in most semiconductors, is characterized by sharp structures associated with valence to conduction interband transition and, in particular, in polar materials, with the lattice polarizability. Methods are available to calculate the band structures of the semiconductors, e.g., those based on Kane's model,[38] the tight-binding method, etc.

In Kane's model, one calculates the band structure using the **k.p** perturbation approach, assuming that the conduction and valence band extrema are at **k**=0. The small band gap requires an accurate treatment of conduction and valence band interactions, while higher bands can be treated by perturbation theory. In a great many semiconducting materials the spin-orbit interaction plays an important role. The spin-orbit interaction is very small for the light elements but increases rapidly as one moves to the right or downward in the periodic table.

In the tight-binding approximation, one assumes that the crystal wave function is close to that of the free atoms of which it is composed. Thus the Bloch functions are represented in terms of a periodic function and a Wannier function, which itself is approximated as a linear combination of atomic orbitals (LCAO). Because of this approximation, the tight-binding method is also known as the method of the LCAO.

In the second spectral region,[21] which extends to about 20 eV, the reflectance decreases monotonically. This behaviour can be associated with collective excitations of essentially free valence electrons. In the third region, beyond 20 eV, the reflectance may rise again to some extent, due to transitions between filled d-bands, which lie below the valence band, and empty conduction band states.

Most optical data on semiconductors have been taken in the first region where a detailed knowledge of the band structure is needed for their interpretation.[15-29,32-36,39,40] Extensive tight binding and ab initio calculations within the local-density-functional formalism have been performed for this purpose for a variety of semiconductors.[32,41-46] A detailed study of zero-gap semiconductors, based on the effective mass approximations exists for the region below 1 eV.[34,47,49] The low frequency[50] and long wavelength dynamic dielectric function[51] for those materials have been studied extensively.

It turns out that the calculation for the van der Waals interaction of atoms in semiconductors for this first region contributes little. The polarizability at imaginary frequency, $\alpha(i\omega)$, drops to only 10% of its static value for ω ranging between 60 eV and 100 eV, depending on the adsorbed particle (H, H_2, He, Ne, Ar, Kr and Xe). Thus one needs $\varepsilon(i\omega)$ up to about 100 eV to calculate C_3, C_{S1} or C_{S2} . In eqn.(1.7) the factor $\frac{\omega'}{\omega^2+\omega'^2}$ in the integrand has a peak at $\omega' = \omega$, making it desirable for the reliability of the value of $\varepsilon(i\omega)$, to have $\varepsilon_2(\omega')$ up to about $\omega' = 100$ eV, where little is known either experimentally[30] or theoretically, so that some extrapolation of data is needed. Fortunately the Kramers-Kronig relations provide a check on such extrapolations.

The procedure is recounted briefly.[15,16,22,29,52-57] At normal incidence, the Fresnel equation for the reflection of radiation from an absorbing medium of complex index of refraction $\tilde{n}$ (= n+ik) is

$$r = \frac{n+ik-1}{n+ik+1} \tag{1.8}$$

giving the reflectance (or reflectivity) R, which is the measured quantity, in terms of the complex reflection coefficient r as

$$R = |r|^2 \quad . \tag{1.9}$$

The phase, θ, of r defined by

$$r = |r|\, e^{i\theta} = \sqrt{R}\, e^{i\theta} \tag{1.10}$$

or,

$$\ln r = \frac{1}{2} \ln R + i\theta \tag{1.11}$$

can be detrmined at any single frequency from the Kramers-Kronig relation[58]

$$\theta(\omega) = -\frac{2\omega}{\pi} \int_0^\infty \frac{\frac{1}{2} \ln R(\omega')}{\omega'^2 - \omega^2}\, d\omega' \tag{1.12}$$

which can be written in the alternative form as[59]

$$\theta(\omega) = -\frac{1}{2\pi} \int_0^\infty \frac{d \ln R(\omega')}{d\omega'} \ln \left| \frac{\omega' + \omega}{\omega' - \omega} \right| d\omega' \quad . \tag{1.13}$$

From eqns (1.8) and (1.10) one can write the index of refraction, n, and the absorption coefficient, k, as

$$n = \frac{1 - R}{1 - 2\sqrt{R}\cos\theta + R} \tag{1.14}$$

and

$$k = \frac{2\sqrt{R}\sin\theta}{1 - 2\sqrt{R}\cos\theta + R} \tag{1.15}$$

These in turn determine the real and imaginary parts of the dielectric function $\varepsilon = \varepsilon_1 + i\varepsilon_2$:

$$\varepsilon_1(\omega) = n^2(\omega) - k^2(\omega) \tag{1.16}$$

$$\varepsilon_2(\omega) = 2\, n(\omega)\, k(\omega) \tag{1.17}$$

for which Kramers-Kronig relations hold[14]

$$\varepsilon_2(\omega) = -\frac{2\omega}{\pi}\int_0^\infty \frac{\varepsilon_1(\omega')-1}{\omega'^2-\omega^2}\,d\omega' \qquad (1.18)$$

$$\varepsilon_1(\omega) = 1 + \frac{2}{\pi}\int_0^\infty \frac{\omega'\varepsilon_2(\omega')}{\omega'^2-\omega^2}\,d\omega' \qquad (1.19)$$

In eqns (1.18) and (1.19) the usual $\varepsilon(\omega=\infty)$ terms have been replaced by unity, since, for the present purposes, ω extends to far ultraviolet or soft x-rays where this approximation suffices.

Because reflectance data are only taken over a limited range of frequencies, to an upper limit ω_u, say (typically of the order of 20-30 eV), one needs to specify the asymptotic behaviour in eqn.(1.12) for $\omega_u < \omega < \infty$. Cardona[30] finds reflectance to be well below 0.01 between ω = 35 eV and 150 eV, justifying the asymptotic diminishing assumption for reflectance in this region. Typically one chooses a power law[24,33,56] behaviour $R \sim \omega^{-n}$, and fixes n such that the low frequency behaviour of ε_2, as calculated from (1.17), matches the values obtained directly from absorption measurements around the band gap.

After little manipulation, the equation (1.12) can be transformed into a form which is more convenient to handle numerically. It can be written as

$$\theta(\omega) = -\frac{\omega}{\pi}\int_0^\infty \frac{\ln\left(R(\omega')/R(\omega) \right)}{\omega'^2-\omega^2}\,d\omega' \qquad (1.20)$$

where the integrand is finite for lim $\omega' \to \omega$, provided the reflectivity spectrum does not have an infinite slope at ω, and it does not vanish at ω, as well. Such an adverse situation never occurs experimentally.

Writing $R \propto \omega^{-n}$ beyond ω_u (the proportionality constant is chosen such as to maintain the continuity in R), one writes eqn.(1.20) as a sum:

$$\theta(\omega) = -\frac{\omega}{\pi}\int_0^{\omega_u} \frac{\ln(R(\omega')/R(\omega))}{\omega'^2-\omega^2}\,d\omega'$$

$$-\frac{1}{2\pi}\ln(R(\omega_u)/R(\omega))\ln\left|\frac{\omega_u+\omega}{\omega_u-\omega}\right|$$

$$-\frac{n}{2\pi}\int_{\omega_u}^{\infty}\ln\left|\frac{\omega'-\omega}{\omega'+\omega}\right|\frac{d\omega'}{\omega'} \qquad (1.21)$$

The last integral in eqn.(1.21) can be expressed in terms of an infinite sum:

$$\int_{\omega_u}^{\infty}\ln\left|\frac{\omega'-\omega}{\omega'+\omega}\right|\frac{d\omega'}{\omega'} = \begin{cases} -2\sum\limits_{\ell=0}^{\infty}\frac{1}{(2\ell+1)^2}(\omega/\omega_u)^{2\ell+1} & ;\ \omega < \omega_u \\ -\frac{\pi^2}{2}+2\sum\limits_{\ell=0}^{\infty}\frac{1}{(2\ell+1)^2}(\omega_u/\omega)^{2\ell+1} & ;\ \omega > \omega_u \\ -\frac{\pi^2}{4} & ;\ \omega = \omega_u \end{cases} \qquad (1.22)$$

Even if it is possible to get θ for all ω from eqn.(1.21), one usually calculates it and thereafter ε_1 and ε_2 for the frequency range for which data on R is available. The reliability of the values of θ decreases as one goes beyond this range, since the factor $\frac{1}{\omega'^2-\omega^2}$, appearing in the integrand of eqn.(1.12), is sharply peaked at $\omega' = \omega$.

Because data so obtained for $\varepsilon_1(\omega)$ and $\varepsilon_2(\omega)$ are only given for a finite range $0 < \omega \leqq \omega_c$ ($\approx \omega_u$) (see Table 1.1), the asymptotic behaviour for $\varepsilon_2(\omega) \sim \omega^{-m}$ is assumed (for $\omega > \omega_c$) to calculate $\varepsilon(i\omega)$ in eqn.(1.7). m is chosen such that $\varepsilon_1(\omega)$, as calculated from the Kramers-Kronig relation (1.19), matches the value given from the reflectance analysis (1.13) through (1.16).

The eqn. (1.19) can be written as

$$\varepsilon_1(\omega) = 1 + \frac{2}{\pi}\int_0^{\infty} \frac{\omega'\,\varepsilon_2(\omega') - \omega\,\varepsilon_2(\omega)}{\omega'^2 - \omega^2}\,d\omega' \tag{1.23}$$

or,

$$\varepsilon_1(\omega) = 1 + \frac{2}{\pi}\int_0^{\omega_c} \frac{\omega'\,\varepsilon_2(\omega') - \omega\,\varepsilon_2(\omega)}{\omega'^2 - \omega^2}\,d\omega' + \frac{2A}{\pi}\int_{\omega_c}^{\infty} \frac{\omega'^{\,1-m}}{\omega'^2 - \omega^2}\,d\omega' - \frac{\varepsilon_2(\omega)}{\pi}\ln\frac{|\omega_c + \omega|}{|\omega_c - \omega|} \tag{1.24}$$

where A is given by

$$\varepsilon_2(\omega) = A\,\omega^{-m} \tag{1.25}$$

for $\omega \geqq \omega_c$. The second integral in eqn.(1.24) can be written as

$$\int_{\omega_c}^{\infty} \frac{\omega'^{\,1-m}}{\omega'^2 - \omega^2}\,d\omega' = \begin{cases} \dfrac{1}{2\sqrt{\omega}}\left[\ln\dfrac{|1-\sqrt{y}|}{|1+\sqrt{y}|} + 2\tan^{-1}\sqrt{y} - \pi\right] & ;\ m=\frac{1}{2} \\[2ex] \dfrac{1}{2\omega}\ln\left|\dfrac{1+y}{1-y}\right| & ;\ m=1 \\[2ex] \dfrac{1}{\omega^2}\ln\dfrac{y}{\sqrt{1-y^2}} & ;\ m=2 \end{cases} \tag{1.26}$$

where $y = \dfrac{\omega_c}{\omega}$.

For some materials these fits for $\varepsilon_1(\omega)$ are not easy if $\varepsilon_2(\omega_c)$ is still appreciably different from zero. Such a bad example is given in Fig.1.3; a good fit is presented in Fig.1.4. For most materials best fits can be obtained with $1 \leqq m \leqq 2$. The fact that $\varepsilon_2(\omega)$ satisfies a sum rule, unfortunately, does not help in determining its asymptotic behaviour. As an exact statement (i.e. involving an integration over frequency up to infinity), it cannot be tested, and, as an approximation (i.e. integrating

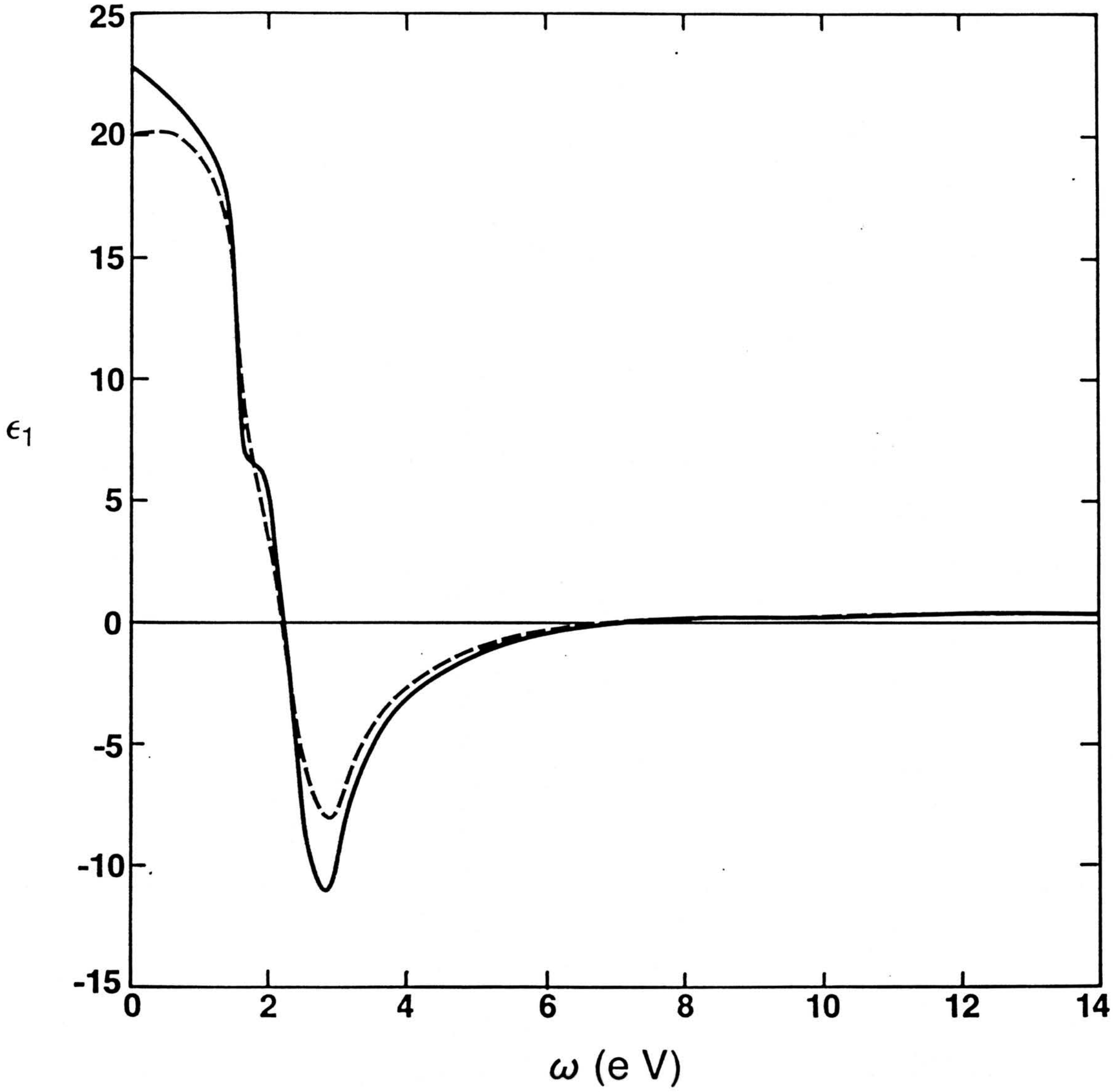

Fig.1.3: Real part ε_1 of the dielectric function for PbSe. Solid line obtained from reflectivity data[24] via eqns (1.13) - (1.16). Dashed line obtained using eqn.(1.19) with ε_2 from eqn.(1.17), assuming, in addition, an asymptotic behaviour $\varepsilon_2(\omega) \sim \omega^{-2}$ for $\omega > 15$ eV.

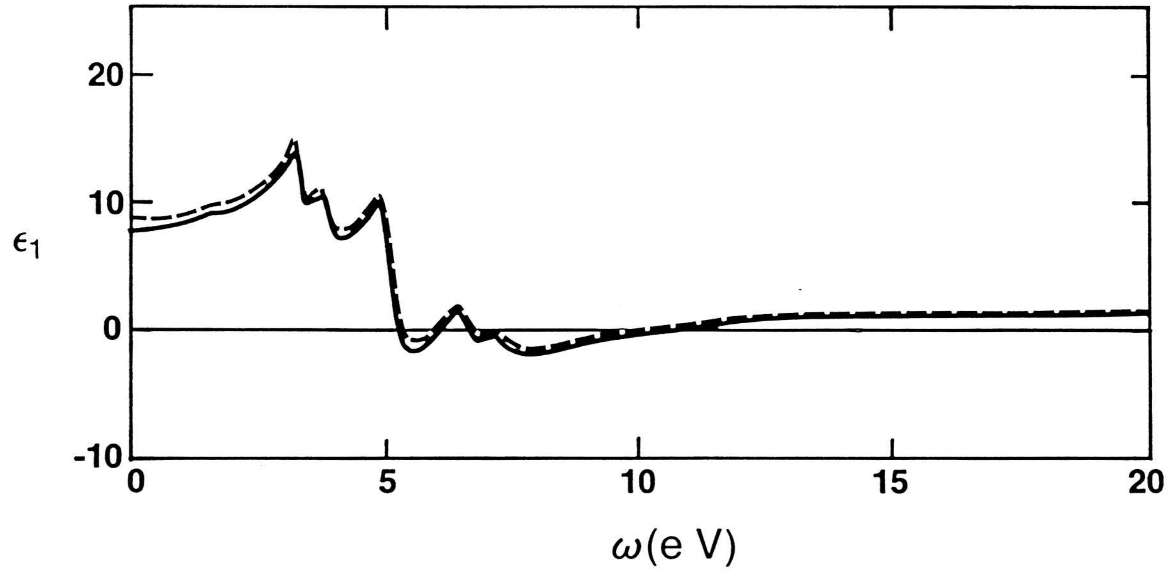

Fig.1.4: Real part ε_1 of the dielectric function for CdTe. Solid line obtained from reflectivity data[33] via eqns (1.13) - (1.16). Dashed line obtained using eqn.(1.19) with ε_2 from eqn.(1.17) assuming, in addition, an asymptotic behaviour $\varepsilon_2(\omega) \sim \omega^{-\frac{1}{2}}$ for $\omega > 25$ eV. The asymptotic behaviour $\varepsilon_2(\omega) \sim \omega^{-2}$, used in the calculations of the van der Waals constants, is indistinguishable from the solid line.

up to some cut-off frequency), it merely serves to define the effective number of valence electrons.

b) The Polarizability of the adsorbing particles:

The polarizability of a particle at imaginary frequency is given by

$$\alpha(i\omega) = \sum_n \frac{f_{no}}{\omega_{no}^2 + \omega^2} \tag{1.27}$$

where f_{no} and ω_{no} are the oscillator strength and the transition frequency of the particle, respectively. Langhoff and Karplus[60] give expressions for the bounds to the polarizability using Padé approximants:

$$\frac{\alpha_0^2/\alpha_1}{(\alpha_0/\alpha_1) + \omega^2} \leqq \alpha(i\omega) \leqq \frac{N}{N/\alpha_0 + \omega^2} \tag{1.28}$$

where $N = \sum_n f_{no}$ is the number of electrons in the particle, via the sum rule.

The Cauchy coefficients α_0 (the static polarizability) and α_1 are quoted in Table 1.2. For the rare gas atoms, Langhoff and Karplus[60] give an approximate expression for the polarizability which is similar to the one given in reference 62:

$$\alpha(i\omega) = \frac{\alpha_0\, \bar{\omega}^2}{\bar{\omega}^2 + \omega^2} \tag{1.29}$$

where

$$\bar{\omega} = \frac{4}{3}\, \frac{C_{aa}}{\alpha_0^2} \tag{1.30}$$

The dipole dispersion force coefficients C_{aa} are quoted in Table 1.3. In

Table 1.2: Cauchy coefficients α_0 (static polarizability) and α_1 (in atomic units) for H, H_2, He, Ne, Ar, Kr and Xe. These have been taken from tables I and IV of Ref.60. They are exact for H but have been calculated for the remaining elements from refractivity data.[61]

	H	H_2	He	Ne	Ar	Kr	Xe
α_0	4.5	5.439	1.3838	2.668	11.091	16.74	27.34
α_1	26.5833	20.02	1.55	2.863	28.16	55.53	116.2

Table 1.3: Dipole dispersion force coefficients C_{aa} (in atomic units) for the rare gas atoms as given in table V of Ref.60.

He	Ne	Ar	Kr	Xe
1.47 ± 0.02	7.03 ± 0.55	69.3 ± 5.7	140 ± 16	423 ± 66

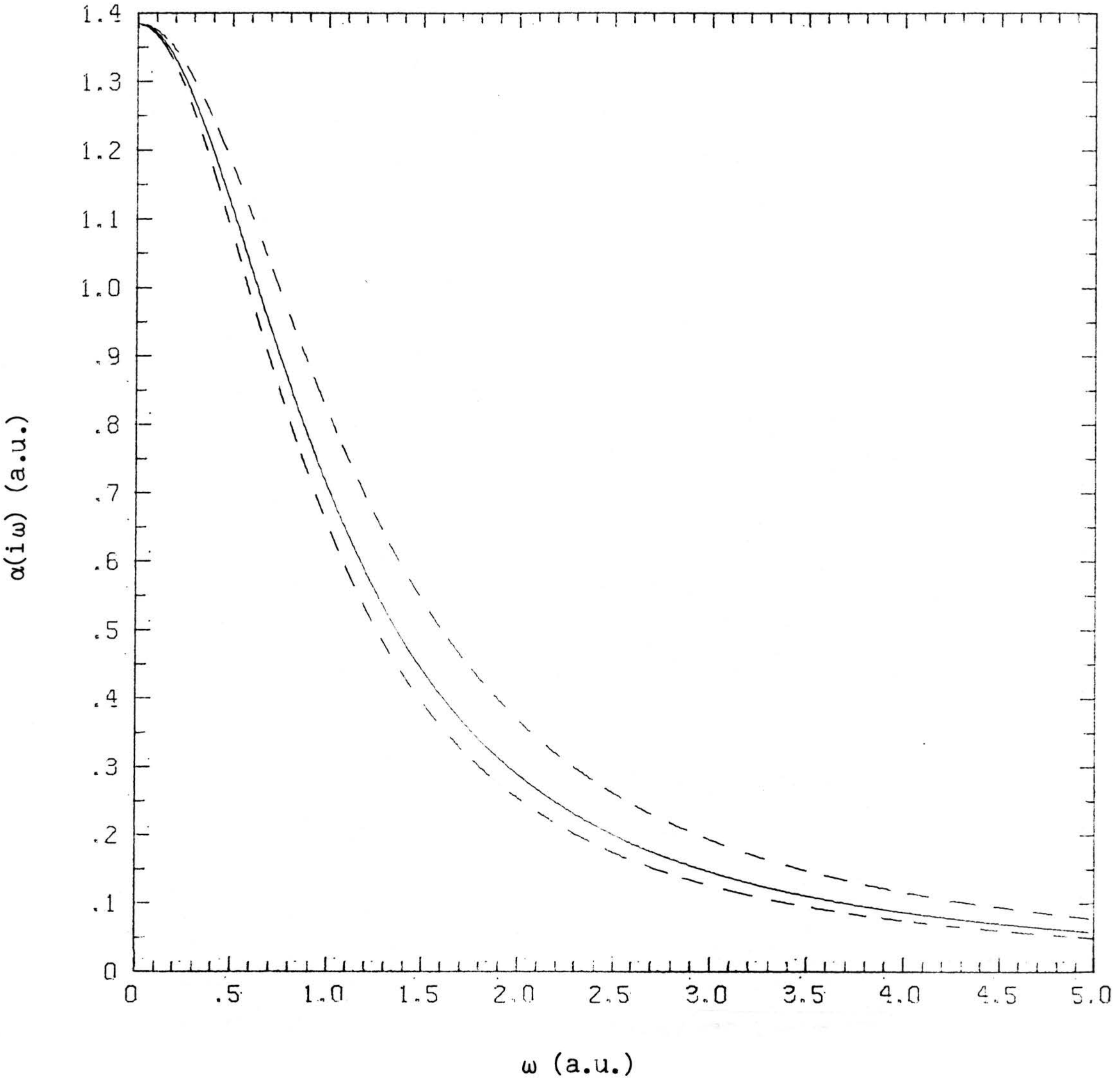

Fig.1.5: Polarizability of He (1 a.u. = 0.1482 Å^3) at imaginary frequency as a function of real frequency (1 a.u. = 27.2 eV). The solid curve is obtained from eqn.(1.29) and has been used to calculate the van der Waals constants. The dashed curves are the two bounds as given by eqn.(1.28).

Fig.1.5 the polarizability $\alpha(i\omega)$ for He is plotted as a function of ω using eqn.(1.29) and the upper and lower bounds from eqn.(1.28). The curve, as obtained using the approximate expression (1.29), lies in between the two bounds, showing that the expression (1.29) is indeed a good approximation for the present purposes. The situation for other rare gas atoms is similar.

c) Results:

The van der Waals coefficients C_3, C_{s1} and C_{s2} of eqns (1.2), (1.4) and (1.5) have been calculated for H, H_2 and the rare gases interacting with any of the 20 semiconductors listed in Table 1.1, except the mercury compounds. For the polarizability of the rare gas atoms, eqn.(1.29) has been used. For H and H_2, as well as for He, the upper and lower bounds for the polarizability in eqn.(1.28) are used to calculate the van der Waals coefficients. For He, the variations in these results from those obtained using the approximate expression (1.29) are less 5%. For H and H_2 the mean of the two values is taken.

To demonstrate the sensitivity of the van der Waals coefficients to the asymptotic behaviour of $\varepsilon_2(\omega)$ for $\omega>\omega_c$ two examples are discussed in detail. Table 1.4 lists C_3 values for the above gases interacting with CdTe for m=0.5, 1 and 2 and the cut-off at $\hbar\omega_c$ = 25 eV. There is a considerable variation in C_3 across m values. However, from Fig.1.4, one knows that one should choose $1 \leq m \leq 2$, amounting to an error in C_3 of less than 15%. Table 1.5 gives C_3 for PbSe ($\hbar\omega_c$ = 15 eV). In this case the asymptotes of $\varepsilon_2(\omega)$ are difficult to establish, as one sees in Fig.1.3. However, C_3 is less sensitive to the m values chosen.

Table 1.4: Van der Waals coefficients C_3 (in meV $\mathring{A}^3$) for CdTe, calculated using (1.2) for different asymptotic behaviour of $\varepsilon_2(\omega) \propto \omega^{-m}$ beyond $\hbar\omega_C$ = 25 eV. In the last column $\varepsilon_2(\omega) = 0$ for $\omega > \omega_C$.

m	0.5	1	2	cut-off
H	523	454	417	386
H_2	757	639	577	526
He	294	227	195	171
Ne	672	498	414	356
Ar	1899	1542	1361	1219
Kr	2631	2173	1938	1749
Xe	4696	3811	3362	3010

Table 1.5: The same as in Table 1.4 but for PbSe. $\hbar\omega_C$ = 15 eV.

m	0.5	1	2	cut-off
H	370	333	316	304
H_2	508	446	419	400
He	173	141	127	119
Ne	374	292	260	242
Ar	1194	1015	939	889
Kr	1702	1467	1366	1297
Xe	2954	2507	2318	2193

For semiconductors, such as Si, GaAs, PbTe, GaP and InSb, the maximum uncertainty in C_3 as a result of varying m from 0.5 to 2, is less than 10%; Si, having no d levels, shows no dependence on the extrapolation because ε_2 drops to zero within the experimentally accessible frequency range.

All the data on C_3, C_{s1} and C_{s2} calculated at T = 300 K (except for MgO at T = 100 K), are listed in Tables 1.6 - 1.8. Choosing m=2 for all materials, the numbers should be accurate to within 10%. It is amazing that for a given gas particle the variation in the van der Waals constants for different semiconductors is less than 50%, i.e. also within the range for metals and for graphite.[11,63,64] The van der Waals constants for metals and graphite, as taken from Bruch,[63] are quoted in Table 1.9 for comparison purposes. In Figs 1.6 and 1.7, $\varepsilon(i\omega)$ and $\frac{\varepsilon(i\omega)-1}{\varepsilon(i\omega)+1}$ have been plotted, respectively, for a metal with a typical plasma frequency ω_p = 10 eV and two semiconductors, namely CdTe and PbSe, for comparison purposes. The dependence of C_{s2} on different materials is more noticeable because of the quadratic dependence of the integrand on $\frac{\varepsilon(i\omega)-1}{\varepsilon(i\omega)+1}$ in eqn.(1.5).

With so little variation, no trustworthy trends can be established. For example, increasing the polarity by going from a III - V compound to a II - VI compound in the same row of the periodic table, one might expect larger van der Waals interaction. However, this is not the case because the frequency range in the dielectric response due to optical phonons does not contribute significantly to the van der Waals constants. Similarly, any structure around the band gaps is too low in

Table 1.6: Van der Waals coefficients C_3 (in meV Å^3) :

	H	H_2	He	Ne	Ar	Kr	Xe
Si	406	550	174	360	1261	1818	3113
Ge	449	615	201	421	1429	2047	3529
GaP	416	570	187	393	1329	1902	3282
InP	414	569	188	397	1329	1900	3283
GaAs	409	558	181	377	1290	1852	3186
InAs	419	574	188	395	1335	1911	3296
InSb	399	541	173	360	1244	1790	3071
MgO	310	435	151	325	1043	1475	2576
ZnO	322	450	155	332	1072	1519	2648
CdO	357	495	168	359	1171	1665	2894
ZnS	376	519	174	369	1222	1742	3019
CdS	354	487	162	343	1142	1631	2822
PbS	355	476	149	306	1080	1563	2667
ZnSe	377	520	174	367	1220	1741	3014
CdSe	367	505	169	356	1185	1691	2927
PbSe	316	419	127	260	939	1366	2318
ZnTe	398	545	180	378	1271	1819	3140
CdTe	417	577	195	414	1361	1938	3362
SnTe	422	573	184	383	1319	1897	3256
PbTe	318	420	126	257	937	1365	2312

Table 1.7: Coefficients C_{s1} (in meV Å^6) in eqns (1.3) and (1.4) :

	H	H_2	He	Ne	Ar	Kr	Xe
Si	2449	4165	365	1495	20292	43407	123583
Ge	2625	4507	407	1692	22258	47331	135592
GaP	2419	4163	378	1574	20611	43781	125562
InP	2400	4127	375	1571	20443	43407	124540
GaAs	2416	4133	369	1528	20310	43280	123714
InAs	2452	4203	379	1578	20733	44103	126300
InSb	2397	4066	357	1470	19805	42358	120622
MgO	1688	2975	288	1233	15175	31826	92492
ZnO	1776	3109	297	1266	15751	33124	95991
CdO	2012	3488	326	1381	17478	36920	106498
ZnS	2136	3704	343	1446	18518	39169	112832
CdS	2037	3509	321	1349	17435	36971	106219
PbS	2198	3681	313	1275	17662	38009	107543
ZnSe	2157	3729	343	1443	18585	39361	113233
CdSe	2109	3636	333	1400	18075	38320	110123
PbSe	2025	3340	269	1105	15756	34146	95917
ZnTe	2314	3975	360	1503	19658	41774	119758
CdTe	2368	4099	380	1606	20485	43327	124813
SnTe	2541	4304	378	1557	20946	44805	127569
PbTe	2053	3376	275	1103	15862	34436	96556

Table 1.8: Coefficients C_{s2} (in meV $\mathring{A}^6$) in eqns (1.3) and (1.5) :

	H	H_2	He	Ne	Ar	Kr	Xe
Si	1677	2728	213	830	12578	27547	76539
Ge	1886	3099	248	978	14465	31511	88039
GaP	1592	2624	211	836	12296	26747	74840
InP	1574	2586	208	823	12094	26323	73610
GaAs	1612	2636	209	820	12240	26722	74488
InAs	1652	2707	216	851	12603	27481	76704
InSb	1623	2625	203	793	12044	26418	73282
MgO	744	1265	110	448	6155	13180	37485
ZnO	831	1399	119	482	6734	14482	41006
CdO	1090	1806	149	597	8547	18506	52031
ZnS	1223	2035	168	669	9639	20871	58680
CdS	1128	1858	150	597	8716	18947	53054
PbS	1422	2264	170	656	10216	22560	62148
ZnSe	1255	2078	170	676	9801	21259	59658
CdSe	1208	1992	161	641	9350	20317	56912
PbSe	1280	2004	145	556	8888	19765	54056
ZnTe	1465	2406	193	762	11238	24474	68398
CdTe	1510	2502	205	820	11818	25614	71943
SnTe	1839	2963	228	891	13556	29766	82480
PbTe	1331	2079	150	573	9193	20466	55906

Table 1.9: Coefficients C_3, C_{s1} and C_{s2} (in a.u.) for some metals and graphite (basal plane surface) as taken from Bruch.[63] For C_3, 1 a.u. = 4032 meV Å^3; for C_{s1} and C_{s2}, 1 a.u. = 597.5 meV Å^6 .

	Cu	Ag	Au	Al	Pd	Gr
C_3:						
H	0.124	0.126	0.135	0.123	0.112	0.090
H_2	0.169	0.174	0.188	0.166	0.152	0.121
He	0.0583	0.0618	0.0678	0.0544	0.0523	0.043
Ne	0.121	0.130	0.143	0.110	0.108	0.086
Ar	0.402	0.420	0.458	0.384	0.362	0.30
Kr	0.569	0.602	0.642	0.546	0.512	0.43
Xe	0.841	0.871	0.941	0.812	0.758	0.61
C_{s1}:						
H	4.72	4.66	4.90	4.87	4.31	3.55
H_2	7.88	7.85	8.33	8.07	7.16	5.80
He	0.754	0.773	0.837	0.744	0.680	0.57
Ne	3.02	3.13	3.41	2.93	2.72	2.23
Ar	39.4	39.7	42.5	39.7	35.7	29.7
Kr	82.1	82.2	87.6	83.3	74.5	63
Xe	191	191	202	195	174	142
C_{s2}:						
H	3.76	3.62	3.93	4.06	3.20	2.16
H_2	5.99	5.81	6.39	6.43	5.04	3.30
He	0.503	0.501	0.568	0.527	0.417	0.31
Ne	1.93	1.94	2.22	2.01	1.60	1.18
Ar	28.3	27.8	31.0	30.2	23.7	17.6
Kr	60.8	59.3	65.5	65.0	51.1	38
Xe	146	141	155	156	123	89

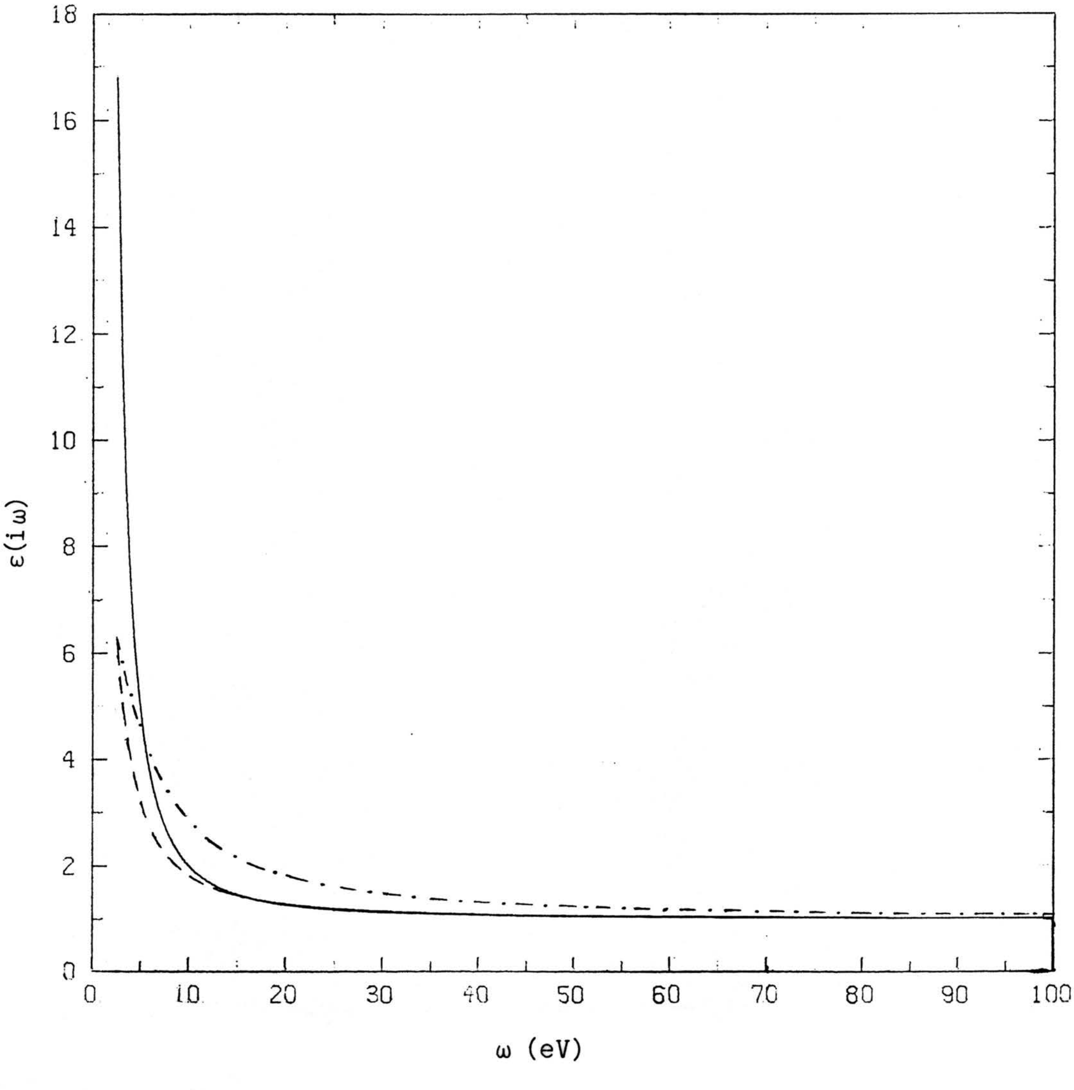

Fig.1.6: Dielectric function at imaginary frequency as a function of real frequency. The dashed curve is for PbSe and the dot-dashed curve is CdTe. The solid curve is for a metal with plasma frequency $\omega_p = 10$ eV ($\varepsilon_{met}(i\omega) = 1 + (\omega_p/\omega)^2$; $\omega_p = \sqrt{4\pi n e^2/m_e}$; n is the electron volume density). In this figure ω starts at about 3 eV to amplify the distinction among the different curves.

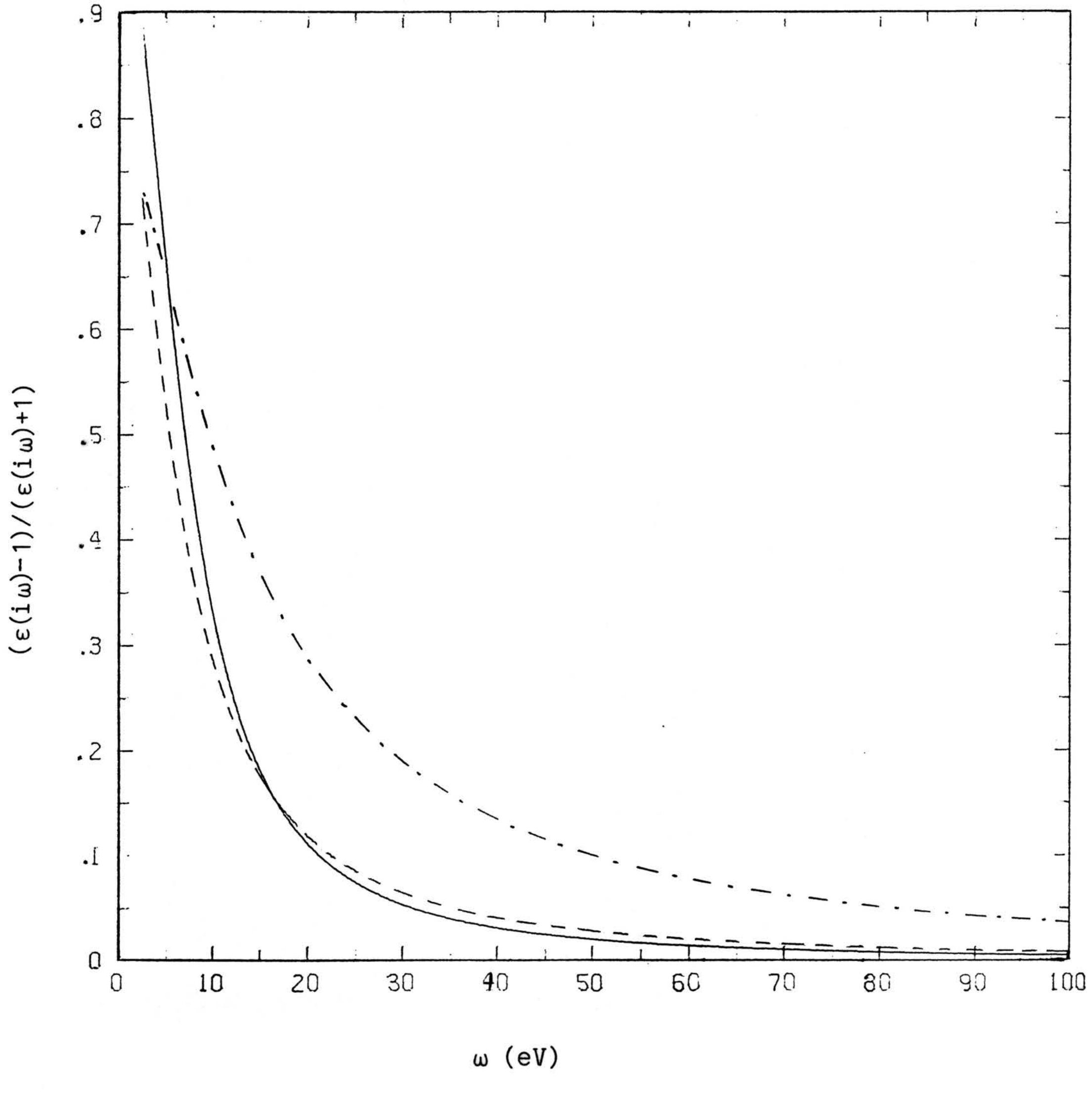

Fig.1.7: See the figure caption 1.6 for the explanation of $\varepsilon(i\omega)$ and ω. Again the dashed curve is for PbSe, the dot-dashed is for CdTe and the solid curve is for a metal with ω_p = 10 eV.

frequency to be important. The main contribution to the van der Waals constants is given by the frequency region in which the collective excitations of the valence electrons contribute most significantly to the dielectric function. Thus it is not surprising that the simple metallic-like model used by Vidali and Cole[12] gives reasonable results.

To estimate the binding energy or heat of adsorption of a particle on a semiconductor, one needs, in addition to C_3, the equilibrium distance z_m of the surface potential minimum. The latter can only be determined via an accurate calculation of the repulsive part of the surface potential (see Chap.II). Laughlin[13] has analysed the He-GaAs system and finds that $z_m \sim 3.5$ Å . One would then estimate the binding energy of He on GaAs to be of the order of 50 K, i.e. only one third of its value on graphite or on metals. This is in agreement with a suggestion by Vidali and Cole,[12] who argued that the rather extended valence electron charge density will repel adparticles at relatively large distances from the surface of the semiconductor.

Esser and Göpel[65] have studied physical adsorption of CO_2, CO, O_2, Xe and H_2 on ZnO. They find a broad distribution of adsorption energies from which heats of adsorption Q of 3.5 kJ/mol = 36.4 meV/particle for H_2 and 24.1 kJ/mol = 250 meV/partcle for Xe can be determined. Equating $Q \approx C_3/z_m^3$, one estimates $z_m = 2.3$ Å for H_2 and $z_m = 2.2$ Å for Xe, as the equilibrium distance of adsorption. The value for H_2 is certainly acceptable but that for Xe is far too small, indicating that binding due to interactions other than the van der Waals are important for the heavy rare gases. This is not surprising in view of the fact that, for example, Xe on W shows a non-negligible charge transfer.[66]

Unfortunately, data on zero-gap and narrow-gap Hg alloys,[32,36,39,43,46] such as $Hg_xCd_{1-x}Te$ and $Hg_xCd_{1-x}Se$, are not sufficient for a reliable calculation of van der Waals constants to establish trends as a function of the Hg mole fraction.

CHAPTER II

1. Field Adsorption of Rare Gases :

The lighter rare gases (He, Ne, Ar) are the most frequently used imaging gases in field-ion microscopy.[1-5] Little seems to be known theoretically about the adsorption properties of rare gases at metal surfaces in the presence of a strong electric field of the order of several volts per angstrom. To introduce the subject, the models that have been developed for rare gas adsorption on metals without a field present are reviewed. As mentioned in chapter I, the long-range attraction of a rare gas atom several angstroms above a surface is given by the van der Waals potential that varies as z^{-3}. The short range repulsion is due to a combination of increasing electron overlap and Coulomb repulsion of nuclear charges as the rare gas atom approaches the surface. A frequently employed model to calculate the interaction of a rare gas atom with a graphite or an alkali halide surface consists of summing two-body potentials between the adsorbing atom and the individual atoms or ions of the solid; a number of correction potentials are usually added.[6] A more microscopic approach is taken in the jellium model to describe He adsorption on metals.[7] It must be stressed that these models rest on a number of assumptions that are rather difficult to assess, such as separating the total energy into an attractive and a repulsive part which are calculated individually.

Theoretical work on field adsorption has been mostly phenomenological in nature.[2-5] For field ionization, one assumes model potentials and calculates electron tunnelling rates to account for the ionization probability of an atom approaching a surface.[8-12] To calculate the binding energy in field adsorption, one estimates the polarizability, hyperpolarizability, and field gradient contributions due to local field variations. Microscopic approaches to the problem of field adsorption are the jellium model employed by Kahn and Ying,[13] and a recent ASED-MO study for N_2 field-adsorbing on Fe(111).[14] In this chapter the latter approach is followed.

The study of field adsorption of rare gases on metals will start by modelling the adsorption of rare gases (in Sect.1a), within the ASED-MO theory,[15-18] as due to the formation of covalent bonds between a rare gas atom and a cluster of metal atoms. In Sect.1a the field effects are also dealt with, and a single particle potential seen by an electron is defined. In Sect.1b the numerical results for the adsorption of He, Ne, and Ar on W(111) in the presence of an electric field are presented. Here the electric field is assumed to be constant outside the metal, dropping to zero at the plane of the upper-most layer of the metal nuclei.

In Sect.2 of this chapter, a method is described in great detail to evaluate multicentre Coulomb integrals as used in Sect.1a. Some computational details and an integration technique are included, to save the computer time and memory involved in evaluating about 2000 such integrals to obtain one point on the electron-potential curve.

In Sect.3 the field penetration and oscillation of this field inside the metal due to the Friedel oscillation of the induced surface charge density is considered. Polarizability, hyperpolarizability and the field gradient terms are considered in the ASED-MO formalism.

a) Model :

(i) ASED-MO Approach

The atom superposition and electron delocalization molecular orbital (ASED-MO)[15-18] method is based on a molecular charge density partitioning model. For the sake of simplicity, the method is outlined for a diatomic molecule $\alpha+\beta$; the results can be generalized immediately to polyatomics and solids. One writes the electronic density, ρ, as[15]

$$\rho(\mathbf{r},\mathrm{R}_\alpha,\mathrm{R}_\beta) = \rho_\alpha(\mathbf{r},\mathrm{R}_\alpha) + \rho_\beta(\mathbf{r},\mathrm{R}_\beta) + \rho_{\mathrm{npf}}(\mathbf{r},\mathrm{R}_\alpha,\mathrm{R}_\beta) \tag{2.1}$$

where ρ_α and ρ_β are the electronic densities of the isolated atoms α and β, respectively. The remainder, ρ_{npf}, is called the non-perfectly-following density. According to electrostatics, the total energy of the molecule can be written as[16]

$$E(\mathbf{R}_\alpha,\mathrm{R}_\beta) = E_r + E_{\mathrm{npf}} \tag{2.2}$$

where

$$E_r(\mathbf{R}_\alpha,\mathrm{R}_\beta) = \frac{Z_\alpha Z_\beta}{|\mathbf{R}_\alpha - \mathbf{R}_\beta|} + Z_\beta \int \rho_\alpha(\mathbf{r}) \frac{1}{|\mathbf{r} - \mathbf{R}_\beta|} d\mathbf{r} \tag{2.3}$$

is the energy of nucleus β in the presence of a fixed atom α, and

$$E_{\mathrm{npf}}(\mathbf{R}_\alpha,\mathrm{R}_\beta) = -Z_\beta \int \int_\infty^{\mathbf{R}_\beta} \rho_{\mathrm{npf}}(\mathbf{r},\mathrm{R}_\alpha,\mathbf{R'}_\beta) \frac{d}{d\mathbf{R'}_\beta} \frac{1}{|\mathbf{r} - \mathbf{R'}_\beta|} d\mathbf{r} d\mathbf{R'}_\beta \tag{2.4}$$

accounts for the energy due to the rearrangement within the atoms in the presence of each other. Z_α and Z_β are the nuclear charges of the atoms α and β, respectively. For infinite separation of the nuclei, $E(\mathbf{R}_\alpha,\mathrm{R}_\beta)$ is the energy of the isolated atoms α and β. The size of E_r and E_{npf}, of course, depends on which of the two nuclei is fixed as the reference point; the total energy is, however, invariant. E_r is readily calculated from available single particle atomic wavefunctions. E_{npf} requires knowledge of ρ_{npf}, which is not available. It has been found[17] that a one-electron molecular orbital delocalization energy is generally a good approximation. A Hamiltonian that works well for this purpose shares some features common with the extended Hückel Hamiltonian.[19-21] The Extended Hückel Molecular Orbital (EHMO) method is a gradual modification of the Simple Hückel Molecular Orbital (SHMO) method and, in its present standard form, it is chiefly due to Hoffmann.[22] The major differences between this method and the SHMO method (originally developed to study the hydrocarbons) are: all valence orbitals on all atoms are included, not just $2p_z$ orbitals on sp^2 hybridized atoms of the π-framework; all off-diagonal elements are retained and the overlap is fully included; and energies are obtained as numerical quantities and not in terms of $\underline{\alpha}$ ($= H_{ii}$) and $\underline{\beta}$ ($= H_{ij}$) units. (H_{ij} is the Hamiltonian matrix element.)

The diagonal elements $H_{ii}^{\alpha\alpha}$ are set equal to the negative of the measured ionization energy of level i on atom α. The off-diagonal elements on the same atom are zero by orthogonality, i.e.

$$H_{ij}^{\alpha\alpha} = E_i^{\alpha} \delta_{ij} \quad . \tag{2.5}$$

The remaining off-diagonal elements are a modification of the extended Hückel formula

$$H_{ij}^{\alpha\beta} = \kappa\,(H_{ii}^{\alpha\alpha} + H_{jj}^{\beta\beta})\,S_{ij}^{\alpha\beta}\exp(-\alpha R_{\alpha\beta}) \tag{2.6}$$

with

$$S_{ij}^{\alpha\beta} = \langle\, \psi_i^{\alpha} \mid \psi_j^{\beta} \,\rangle \tag{2.7}$$

being the overlap integral between the i-th atomic orbital on atom α and the j-th orbital on β, the latter being a distance $R_{\alpha\beta}$ away. The exponential term, not present in the standard extended Hückel theory, has been introduced to improve predictions on molecular bond strengths; bond lengths and force constants are barely affected by this modification. Fitting bond strengths and lengths of first row diatomics, one determines the parameters in eqn.(2.6) to be $\kappa = 1.125$ and $\alpha = 0.13$ Å^{-1}. When this approximation to E_{npf} is used, results are generally more accurate if the two-body energy is calculated using the charge density of the more electronegative atom.

Summarizing, one can write the Hamiltonian, from which E_{npf} in eqn.(2.2) is calculated by diagonalization, as

$$H = \sum_{i\alpha} H_{ii}^{\alpha\alpha} \mid \psi_i^{\alpha} >< \psi_i^{\alpha} \mid + \sum_{\alpha\beta ij}' H_{ij}^{\alpha\beta} \mid \psi_i^{\alpha} >< \psi_j^{\beta} \mid \qquad (2.8)$$

where α and β enumerate the atoms in the cluster and i and j label the participating atomic orbitals.

There is an interesting additional consequence in partitioning the molecular charge density as discussed above. If one models ρ_{npf} as a set of fixed point charges, its contribution to the divergence of the electrostatic force on nucleus β is zero and one gets for the harmonic force constants[16,18]

$$k_e = 4\pi Z_{\beta} \rho_{\alpha}(R_e) = \left[\frac{\partial^2 E}{\partial R_{\beta}^2}\right]_{R_e} \qquad (2.9)$$

where R_e is the equilibrium distance. These, and higher order force constants, are typically within a few percent of experimental values.

(**ii**) Field Effects

The next task is to incorporate the effect of an electric field applied to a field emission tip. From the capacitance of parallel plates, one can estimate the charge q per surface atom, accumulated on a metal surface in the presence of a field F, to be of order

$$q = A\varepsilon_0 F = 0.055\ e\ F(\mathrm{V/\AA}) \tag{2.10}$$

Here A is the area per adsorption site, typically of the order of 10 $\AA^2$. Such surface charges are, indeed, generated in the present calculations.

To incorporate field effects in the ASED-MO approach, one adds the locally varying field energy of electrons and nuclei in the Hamiltonian (2.8)

$$H_{ij}^{\alpha\beta}(F) = \int \psi_i^{\alpha}(\mathbf{r})^* \, V_F(\mathbf{r}) \, \psi_j^{\beta}(\mathbf{r}) \, d^3\mathbf{r} \tag{2.11}$$

where the field potential is given by

$$V_F(\mathbf{r}) = e \int_{-\infty}^{\mathbf{r}} F(\mathbf{r'})\cdot d\mathbf{r'} \tag{2.12}$$

Additionally, one also adds the field energy of the nuclei

$$-\sum_{\alpha} \frac{Z_\alpha}{e} V_F(\mathbf{R}_\alpha) \tag{2.13}$$

where Z_α is the charge of the α-th nucleus at position $\mathbf{R}_\alpha$.

In eqn.(2.11) one writes

$$V_F(\mathbf{r}) = V_F(\mathbf{R}_\alpha) + V_F(\mathbf{r}) - V_F(\mathbf{R}_\alpha) \tag{2.14}$$

and gets

$$H_{ij}^{\alpha\beta}(F) = V_F(\mathbf{R}_\alpha)\, S_{ij}^{\alpha\beta} + \int \psi_i^{\alpha}(\mathbf{r})^* \, [V_F(\mathbf{r}) - V_F(\mathbf{R}_\alpha)] \, \psi_j^{\beta}(\mathbf{r}) \, d^3\mathbf{r} \tag{2.15}$$

The diagonal parts of the first term in eqn.(2.15) lead to the raising of the ionization energies in eqn.(2.5) by the field energy. With a varying electric field the field energy at a given nuclear position $\mathbf{R}_\alpha$ must be integrated out explicitly using eqn.(2.12). The off-diagonal parts of the first term in eqn.(2.15) are obviously proportional to the overlap integrals between atomic orbitals on different atoms. They, and the $\alpha \neq \beta$ contributions in the second term of eqn.(2.15), have been accounted for in the present model by modifying the Hückel-type hopping matrix elements in eqn.(2.6) by again raising the ionization energies via the field energy. This approximation seems to be the most natural in the context of an extended Hückel model and will be adopted throughout. For $\alpha=\beta$, the contributions due to the second term in eqn.(2.15) account for the atomic polarization.

In this section, it is assumed that the electric field is constant outside the metal, dropping to zero at the surface. The position of the vanishing of the field could be the classical image plane, assumed to lie about half an inter-planar lattice distance above the top-most ion cores and moving inward as the field increases. In Sect.3, the effect of the local field variations, relying on a recent jellium model calculations, have been studied in great detail. To emphasize electronic effects in field adsorption, namely, the changing character of the electronic bonds between the metal and the adsorbed species, one will, in this section, simplify the field aspect as far as possible by assuming that the electric field is given by a step function. The contributions due to the polarization term are also set aside for the moment. Although there is thus no direct effect of the electric field on the metal atoms, their electronic structure will be changed dramatically by the redistribution of electrons from the adsorbed species. This alone immediately leads to field-enhanced binding of rare gases.

Thus, to incorporate field effects in the ASED-MO model, one simply adds the energy term eFz (the origin of z being taken as the point where the field is supposed to drop to zero) to the Hamiltonian (2.8), so that

$$H_F = \sum_{\alpha i} \left[H_{ii}^{\alpha\alpha} + eFz_\alpha \right] |\psi_i^\alpha >< \psi_i^\alpha | + \sum_{\alpha\beta ij}{}' H'^{\alpha\beta}_{ij}(F) \, |\psi_i^\alpha >< \psi_j^\beta | - \sum_\alpha Z_\alpha F z_\alpha \qquad (2.16)$$

where

$$H'^{\alpha\beta}_{ij}(F) = \kappa \, (H_{ii}^{\alpha\alpha} + H_{jj}^{\beta\beta} + eFz_\alpha + eFz_\beta) \, S_{ij}^{\alpha\beta} \exp(-\alpha R_{\alpha\beta}) \quad , \qquad (2.17)$$

and z_α and z_β are the z components of the center of mass coordinate of the atoms α and β, respectively.

(iii) Rare Gases

To model the interaction between rare gas atoms and between a rare gas atom and some other species, the closed electronic shells are opened up by including 2p orbitals for He, 3d for Ne and Ar, 4d for Kr, and 5d for Xe. The oscillator strengths between these atomic orbitals are the greatest. These orbitals are taken to be of Slater type, to be discussed in detail in Sect.2. Ionization energies and Slater exponents[23,24] are adjusted to account for the dimer properties.[25] The data are listed in Table 2.1.

Table 2.1a: Ionization energies, E_I, and Slater exponents, δ, for the atomic orbitals of rare gases. Calculated and experimental dimer bond lengths, d, and binding energies, E_B, are also listed.

		E_I (eV)	δ($\AA^{-1}$)	d(Å)		E_B (eV)	
				Expt.	Theor.	Expt.	Theor.
He	1s	24.59	1.6875	2.96	2.92	0.001	0.001
	2p	3.5	1.4				
Ne	2s	48.47	2.4792	3.03	2.91	0.004	0.0015
	2p	21.56	2.4792				
	3d	4.0	2.0				
Ar	3s	29.24	2.086	3.7	3.6	0.012	0.013
	3p	15.85	2.086				
	3d	1.0	1.5				

Table 2.1b: Ionization energies, E_I, and Slater exponents, δ, for the atomic orbitals of a tungsten atom. The exponential terms in the d-orbitals are expressed as $C_1\exp(-\delta_1 r)+C_2\exp(-\delta_2 r)$. Also given is the initial occupation of the various orbitals.

	E_I (eV)	δ_1($\AA^{-1}$)	δ_2($\AA^{-1}$)	C_1	C_2	initial occupation
6s	8.0	2.641				1
6p	5.6	1.841				0
5d	9.0	4.982	2.068	0.6685	0.5424	5

(**iv**) Electron Potential

So far, the calculation of the total interaction energy of a rare gas atom with a metal cluster in the presence of an electric field has been outlined. To eventually compute the ionization probability for a rare gas atom at a field-ion emission tip, one also needs the potential energy of an electron. This is readily calculated from the molecular orbitals according to

$$V_e(\mathbf{r}) = - e \int \frac{\rho(\mathbf{r}')}{|\mathbf{r}-\mathbf{r}'|} d\mathbf{r}' + e F r\cos\theta \, \Theta(r\cos\theta) \qquad (2.18)$$

where θ is the angle between $\vec{F}$ and $\vec{r}$, and $\Theta(x)$ is a step function. The cluster charge density is given by

$$\rho(\mathbf{r}') = \sum_{\alpha} Z_\alpha \, \delta(\mathbf{r}'-\mathbf{R}_\alpha) - e \sum_{\nu} n_\nu \, |\Phi_\nu(\mathbf{r}')|^2 \; . \qquad (2.19)$$

Thus one gets

$$V_e(\mathbf{r}) = - e \sum_{\alpha} \frac{Z_\alpha}{|\mathbf{r}-\mathbf{R}_\alpha|} + e^2 \sum_{\nu} n_\nu \int |\Phi_\nu(\mathbf{r}')|^2 \frac{d\mathbf{r}'}{|\mathbf{r}-\mathbf{r}'|}$$

$$+ e F r\cos\theta \, \Theta(r\cos\theta) \qquad (2.20)$$

The summation over ν includes all molecular orbitals Φ_ν which are obtained by diagonalizing the Hamiltonian (2.8) or (2.16); n_ν is the molecular orbital occupation number. It is interesting to note that there is no noticeable numerical difference whether one sums in eqn.(2.20) over all electrons in the cluster or excludes the one associated with the tunnelling process. The molecular orbitals can be expressed in terms of the atomic orbitals as

$$\Phi_{\nu}(\mathbf{r}) = \sum_{\alpha i} C_{\nu}^{\alpha i} \psi_{i}^{\alpha}(\mathbf{r}-\mathbf{R}_{\alpha}) \qquad (2.21)$$

Because the Slater orbitals of atom α are centered around the nucleus α at position $\mathbf{R}_{\alpha}$, it is necessary in eqn.(2.20) to evaluate two- and three-center Coulomb integrals. This will be outlined in detail in Sect.2.

b) Results :

(i) He - W

For He adsorption on one-fold sites (i.e., on top of W atoms), there is a relatively strong covalent donation bond between the filled He 1s orbital and the empty W 6p band. There are two additional weaker but stabilizing donation interactions, this time from the W 5d to the empty 2p orbitals on He. As a He atom approaches the surface, these interactions increase, as shown in Fig.2.1 for the W-He dimer (similar interactions occur with W_4). The total orbital energy for the dimer is plotted as a function of distance in Fig.2.2. Clearly, as the height of the He atom above the surface decreases, the overlap giving rise to these interactions increases (as shown in Fig.2.1), with the result that the orbital energy stabilization accelerates rapidly. The stabilization of each of the orbitals is in a manner proportionate to the overlap in the second-order expression

$$E^{(2)} = \frac{|\langle\psi_a |H'| \psi_b \rangle|^2}{E_a - E_b} , \qquad (2.22)$$

where ψ_a and ψ_b are the basis functions for the separated atoms, H' is

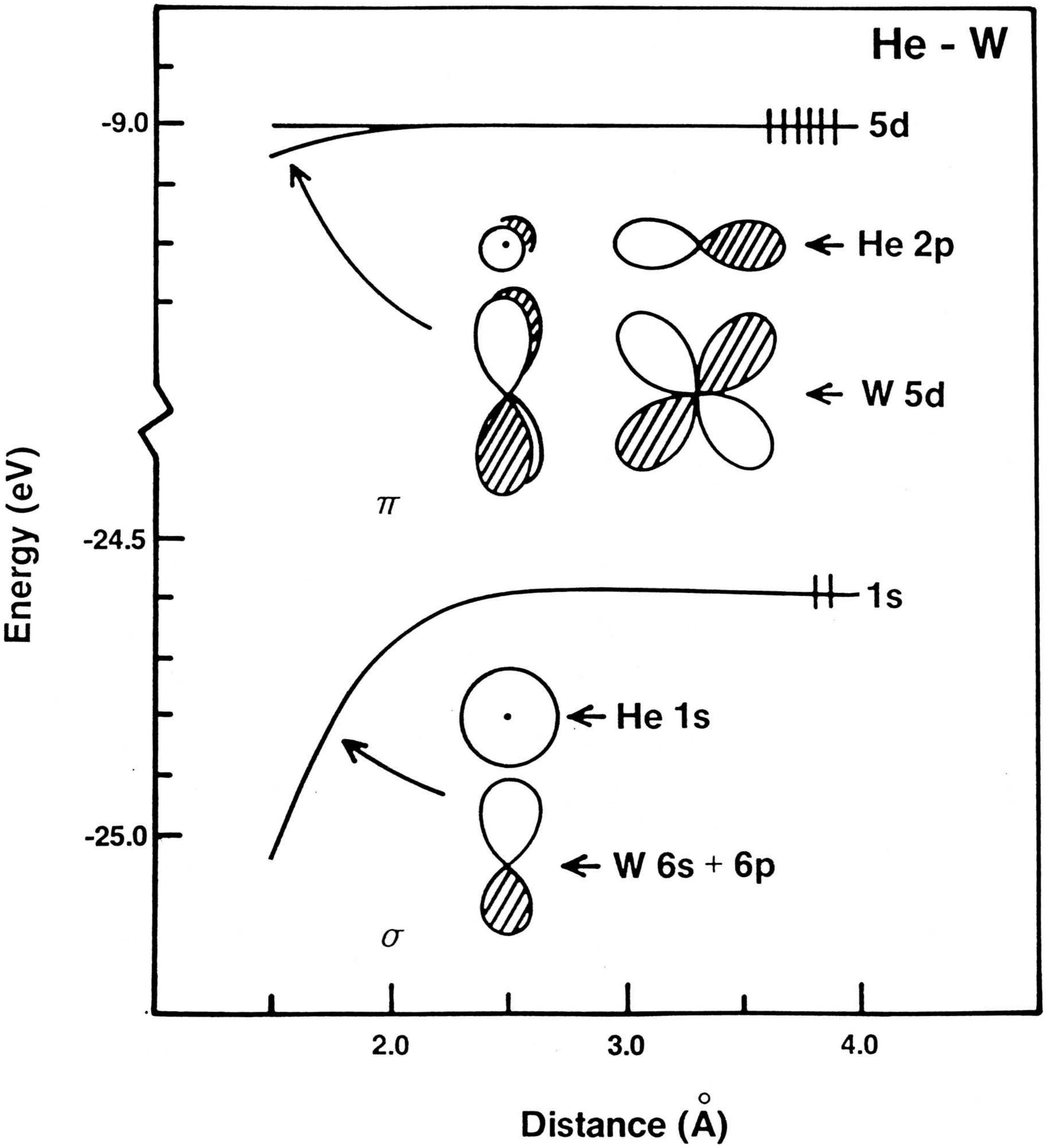

Fig.2.1: Dependence of energy levels of filled orbitals on internuclear distance for diatomic He-W.

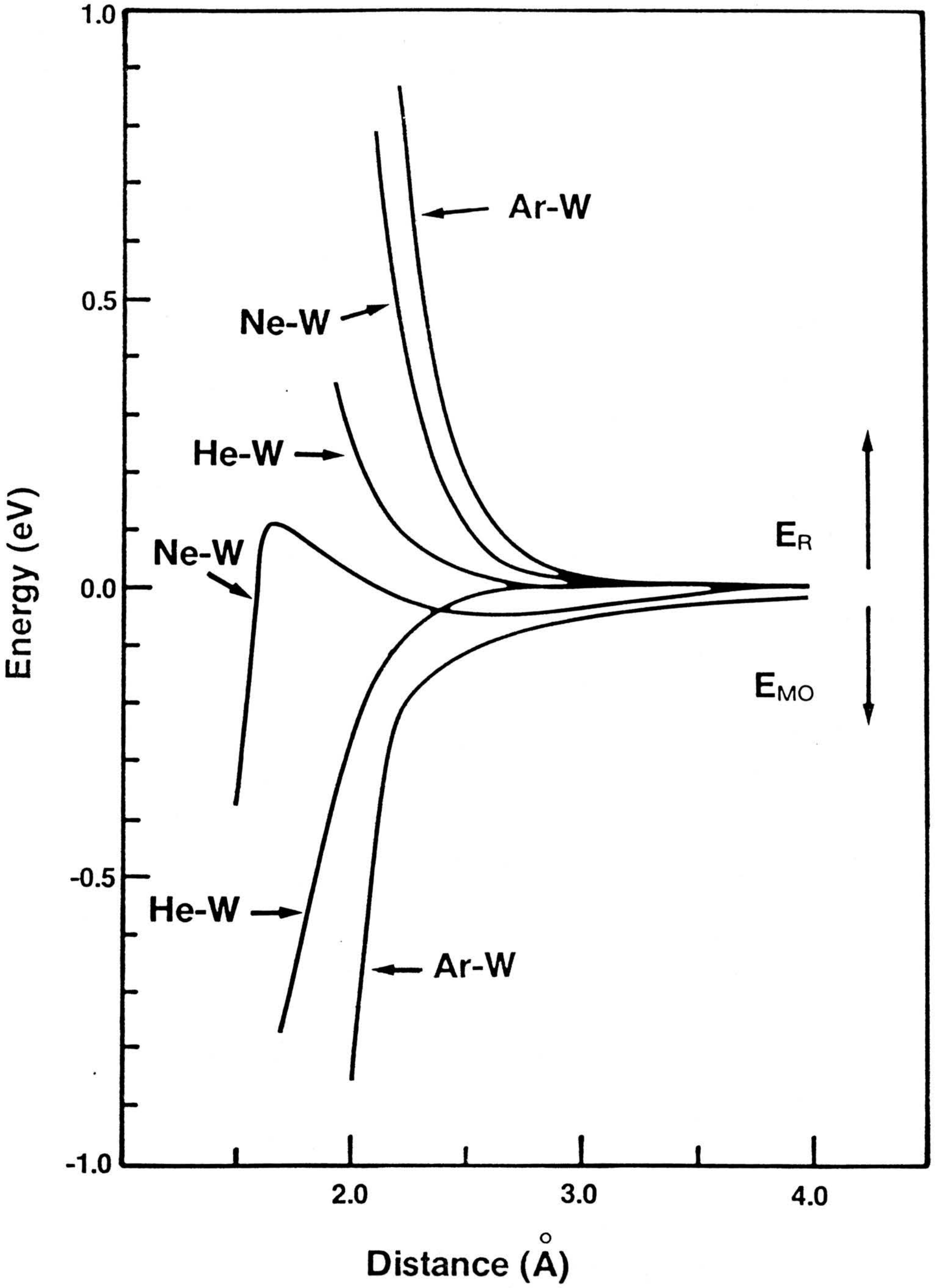

Fig.2.2: Two-body repulsive (E_r) and orbital (E_{MO}) energies of rare gas-tungsten diatomics as a function of internuclear distance.

the perturbation between them, and E_a and E_b are the respective eigenvalues. In the case of He 1s donation $E^{(2)}$ is negative because $E_{1s} < E_{6p}$. For each of the bonding interactions shown in Fig.2.1, there will be an anti-bonding counterpart orbital which is destabilizing because the sign of the energy denominator changes. For example, the anti-bonding counterpart to the He 1s + W 6p σ donation stabilization is shifted up within the empty W 6p band and, being empty according to the low-spin assumption, does not detract from the binding stabilization.

When the extravalent (empty) He 2p orbitals are excluded from the basis set, there are only small changes in the binding. The equilibrium height of He is unchanged within 0.1 Å, and the dissociation energy decreases by about 5 percent. The participation of the extravalent orbitals is small because of the large energy denominator in the perturbation expansion and the weak overlap of these orbitals with W orbitals.

The two-body repulsion energy increases as the height above the surface decreases, as shown in Fig.2.2. In this case, E_r is calculated using the charge density function of W and the nuclear charge of He. The increase is a consequence of the penetration of the electronic charge cloud of W by the He nucleus so that the influence of the nuclear repulsion term increases. The total potential energy of He interacting with a W(111) cluster, as calculated in the ASED-MO approximation, is given in Fig.2.3 for four different clusters, and also for the He-W dimer. The W_4 cluster has a near tetrahedral structure with He adsorbed above its apex. In the W_{7s} cluster, all the seven W atoms are from the surface layer, i.e. six atoms surrounding one in the center. The W_{7b} is enlarged by adding three below the base plane of the W_4 tetrahedron. In

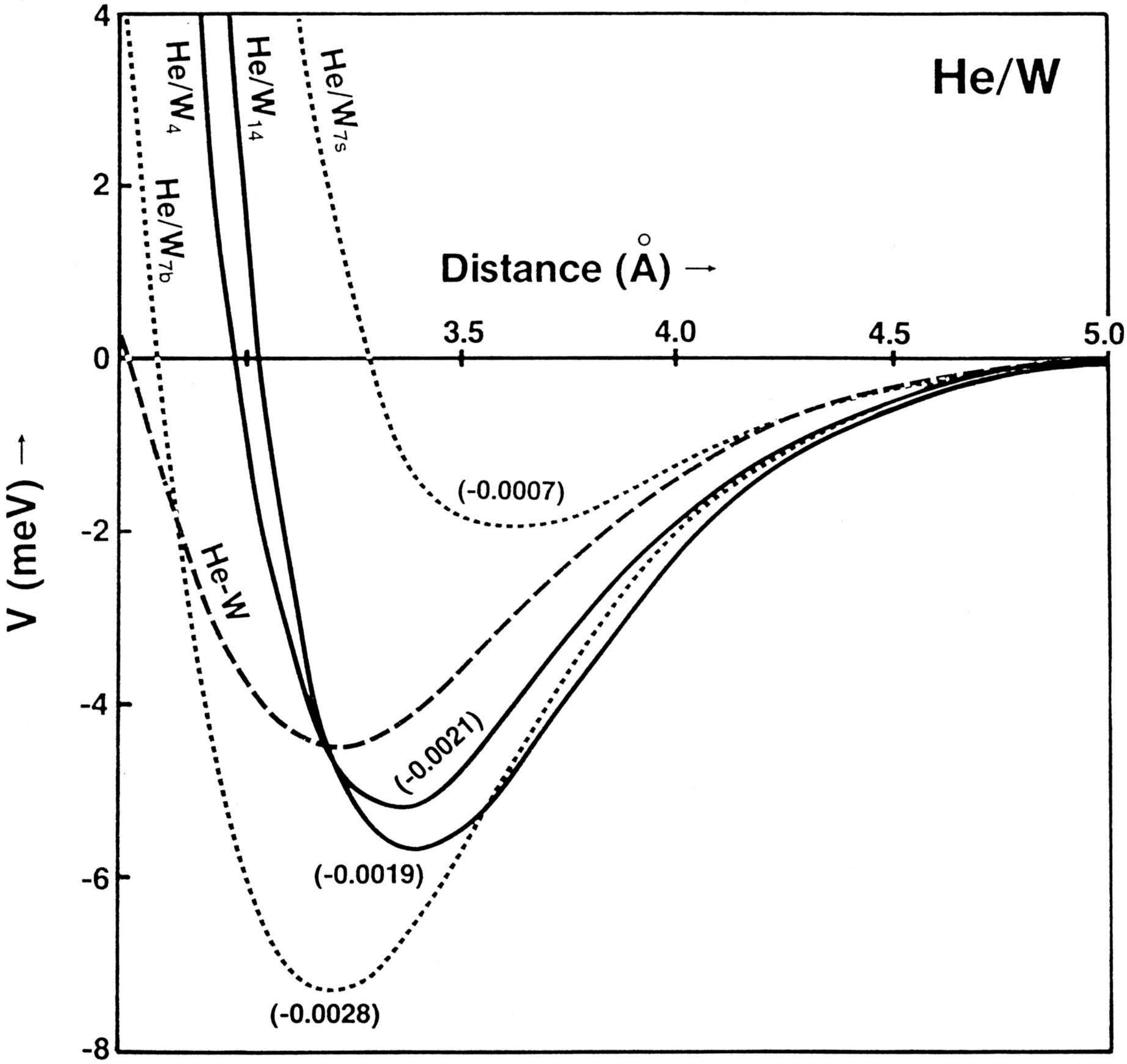

Fig.2.3: Potential energy of He interacting with various W clusters (as described in Sect.1b(i)) in zero field. Numbers in the parentheses give the charge on the He atom at the equilibrium position.

the W_{14} cluster, one has included seven more atoms to the W_{7b} cluster, with six from the surface layer, surrounding the top-most atom, and adding one W atom from the fourth layer nearest to it. In chapter III an arrangement of the W(111) surface atoms is shown. W_{14} is the cluster which includes considerable amount of surface atoms close to the adsorbing atom, and the nearest, next nearest and next-next nearest atoms of the surface W atom nearest to the adsorbing atom. The good agreement between the W_4 and the W_{14} results justifies the use of the W_4 cluster for the most of the text. The potential energy for He has a minimum at a distance of 3.33Å, with a depth of 5 meV, in good agreement with experimental results for He adsorption on metal surfaces. One should stress that binding energies calculated within the ASED-MO theory are not too accurate and may be off by as much as a factor of two; however, bond lengths are quite accurate. One notes that at the minimum there is a charge transfer of about -0.002e to the He atom.

He adsorption on the W_4 cluster in the presence of an electric field is discussed next. Within the current field model, the 1s and 2p ionization potentials decrease as the height above the surface increases (see eqn.(2.16)). The result is that the He 1s orbital level moves closer to the resonance with the W 5d band so that, according to the energy denominator in eqn.(2.22), the binding stabilization will increase. Similarly, the W s-d back-donation to the empty He 2p orbitals decreases. The strengthened σ interaction in the presence of a field is the cause of the strengthening of the bond to the surface, as shown in Fig.2.4. This strengthening is manifested in the increased activation energy, the decreased equilibrium internuclear distance, and the increased curvature near equilibrium, i.e. the force constant. The

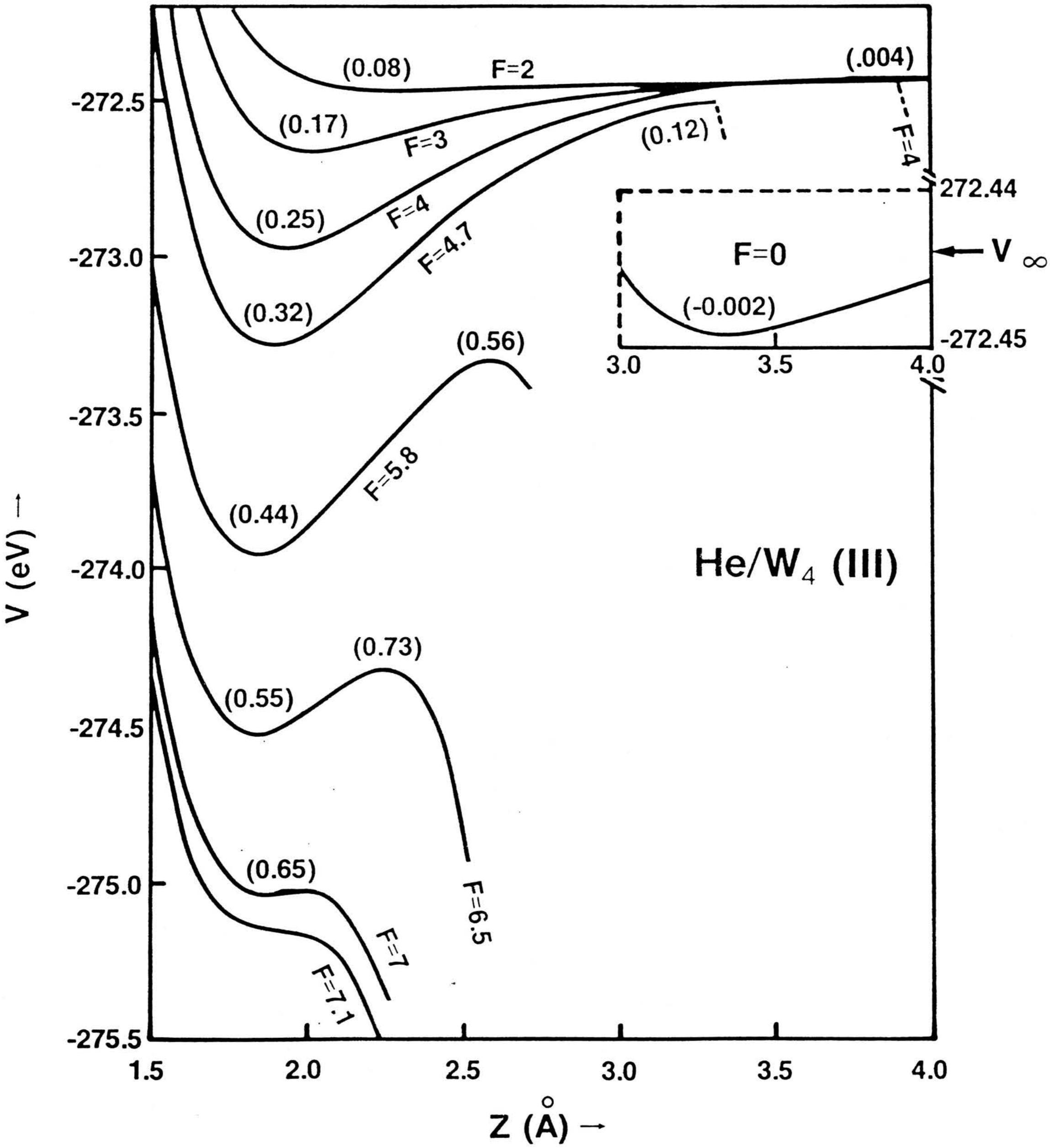

Fig.2.4: Potential energy of He interacting with a W_4 cluster for various electric field strengths F in V/Å. The broken lines are the potential energy for a He ion. Numbers in parentheses give the charge on the He atom at the equilibrium position.

activation energy is defined as the energy difference between the bottom of the adsorption energy well and the top of the activation barrier (also known as the Schottky barrier). In zero field it is equal to the binding energy of the adsorbed species. The dashed portion of the energy curves for large distances represents the energy for a He^+ ion. An ion can form at a distance at which the He 1s ionization energy is raised by the field energy eFz above the W 5d level. Whether ionization, indeed, occurs at that distance depends, in addition, on the ionization probability connected with the ability of an electron initially located on the He to tunnel through the potential barrier separating it from the metal band. We will return to this point in a moment.

To quantify the discussion of He field adsorption further, the position, z_{min}, of the (local) minimum in the energy curves (as shown in Fig.2.4), the activation energy Q, and the charge transfer, Δq, to or from the adsorbed He have been plotted in Fig.2.5. Fig.2.5a shows a drastic decrease in z_{min} around field strengths of 1.5 - 2 V/Å, from 3.3 Å to less than 2 Å. Ignoring the dotted curves for the moment, one sees that this is accompanied by a substantial increase in activation energy, from 5 meV in zero field to more than 600 meV at a field of 5 V/Å, decreasing rapidly beyond that point. Concurrently, the He atom acquires a charge of about 0.5 e. The reasons for this transition of He physisorption in zero field to chemisorption in a strong field have been analysed above.

In setting up a model for field adsorption in Sect.1a, it has been assumed that the electric field is totally excluded from the metal cluster. This is obviously oversimplified as such a situation should, for instance, not allow for field evaporation of metal ions. There must be

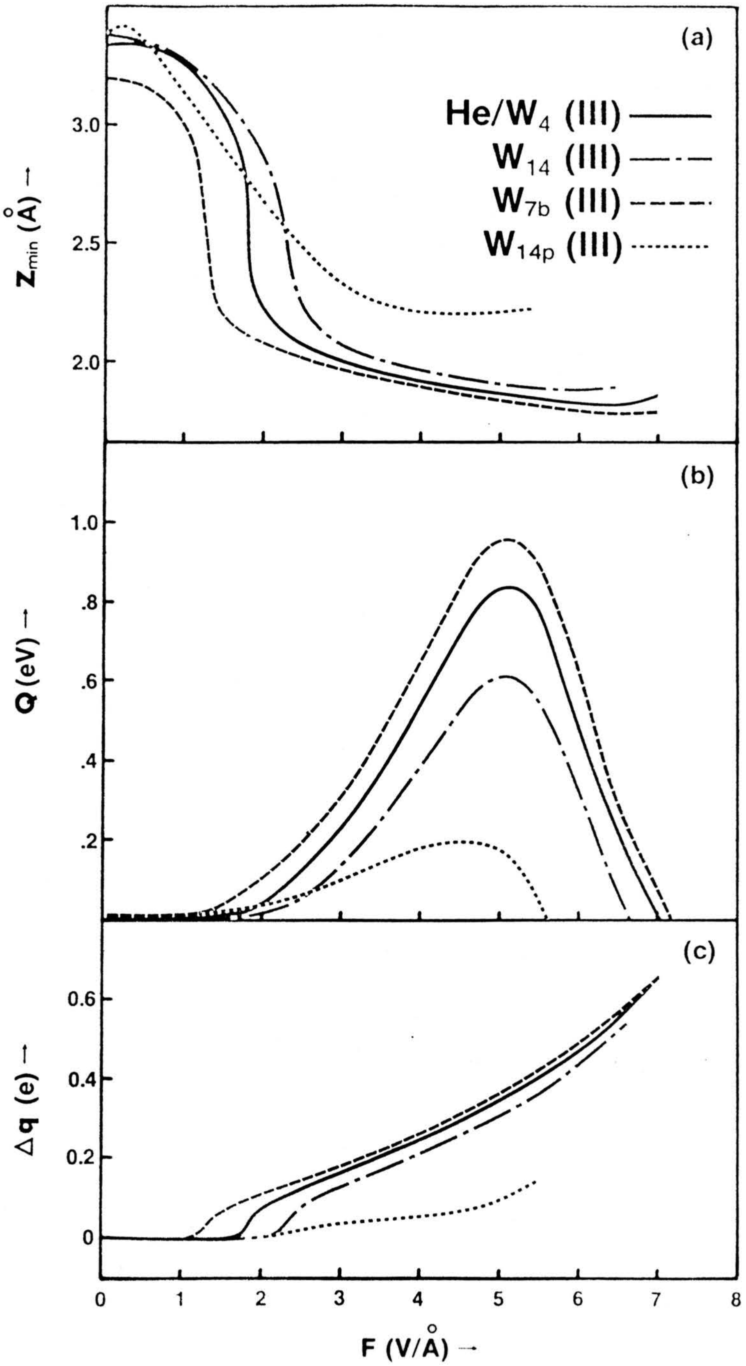

Fig.2.5: The position z_{min} of the potential minimum in Fig.2.4, the activation energy Q and the charge transfer Δq as a function of field strength for He interacting with various W clusters which are described in Sect.1b(i). W_{14p} is the W_{14} cluster with the zero of the field taken at -0.6 Å.

some field penetration into the metal which should, in principle, be included self-consistently.[26-28] Instead, one resorts here to a simple prescription by putting the origin of the electric field a distance a_F on the inside of the top-most metal atom of the cluster rather than at its center. To get an estimate of a_F, one notes that the field strength for field evaporation of W is about 5.5 V/Å. Therefore, if one demands that the activation barrier for He field adsorption disappears at this field strength rather than at about 7 V/Å, as suggested by the present calculations, one gets a_F of the order of 0.6 Å. The resulting equilibrium positions, activation energies and charge transfers for He field adsorption on a W_{14} cluster are given in Fig.2.5 as dotted curves. One notes in particular that the increase in activation energy is only of the order of maximally 200 meV and that the charge transfer also remains much smaller. This ad hoc procedure clearly demonstrates the importance of field penetration and points to the necessity to develop a self-consistent theory.

In field-ion emission microscopy, one usually defines a best image potential or field F_b at which the image is clearest. Within a theoretical framework, it would be identified with the field at which the break in the potential energy curve from neutral atom to ion occurs close enough to the surface to insure a high electron tunnelling probability and a clear image at the same time. As the present theory provides, so far, only adiabatic energy curves, one resorts to identifying the best image field as that at which the Schottky barrier is located at the distance of the potential minimum in the field-free case. For He this field is around 4.7 V/Å, in good agreement with experimental estimates of somewhat larger than 4 V/Å.

It has been hinted repeatedly that for a full understanding of the field-ion emission process, it is mandatory to calculate the tunnelling probability of an electron initially located on an atom approaching a surface from the gas phase into the valence band of the metal. In the simplest model, this calculation would be performed in a crude single particle picture. The single electron potential energy curves have therefore been calculated for the He-W_4 system according to eqn.(2.20). The results are presented in Fig.2.6. In zero electric field the ASED-MO theory predicts a single electron potential around the He nucleus that is very close to an unscreened Coulomb potential. Near the surface of the metal cluster, a potential trough appears around the nucleus of the top-most W atom. Note that in a jellium type model one would expect the bottom of the conduction band to rise within an angstrom or so at a distance of about half an interplanar distance above the top-most layer. The dashed curve in Fig.2.6a represents such a simple model, with the electron potential rising abruptly at the metal surface and becoming a Coulomb potential around the He nucleus. Fig.6b shows the electron potential in a field of 3 V/Å; nothing unexpected happens. However, a drastic change occurs at the critical field of 4.7 V/Å. Just below this field strength there is still a well-defined potential barrier between the He and metal regions, thus localizing an electron on the adsorbed He atom. At the critical field this barrier disappears completely as a result of hybridizing and delocalizing the He wavefunction. It has also been found that at the positions of the potential minima in the activation energy curves in Fig.2.4 there is no potential barrier for the electrons. One thus concludes that, in the critical field, a He atom at the critical distance will ionize instantly.

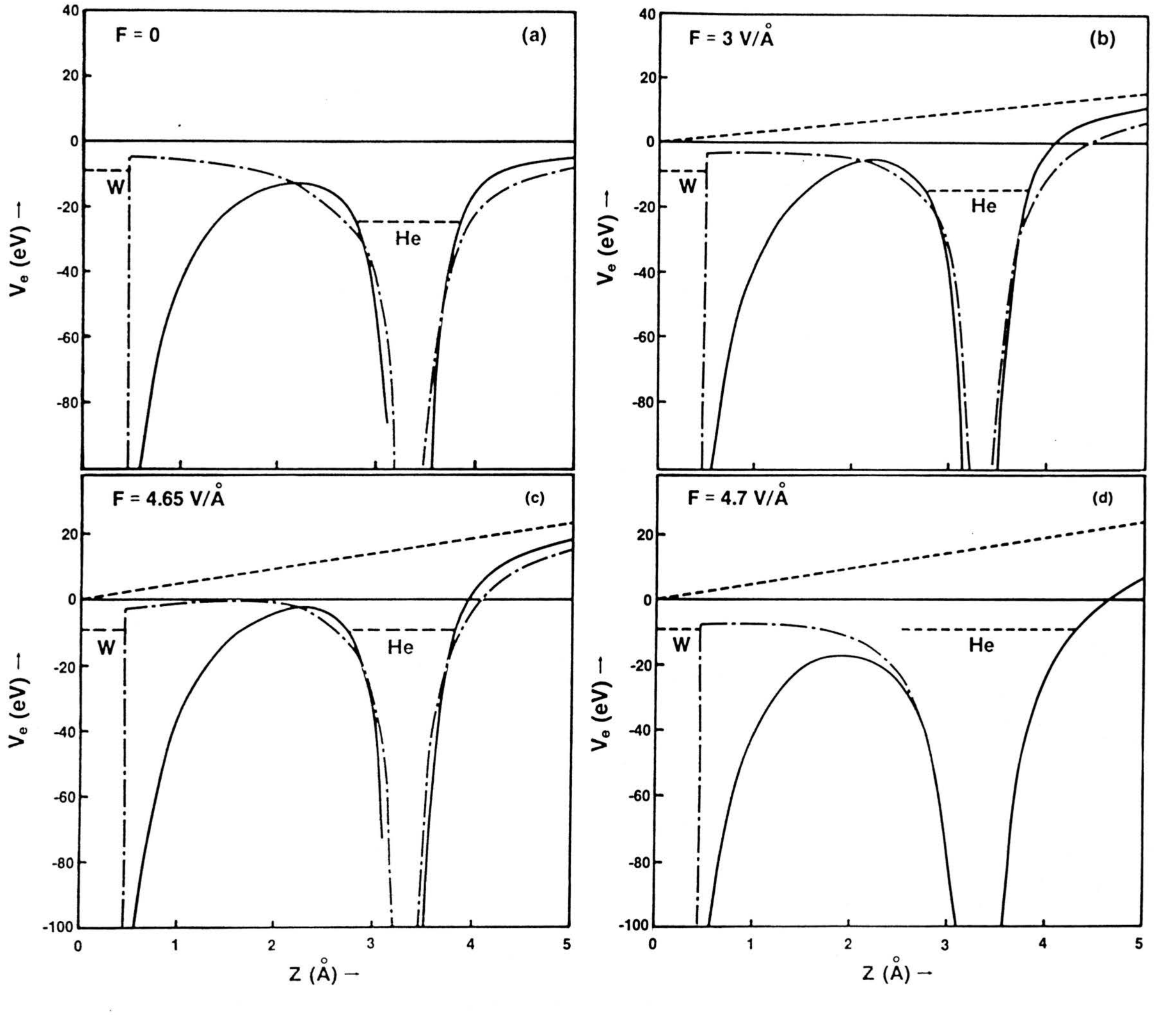

Fig.2.6: The one-electron potential (2.20) for the He-W_4 system at various field strengths. The dot-dashed curve is the unscreened Coulomb potential plus the field term eFz (dashed curve). In Fig.(d) the charge taken for the unscreened Coulomb potential is 2e.

A small distance further out, or at a field slightly below critical, however, the electron has to penetrate a barrier. For example, at a field of 4.65 V/Å an electron on a He atom 3.3 Å above the surface encounters a barrier depicted in Fig.2.6c. The tunnelling probability in the WKB approximation has been calculated to assess the quality of the model barrier consisting of a stepped jellium edge, a linear electric potential and a Coulomb potential around the He nucleus. It is found that the tunnelling rate through this model barrier is too small, by an order of magnitude, indicating that some care must be taken to set up such phenomenological models.[10-12]

(ii) Ne and Ar

Ne and Ar adsorption onto the W cluster are similar to one another, but somewhat different from He. Again, the inert gas filled valence s orbital donates to W s-p-d hybrid orbitals, as shown in Figs 2.7 and 2.8. Over most of the range of z values this is a stabilizing interaction. The filled Ne and Ar valence p orbitals are involved in important p + W-d π donation interactions. The gas p_z orbital donates to the W 6s-5d, and its anti-bonding counterpart is empty at all but small z values. The gas p_x and p_y orbitals donate to W d,p hybrid orbitals and there is a weak δ stabilization of the W $d_{x^2-y^2}$ and d_{xy} orbitals by the high-lying empty gas d orbitals at small z. Two electrons go into an antibonding orbital, a π^* composed of W 5d and a Ne 3d,2p hybrid. This rises rapidly at small z values, causing the total orbital energy in Fig.2.2 to begin to rise slowly at a value of 2.5 Å, but at 1.6 Å this orbital crosses the more slowly rising σ^* and donates its electrons into

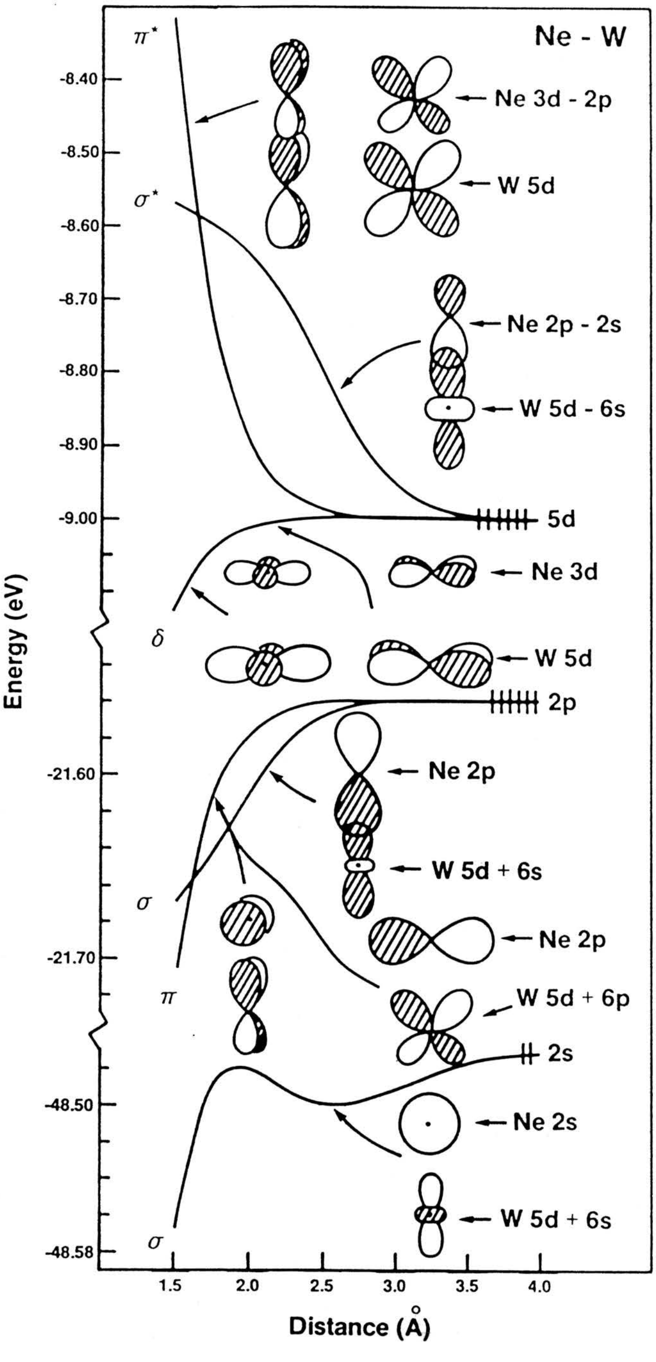

Fig.2.7: Dependence of energy levels of filled orbitals on internuclear distance for diatomic Ne-W. Doubly degenerate π^* orbitals are half filled.

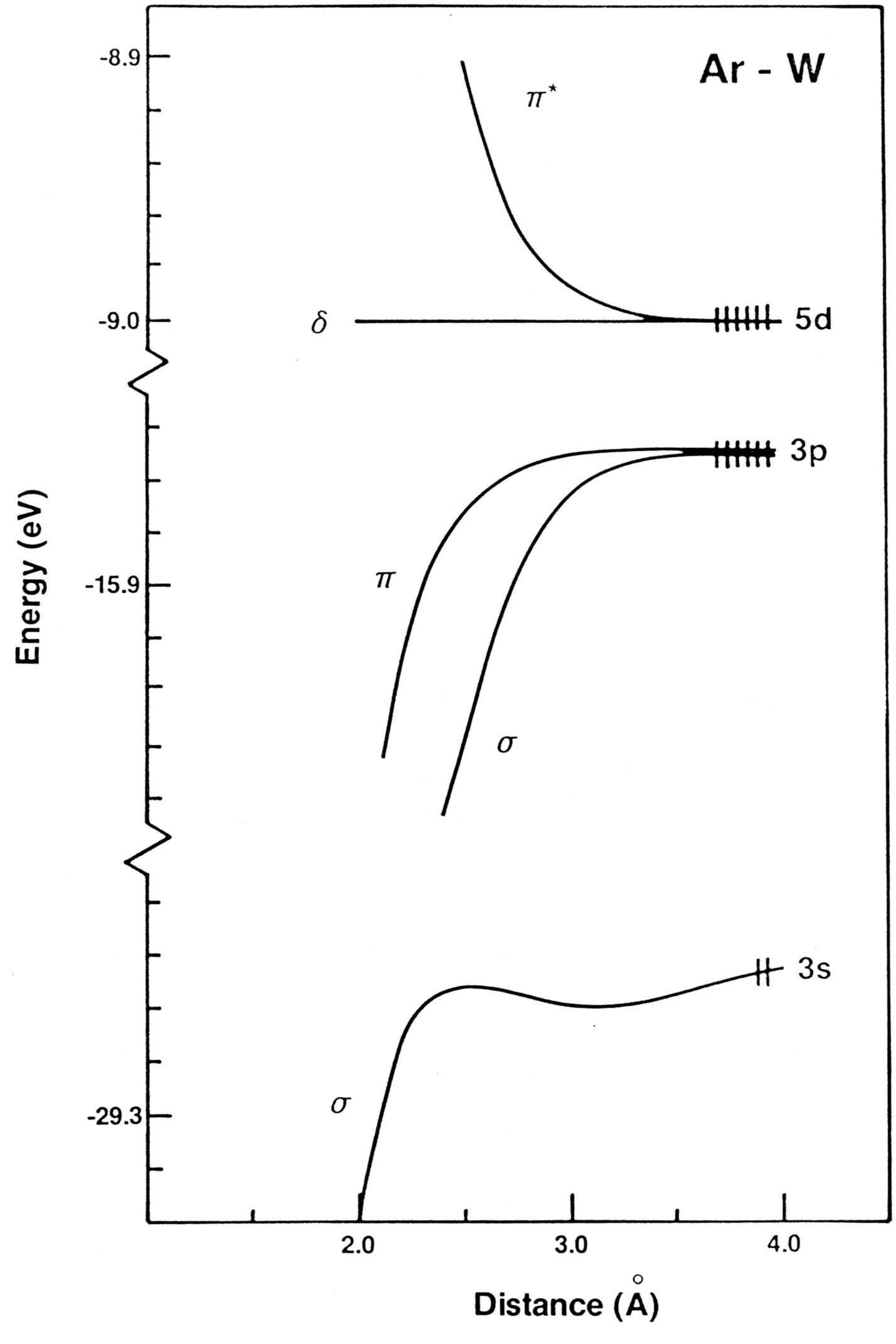

Fig.2.8: Dependence of energy levels of filled orbitals on internuclear distance for diatomic Ar-W. Doubly degenerate π^* orbitals are half filled.

the latter. This allows the total orbital energy to begin to drop again, as shown in Fig.2.2. The σ^* orbital shows its rise with decreasing z because the high-lying Ne $3d_{z^2}$ orbital begins to mix in a stabilizing way. The orbital interactions are greater for Ar than for Ne because of the greater size of Ar valence s and p orbitals, as evident by comparing Figs 2.7 and 2.8. The total orbital stabilization energy is therefore larger for Ar, as evident from Fig.2.2, but the two-body repulsion energy is also higher for Ar. The total binding energy curves have depths 35 meV for Ne and 33 meV for Ar. Whereas the He and Ne binding energies at their equilibrium distances are in good agreement with experimental values, the binding energy for Ar is too small by a factor of three. Binding energies for He, Ne and Ar on metals are approximately 5 meV, 30 meV and 100 meV, respectively.[29]

For Ne and Ar, the presence of a field strengthens the adsorption bonds, for reasons similar to those discussed for He. As the field is increased, the equilibrium distances from the surface decrease for all these inert gas molecules, but as each bond is stretched at high field strengths, dissociation to ions takes place, as shown in Figs 2.9 and 2.10, for the potential energy curves. Despite the dissociation, the covalent bonds are strong if one considers their strengths from the point of view of overlap populations. Table 2.2 shows how the reduced overlap populations,[21,30] defined with the help of eqns (2.7) and (2.21), as

$$\rho^{\alpha\beta} = 2 \sum_{ij\nu} n_\nu \, C_\nu^{\alpha i} \, C_\nu^{\beta j} \, S_{ij}^{\alpha\beta} \quad ; (\alpha \neq \beta) \qquad (2.23)$$

increase for each gas for the short equilibrium heights which one

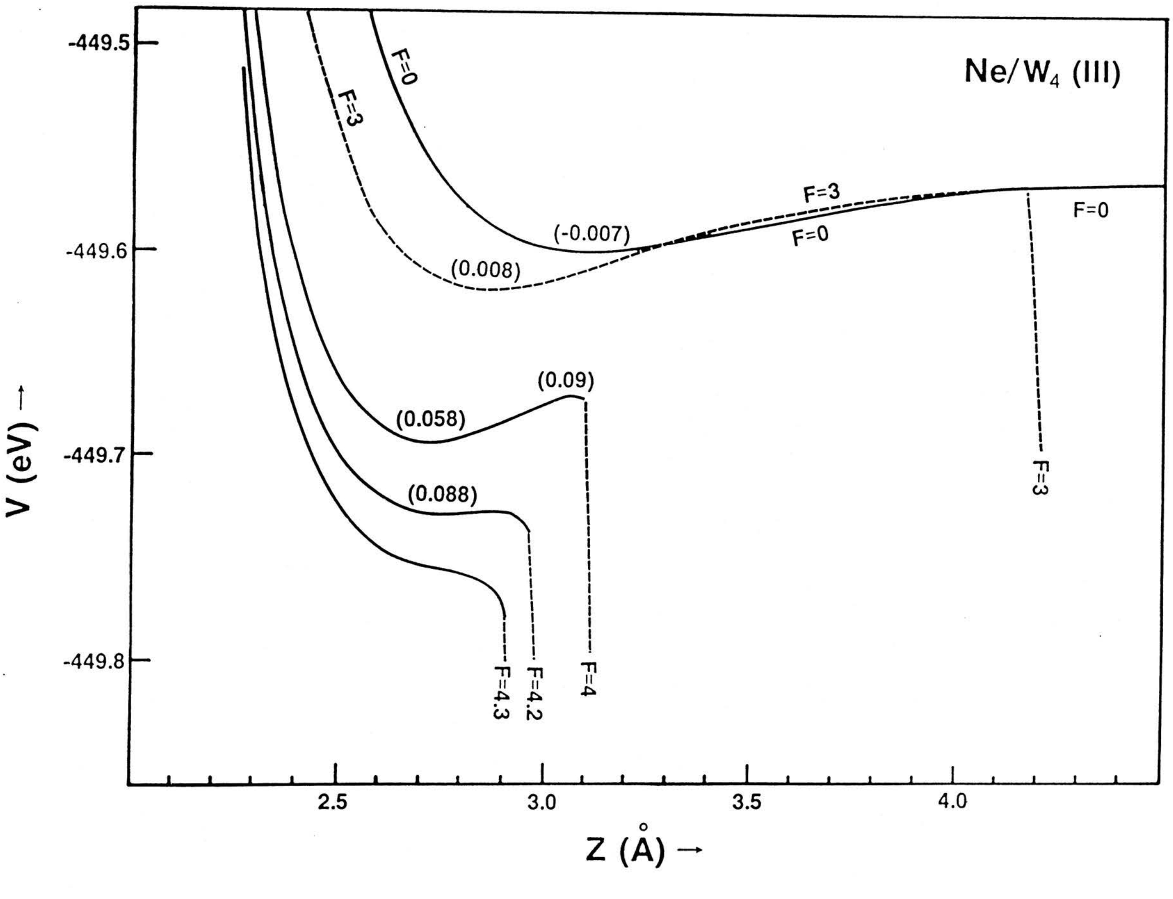

Fig.2.9: Potential energy of Ne interacting with a W_4 cluster for various electric field strengths F in V/Å. The broken lines are the potential energy for a Ne ion. Numbers in parentheses give the charge on the Ne atom at the equilibrium position.

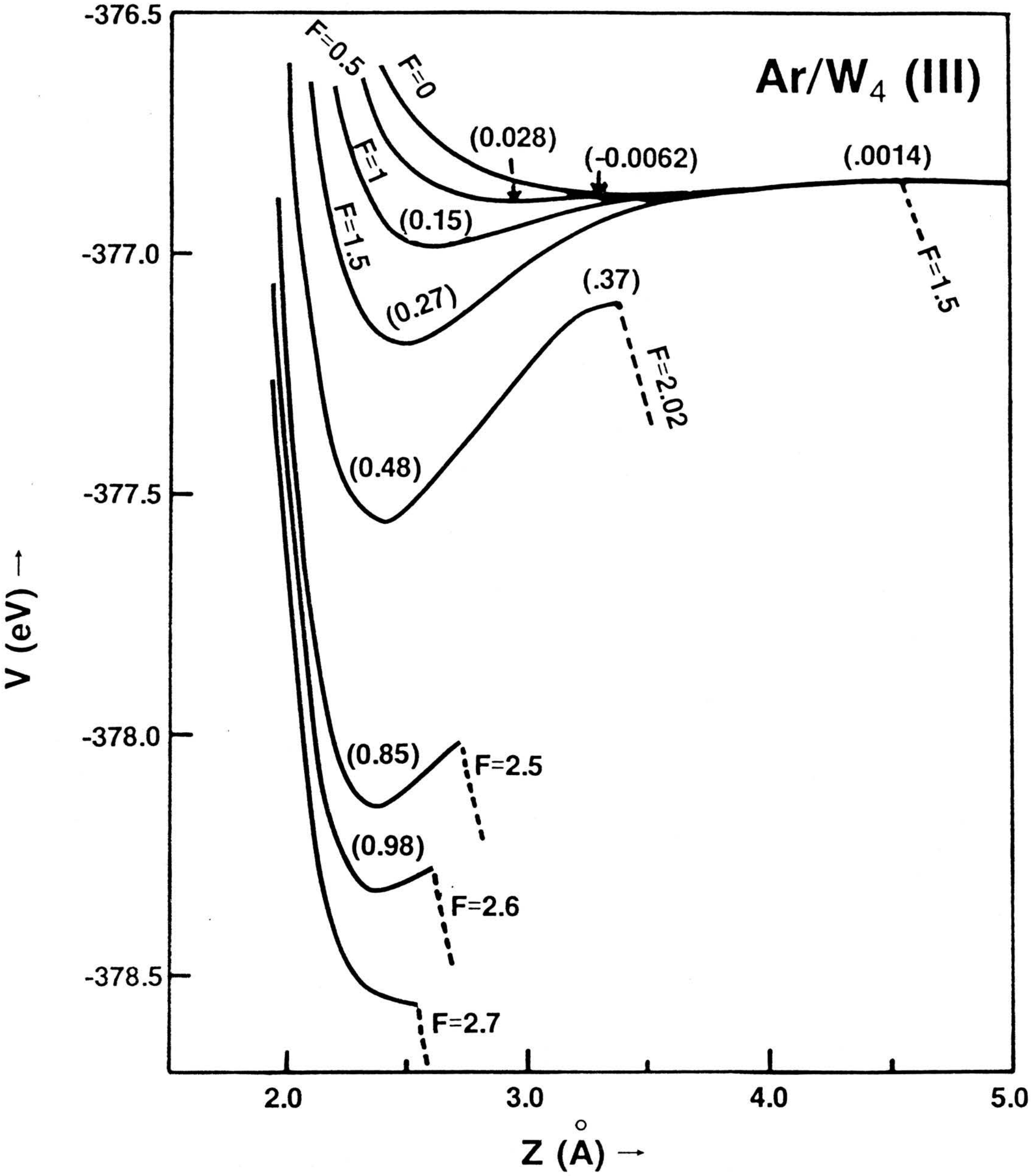

Fig.2.10: Potential energy of Ar interacting with a W_4 cluster for various electric field strengths F in V/Å. The broken lines are the potential energy for an Ar ion. Numbers in parentheses give the charge on the Ar atom at the equilibrium position.

Table 2.2: Reduced overlap populations, $\rho^{\alpha\beta}$, from eqn.(2.23) between rare gases and the nearest W atom for various fields in the equilibrium configurations.

	F(V/Å)	z_{min}(Å)	$\rho^{\alpha\beta}$
He	0	3.33	-0.0047
	2.0	2.18	0.0542
	4.0	1.92	0.1368
	4.7	1.87	0.1481
	5.8	1.83	0.1485
	7.0	1.85	0.1492
Ne	0	3.08	-0.0158
	3.0	2.86	-0.0134
	4.0	2.70	0.0121
	4.2	2.72	0.0243
Ar	0	3.39	-0.0287
	0.5	2.95	-0.0054
	1.0	2.60	0.1085
	1.5	2.48	0.2104
	2.0	2.39	0.3384
	2.6	2.37	0.4897

The values are good only to two significant figures. However, these figures are retained for comparisions.

predicts for high field strengths. Reduced net atomic orbital (AO) population for the atom α is defined as

$$q^{\alpha}_{net} = \sum_{i\nu} n_{\nu} \, |c_{\nu}^{\alpha i}|^{2} \tag{2.24}$$

The charge on the atom α, as calculated in the text, is obtained from Mulliken's definition[21,30] of reduced gross AO population which is given in terms of reduced AO and overlap populations as

$$q^{\alpha}_{gross} = q^{\alpha}_{net} + \frac{1}{2} \sum_{\beta} \rho^{\alpha\beta} \tag{2.25}$$

To survey the field-adsorption characteristics of Ne and Ar, one again plots in Figs 2.11 and 2.12 the equilibrium positions, activation energies, and charge transfers for Ne and Ar, respectively, as a function of field strength. Again one notes that the equilibrium distance decreases drastically for fields around 3 and 1 V/Å for Ne and Ar, respectively, but not as much as for He. For Ne the activation energy rises by a factor of 2, for Ar by a factor of 10; recall that it was a factor of 100 for He without field penetration and a factor of 40 with field penetration. The effect of the latter on the adsorption of Ne and Ar is again indicated by dotted curves in Figs 2.11 and 2.12. The charge transfer for Ne is significantly smaller than for He. This stunning difference in field adsorption between He and other rare gases has a very simple explanation in the much larger ionization potential for He. A He atom remains field adsorbed to much higher fields before its valence levels get lifted above the empty W levels, so that the hybridization can take place, leading to typical chemisorption features.

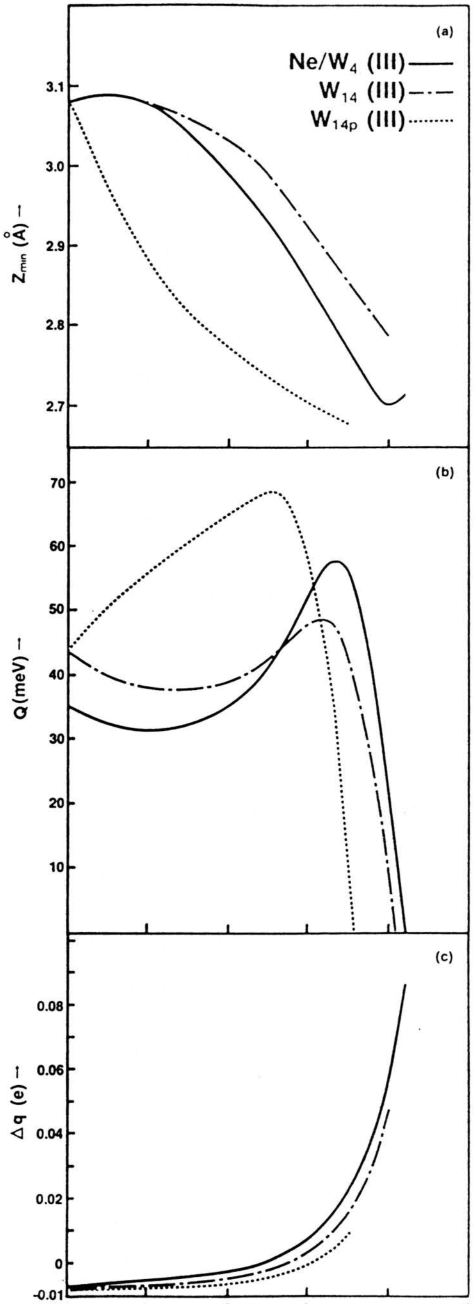

Fig.2.11: The position z_{min} of the potential minimum in Fig.2.9, the activation energy Q and the charge transfer Δq as a function of field strength for Ne interacting with various W clusters which are described in Sect.1b(i). W_{14p} is the W_{14} cluster with the zero of the field taken at -0.6 Å.

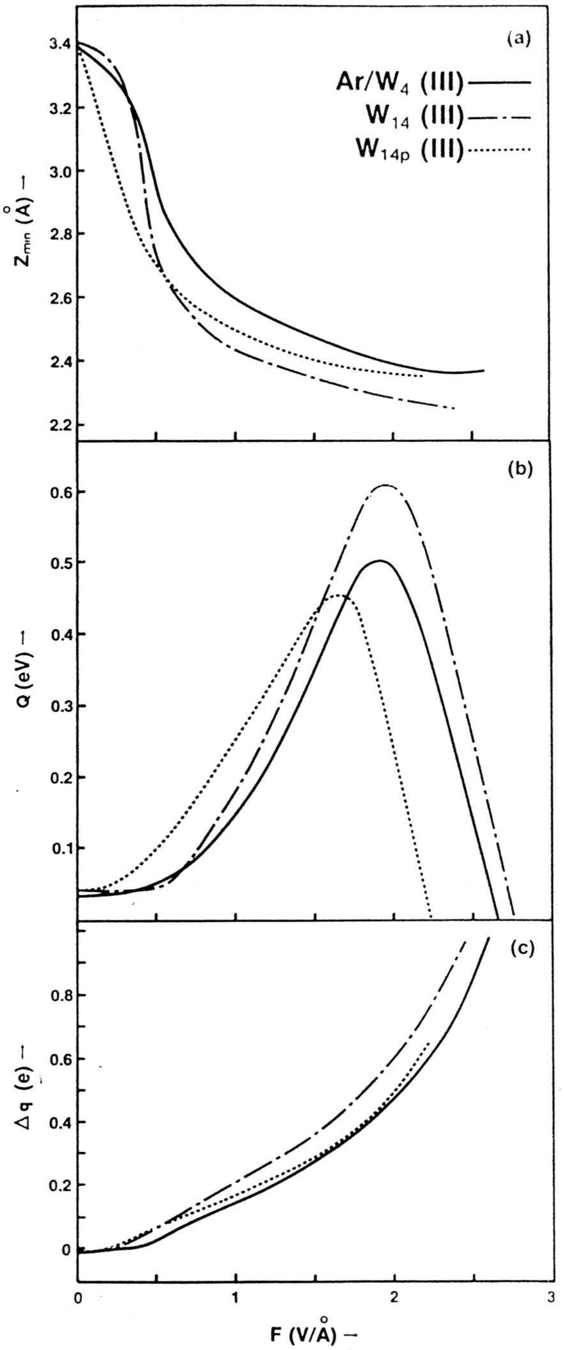

Fig.2.12: The position z_{min} of the potential minimum in Fig.2.10, the activation energy Q and the charge transfer Δq as a function of field strength for Ar interacting with various W clusters which are described in Sect.1b(i). W_{14p} is the W_{14} cluster with the zero of the field taken at -0.6 Å.

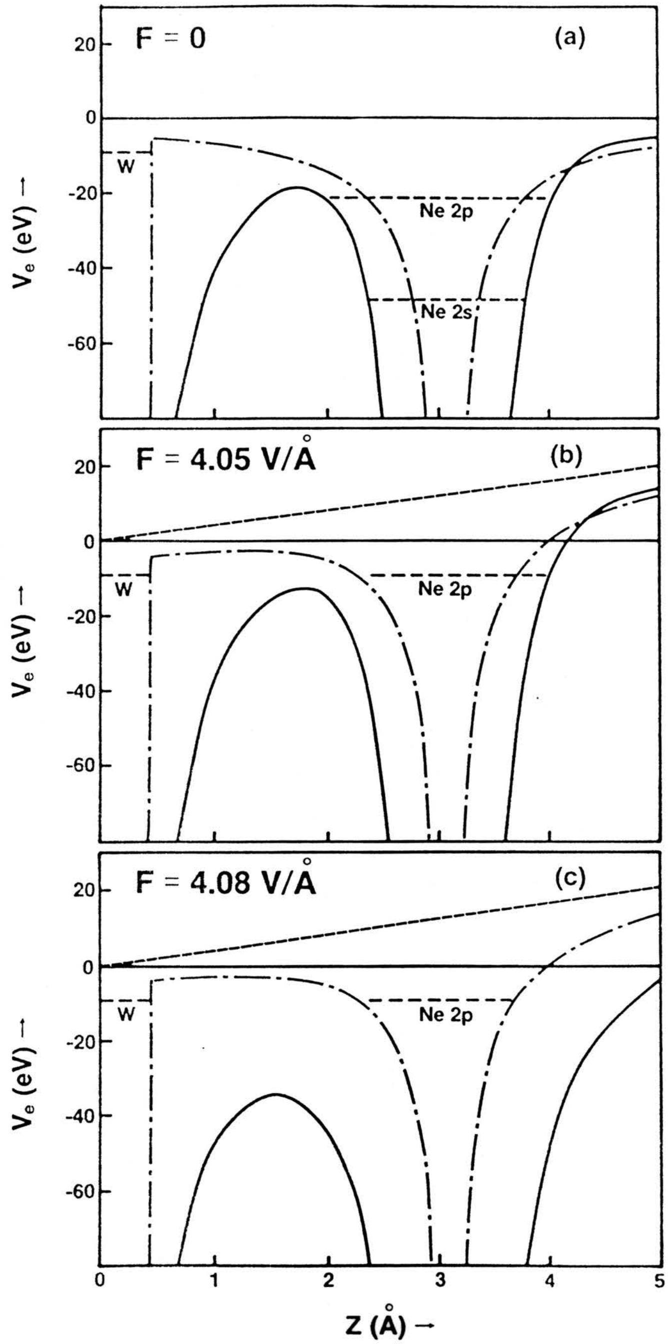

Fig.2.13: The one-electron potential (2.20) for the Ne-W_4 system at various field strengths. The dot-dashed curve is the unscreened Coulomb potential plus the field term eFz (dashed curve).

In Fig.2.13, the one-electron potential (2.20) for the Ne-W_4 system in zero field and at $F \approx 4$ V/Å is plotted. One notes that a model potential, jellium plus Coulomb, is a very poor approximation, as a simple Coulomb potential does not take into account the large size of the Ne atom. One notes again that at the critical field there is no potential barrier between the Ne p orbitals and the W d-band.

c) Summary :

In this section we have dealt with the adsorption of rare gases on a metal surface in the presence of a strong electric field as it occurs at the tip of a field ion microscope. Employing the ASED-MO method, we have been able to calculate the static properties of field-adsorption such as the field dependence of activation energies, equilibrium positions, etc. A surprising transition for He from physisorption in zero field to chemisorption in fields above 3 V/Å is explained as a consequence of its large ionization energy. One recalls that the activation energy of field-adsorbed He rises to ~ 0.6 eV with a charge transfer of 0.3 e in the field of 4.5 V/Å. This hundredfold increase in the activation energy over that in zero field is not found for Ne and Ar. Ne, indeed, field-adsorbs rather weakly, whereas Ar shows features of chemisorption again as the electric field strength rises. This taking account of the field penetration, even in an ad hoc manner, is convincing evidence that the penetration is an important effect that eventually must be included in the theory in a self-consistent way.

2. Multi-centre Coulomb Integrals :

In this section the main task is to evaluate the second term on the right hand side of eqn.(2.20), which is denoted by $V'_e(\mathbf{r})$

$$V'_e(\mathbf{r}) = e^2 \sum_{\nu} n_{\nu} \int |\Phi_{\nu}(\mathbf{r}')|^2 \frac{d\mathbf{r}'}{|\mathbf{r}-\mathbf{r}'|} \quad . \tag{2.26}$$

Here the molecular orbitals $\Phi_{\nu}(\mathbf{r}')$ are expressed in terms of Slater type orbitals (the superscript α is dropped from STO throughout in this section - compare eqn.(2.21))

$$\Phi_{\nu}(\mathbf{r}') = \sum_{\alpha i} C_{\nu}^{\alpha i} \psi_i(\mathbf{r}'-\mathbf{R}_{\alpha}) \tag{2.27}$$

where

$$\psi_i(\mathbf{r}'-\mathbf{R}_{\alpha}) = N_i \, |\mathbf{r}'-\mathbf{R}_{\alpha}|^{n_i-1} \exp(-\delta_i \, |\mathbf{r}'-\mathbf{R}_{\alpha}|) \, Y_{\ell_i m_i}(\theta,\phi) \quad , \tag{2.28}$$

N_i is the normalization constant, and n_i, ℓ_i and m_i are the principal, orbital and magnetic quantum numbers, respectively, and δ_i is the Slater exponent. Thus one can rewrite eqn.(2.26) as

$$V'_e(\mathbf{r}) = e^2 \sum_{\nu\alpha\beta ij} n_{\nu} \int C_{\nu}^{\alpha i^*} C_{\nu}^{\beta j} \psi_i(\mathbf{r}'-\mathbf{R}_{\alpha})^* \psi_j(\mathbf{r}'-\mathbf{R}_{\beta}) \frac{d\mathbf{r}'}{|\mathbf{r}-\mathbf{r}'|} \quad . \tag{2.29}$$

The above equation contains several two- and three-centre one-electron three-dimensional Coulomb integrals of the type:

$$I_{ab}(\mathbf{R}'_a, n_a, \ell_a, m_a, \delta_a; \mathbf{R}'_b, n_b, \ell_b, m_b, \delta_b; \mathbf{r}) =$$

$$= \int \psi_a(\mathbf{r}'-\mathbf{R}'_a)^* \psi_b(\mathbf{r}'-\mathbf{R}'_b) \frac{d\mathbf{r}'}{|\mathbf{r}-\mathbf{r}'|} \quad . \tag{2.30}$$

The above integral is converted analytically to a one-centre, one-dimensional integral before integration is performed numerically. The method described here is based on a prescription of Harris and Michels[31] and is general as far as the choice of the positions of the three centres and the orientations of the axial frames are concerned. The procedure involves: (i) rotation of an STO around its centre, (ii) its translation to another centre, followed by (iii) its rotation to coincide with the axes of another STO, and (iv) the rotation of the product function to the fixed spatial frame of reference, in which the integration over **r'** is performed. Here the term rotation will be interpreted as a rotation of the frame of reference about its origin, the field points (i.e. the physical system) being assumed to be fixed. The same is true for the term translation, i.e. the frame of reference is being translated.

The most general expression to expand the Coulomb potential in terms of the spherical harmonics is:

$$\frac{1}{|\mathbf{r}-\mathbf{r'}|} = \sum_{\ell=0}^{\infty} \sum_{m=-\ell}^{\ell} \frac{(\ell-|m|)!}{(\ell+|m|)!} \frac{r_-^{\ell}}{r_+^{\ell}} P_{\ell}^{m}(\cos\theta)\, P_{\ell}^{m}(\cos\theta')\, e^{im(\phi-\phi')} \qquad (2.31)$$

where **r** denotes (r,θ,ϕ), and r_+ and r_- refer to the greater and lesser, respectively, of r and r'.

However, a more elegant and less expensive (computation-wise) choice is used to evaluate the integral (2.30) by choosing **r** as the origin of the system. Thus one does not need the expansion (2.31), and the integral I_{ab} takes the form

$$I_{ab}(\mathbf{R}_a, n_a, \ell_a, m_a, \delta_a;\ \mathbf{R}_b, n_b, \ell_b, m_b, \delta_b;\ 0) =$$

$$= \int \psi_a(\mathbf{r}-\mathbf{R}_a)^{*}\ \psi_b(\mathbf{r}-\mathbf{R}_b)\ \frac{d\mathbf{r}}{r} \ . \qquad (2.32)$$

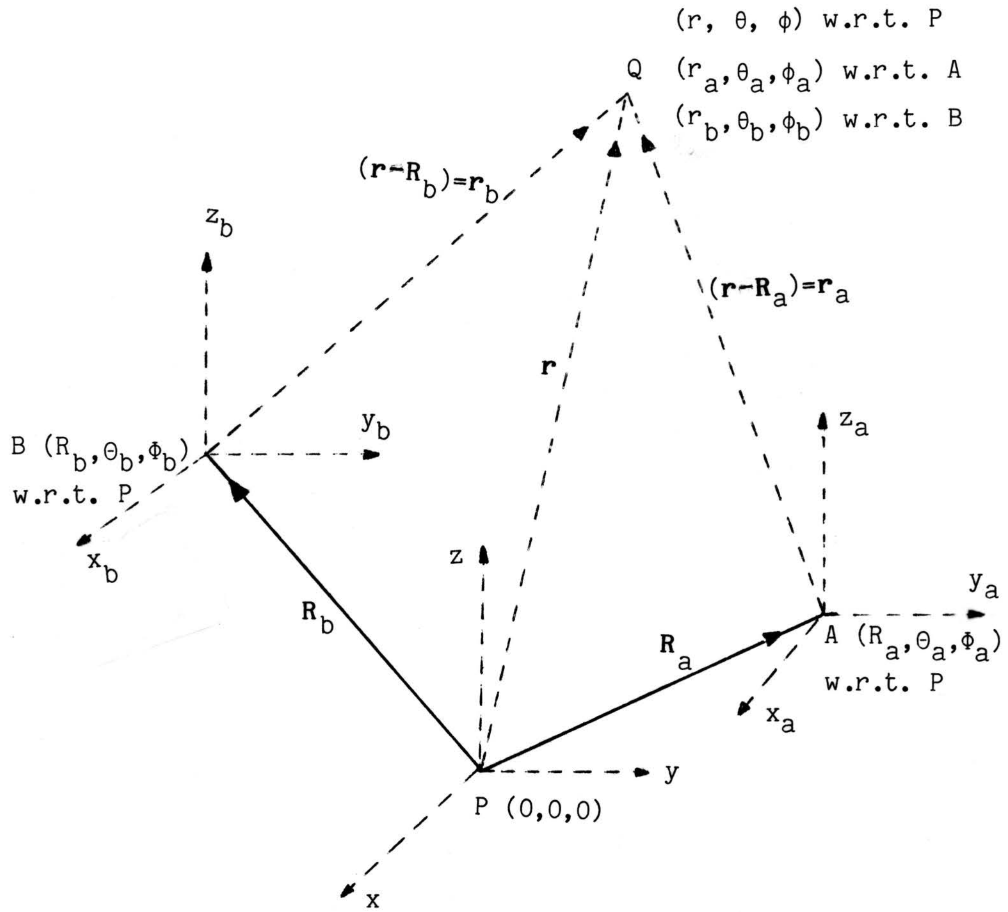

Fig.2.14: As mentioned in the text.

A schematic diagram for the coordinate systems is drawn in Fig.2.14. P is the origin, A and B are the positions of the nuclei of the two atoms, and Q is a field point. For simplicity all the x-axes are taken parallel and so are the y- and the z-axes. One takes the real form of STO ($\mathbf{r}-\mathbf{R}_a = \mathbf{r}_a$) :

$$\psi_a(\mathbf{r}_a) = N_a\, r_a^{n_a-1}\, e^{-\delta_a r_a}\, P_{\ell_a}^{m_a}(\cos\theta_a) \times \left[\begin{array}{ll} \cos(m_a\,\phi_a) & ;\ m_a \geqq 0 \\ & \\ \sin(|m_a|\,\phi_a) & ;\ m_a < 0 \end{array}\right. \tag{2.33}$$

where (r_a, θ_a, ϕ_a) are the spherical polar coordinates, centred on the nucleus of atom a. $P_\ell^m(x)$ is an associated Legendre function with the definition

$$P_\ell^m(x) = \frac{(-1)^m\ (1-x^2)^{|m|/2}}{2^\ell\ \ell!}\ \frac{d^{\ell+|m|}\ (x^2-1)^\ell}{dx^{\ell+|m|}} \tag{2.34}$$

satisfying the orthogonality relation

$$\int_{-1}^{1} P_\ell^m(x)\ P_{\ell'}^m(x)\ dx = \delta_{\ell\ell'}\ \frac{2}{2\ell+1}\ \frac{(\ell+|m|)!}{(\ell-|m|)!} \tag{2.35}$$

and the normalization constant, N (dropping the subscripts a),is given by:

$$N = \sqrt{\frac{2\ell+1}{2\pi(1+\delta_{om})}\ \frac{(\ell-|m|)!}{(\ell+|m|)!}\ \frac{(2\delta)^{2n+1}}{(2n)!}} \tag{2.36}$$

To simplify the subsequent formalism, the sine and cosine appearing in eqn.(2.33) are expressed in their complex forms (omitting the normalization constant everywhere, unless it is necessary) as

$$\psi_a(\mathbf{r}_a) = r_a^{n_a-1}\, e^{-\delta_a r_a}\, P_{\ell_a}^{m_a}(\cos\theta_a) \times \left[\begin{array}{ll} \frac{1}{2}\ (e^{im_a\phi_a} + e^{-im_a\phi_a}) & ;m_a \geqq 0 \\ & \\ \frac{i}{2}\ (e^{im_a\phi_a} - e^{-im_a\phi_a}) & ;m_a < 0 \end{array}\right. \tag{2.37}$$

There is a similar expression for $\psi_b(\mathbf{r}_b)$.

The procedure, in detail, is as follows :

(i) Rotation about A :

The form of $\psi_a(\mathbf{r}_a)$, as expressed by eqn.(2.37), is in the axial frame with the origin at A and the axes parallel to those of the fixed spatial frame of reference. One wants to express $\psi_a(\mathbf{r}_a)$ in an axial frame with origin at A and the polar axis directed towards the origin P. In this rotated frame, the coordinates of point Q are taken to be $(r_a, \theta_a', \phi_a')$, and the Euler angles (in the y-convention), responsible for the rotation, are $(\alpha_a, \beta_a, \gamma_a)$ (see Appendix A for tips on Euler angles). It is shown in Appendix A that $(\alpha_a,\ \beta_a,\ \gamma_a) = (\pi+\Phi_a,\ \pi-\Theta_a,\ 0)$, since the coordinates of the point P in the axial system, with origin at A and axes parallel to those of the fixed axial system, are $(R_a,\ \pi-\Theta_a,\ \pi+\Phi_a)$.

The effect of rotational transformations upon spherical harmonics is well known.[32] Spherical harmonics are the eigenfunctions of the orbital angular momentum operator L^2. This operator is invariant under a rotation of the frame of reference; it follows that the spherical harmonics in the rotated frame are still eigenfunctions of L^2 with the same ℓ-values. Thus the spherical harmonics transform under a rotation according to

$$Y_{\ell_a m_a}(\theta_a, \phi_a) = \sum_{\sigma=-\ell_a}^{\ell_a} D_{\ell_a}^{m_a\sigma}(\alpha_a\ \beta_a\ \gamma_a)\ Y_{\ell_a \sigma}(\theta_a', \phi_a') \qquad (2.38)$$

where

$$D_{\ell_a}^{m_a\sigma}(\alpha_a\ \beta_a\ \gamma_a) = \langle \ell_a\ m_a\ |\tilde{D}\ (\alpha_a\ \beta_a\ \gamma_a)|\ \ell_a\ \sigma\rangle \qquad (2.39)$$

with

$$\tilde{D}(\alpha_a\, \beta_a\, \gamma_a) = \exp(i\frac{\alpha_a}{\hbar}L_{z'})\, \exp(i\frac{\beta_a}{\hbar}L_{y'})\, \exp(i\frac{\gamma_a}{\hbar}L_{z'}) \quad , \qquad (2.40)$$

where x',y',z', are the rotated cartesian axes.

The properties of the operator $\tilde{D}(\alpha_a\, \beta_a\, \gamma_a)$ are determined by the algebraic properties of the operators $L_{x'}$, $L_{y'}$ and $L_{z'}$; i.e. by their commutation relations. Using eqns(2.39) and (2.40), eqn.(2.38) can be written as

$$Y_{\ell_a m_a}(\theta_a, \phi_a) = \sum_{\sigma=-\ell_a}^{\ell_a} e^{i m_a \alpha_a + i\sigma\gamma_a}\, d^{\ell_a}_{m_a\sigma}(\cos\beta_a)\, Y_{\ell_a\sigma}(\theta'_a, \phi'_a) \qquad (2.41)$$

where

$$d^{\ell_a}_{m_a\sigma}(\cos\beta_a) = \langle \ell_a\, m_a \mid \exp(i\, \frac{\beta_a}{\hbar}\, L_{y'}) \mid \ell_a\, \sigma\rangle \qquad (2.42)$$

Expressions for $d^{\ell}_{m\sigma}(t)$ are given in Appendix B. The most efficient way, however, is to generate the d-matrices for various ℓ, m and σ by recurrence methods outlined in Appendix B.

Thus, using eqns (2.37) and (2.38), one can write

$$\psi_a(\mathbf{r}_a) = r_a^{n_a-1}\, e^{-\delta_a r_a} \quad \times$$

$$\times \left[\begin{array}{ll} \frac{1}{2} \sum\limits_{\sigma=-\ell_a}^{\ell_a} \left[D_{\ell_a}^{m_a\sigma}(\alpha_a\, \beta_a\, \gamma_a) + D_{\ell_a}^{-m_a\,\sigma}(\alpha_a\, \beta_a\, \gamma_a) \right] P^{\sigma}_{\ell_a}(\cos\theta'_a)\, e^{i\sigma\phi'_a} & ; m_a \geq 0 \\ \\ \frac{i}{2} \sum\limits_{\sigma=-\ell_a}^{\ell_a} \left[D_{\ell_a}^{m_a\,\sigma}(\alpha_a\, \beta_a\, \gamma_a) - D_{\ell_a}^{-m_a\,\sigma}(\alpha_a\, \beta_a\, \gamma_a) \right] P^{\sigma}_{\ell_a}(\cos\theta'_a)\, e^{i\sigma\phi'_a} & ; m_a < 0 \end{array} \right. \qquad (2.43)$$

(ii) Translation along the z'-axis :

The next task is to expand $\psi'_a(\mathbf{r}_a)$, which is defined as

$$\psi'_a(\mathbf{r}_a) = r_a^{n_a-1} \; e^{-\delta_a r_a} \; P^{\sigma}_{\ell_a}(\cos\theta'_a) \; e^{i\sigma\phi'_a} \quad , \qquad (2.44)$$

in terms of STO's expressed in the axial system with origin at P and the polar axis along $\vec{AP}$, keeping the azimuthal angles the same in both systems. Suppose, in this system, the coordinates of the point Q changes from $(r_a, \theta'_a, \phi'_a)$ to $(r, \bar{\theta}_a, \bar{\phi}_a)$, for which the following relations hold (see Fig.2.15)

$$\left.\begin{array}{l} r_a^2 = R_a^2 + r^2 + 2\, r\, R_a \cos\bar{\theta}_a \\ r_a \sin\theta'_a = r \sin\bar{\theta}_a \\ r_a \cos\theta'_a = R_a + r \cos\bar{\theta}_a \\ \phi'_a = \bar{\phi}_a \end{array}\right] \; . \qquad (2.45)$$

The general form for the expansion of the orbital $\psi'_a(\mathbf{r}_a)$ about the point P is taken as

$$\psi'_a(\mathbf{r}_a) = \delta_a^{1-n_a} \sum_{j=|\sigma|}^{\infty} V^{\sigma}_{n_a\ell_a j}(\delta_a\, r\, R_a) \; P^{\sigma}_j(\cos\bar{\theta}_a) \; e^{i\sigma\bar{\phi}_a} \quad . \qquad (2.46)$$

$V^{\sigma}_{n_a\ell_a j}(\delta_a\, r\, R_a)$ is obtained by using the orthogonality relations of P^{σ}_j. Multiplying the right hand side of eqns (2.44) and (2.46) by $P^{\sigma}_j(\cos\bar{\theta}_a)\cdot\sin\bar{\theta}_a$ and integrating over $\bar{\theta}_a$ from 0 to π, one has

$$\int_0^{\pi} r_a^{n_a-1} \; e^{-\delta_a r_a} \; P^{\sigma}_{\ell_a}(\cos\theta'_a) \; P^{\sigma}_j(\cos\bar{\theta}_a) \; \sin\bar{\theta}_a \; d\bar{\theta}_a = \delta_a^{1-n_a} \;\; \times$$

$$\times \int_0^{\pi} \sum_{j'=|\sigma|}^{\infty} V^{\sigma}_{n_a\ell_a j'}(\delta_a\, r\, R_a) \; P^{\sigma}_{j'}(\cos\bar{\theta}_a) \; P^{\sigma}_j(\cos\bar{\theta}_a) \; \sin\bar{\theta}_a \; d\bar{\theta}_a \qquad (2.47)$$

giving

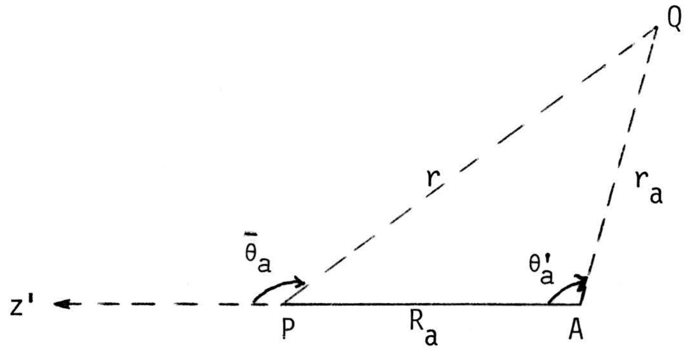

or

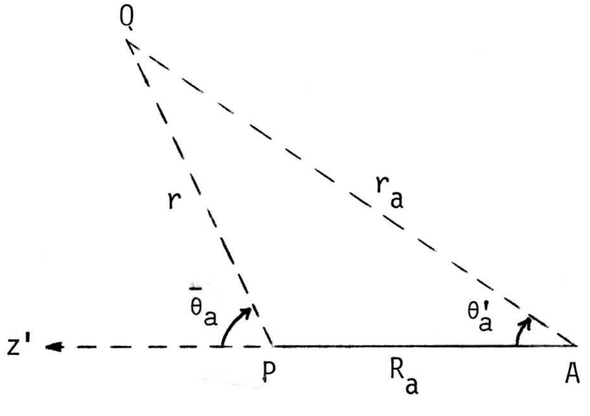

Fig.2.15: As mentioned in the text.

$$V^{\sigma}_{n_a\ell_a j}(\delta_a\, r\, R_a) = \delta_a^{n_a-1}\, \frac{2j+1}{2}\, \frac{(j-|\sigma|)!}{(j+|\sigma|)!}\ \times$$

$$\times \int_{-1}^{1} d(\cos\bar{\theta}_a)\, r_a^{n_a-1}\, e^{-\delta_a r_a}\, P^{\sigma}_{\ell_a}(\cos\theta_a')\, P^{\sigma}_{j}(\cos\bar{\theta}_a) \qquad (2.48)$$

The recurrence formulae to evaluate the V-functions are given in Appendix C.

Thus, with help of eqn.(2.46), eqn.(2.43) can be written as

$$\psi_a(\mathbf{r}_a) = \delta_a^{1-n_a} \sum_{\sigma=-\ell_a}^{\ell_a} \sum_{j=|\sigma|}^{\infty} W^{\sigma}_{ja}(r)\, P^{\sigma}_{j}(\cos\bar{\theta}_a)\, e^{i\sigma\bar{\phi}_a} \qquad (2.49)$$

where

$$W^{\sigma}_{ja}(r) = \begin{cases} \frac{1}{2}\left[D_{\ell_a}^{m_a\sigma}(\alpha_a\,\beta_a\,\gamma_a) + D_{\ell_a}^{-m_a\sigma}(\alpha_a\,\beta_a\,\gamma_a)\right] V^{\sigma}_{n_a\ell_a j}(\delta_a\, r\, R_a) & ; m_a \geq 0 \\ \\ \frac{i}{2}\left[D_{\ell_a}^{m_a\sigma}(\alpha_a\,\beta_a\,\gamma_a) - D_{\ell_a}^{-m_a\sigma}(\alpha_a\,\beta_a\,\gamma_a)\right] V^{\sigma}_{n_a\ell_a j}(\delta_a\, r\, R_a) & ; m_a < 0 \end{cases} \qquad (2.50)$$

Similarly $\psi_b(\mathbf{r}_b)$ can be expressed in the axial frame with the origin at P and the polar axis along $\vec{BP}$:

$$\psi_b(\mathbf{r}_b) = \delta_b^{1-n_b} \sum_{\lambda=-\ell_b}^{\ell_b} \sum_{k=|\lambda|}^{\infty} W^{\lambda}_{kb}(r)\, P^{\lambda}_{k}(\cos\bar{\theta}_b)\, e^{i\lambda\bar{\phi}_b} \qquad (2.51)$$

with

$$W^{\lambda}_{kb}(r) = \begin{cases} \frac{1}{2}\left[D_{\ell_b}^{m_b\lambda}(\alpha_b\,\beta_b\,\gamma_b) + D_{\ell_b}^{-m_b\lambda}(\alpha_b\,\beta_b\,\gamma_b)\right] V^{\lambda}_{n_b\ell_b k}(\delta_b\, r\, R_b) & ; m_b \geq 0 \\ \\ \frac{i}{2}\left[D_{\ell_b}^{m_b\lambda}(\alpha_b\,\beta_b\,\gamma_b) - D_{\ell_b}^{-m_b\lambda}(\alpha_b\,\beta_b\,\gamma_b)\right] V^{\lambda}_{n_b\ell_b k}(\delta_b\, r\, R_b) & ; m_b < 0 \end{cases} \qquad (2.52)$$

where $(\alpha_b, \beta_b, \gamma_b) = (\pi+\Phi_b, \pi-\Theta_b, 0)$, analogous to $(\alpha_a, \beta_a, \gamma_a)$ as shown in Appendix A.

(iii) Rotation again :

Until now, $\psi_a(\mathbf{r}_a)$ and $\psi_b(\mathbf{r}_b)$ have been expressed in the axial frames with common origins but different orientations. The next task is to re-express $\psi_a(\mathbf{r}_a)$ in the axial frame in which $\psi_b(\mathbf{r}_b)$ is currently expressed, i.e. the axial frame with the origin at P and the polar axis along $\vec{BP}$. In this frame, point Q (see Fig.2.14) has the coordinates $(r, \bar{\theta}_b, \bar{\phi}_b)$. Assume the Euler angles necessary to rotate the axes from the direction $(\pi+\Phi_a, \pi-\Theta_a, 0)$ to $(\pi+\Phi_b, \pi-\Theta_b, 0)$ are $(\alpha_{ab}, \beta_{ab}, \gamma_{ab})$. A convenient method to evaluate $(\alpha_{ab}, \beta_{ab}, \gamma_{ab})$ is given in Appendix A, together with the special meaning of the direction used here. Thus one can write

$$\psi_a(\mathbf{r}_a) = \delta_a^{1-n_a} \sum_{j=0}^{\infty} \sum_{\sigma=-j}^{j} W^{\sigma}_{ja,b}(r)\, P_j^{\sigma}(\cos\bar{\theta}_b)\, e^{i\sigma\bar{\phi}_b} \tag{2.53}$$

with

$$W^{\sigma}_{ja,b}(r) = \sum_{\tau=-j}^{j} D_j^{\tau\sigma}(\alpha_{ab}\ \beta_{ab}\ \gamma_{ab})\, W_{ja}^{\tau}(r) \tag{2.54}$$

From eqn.(2.50) one finds that

$$W_{ja}^{\sigma}(r)^{*} = W_{ja}^{-\sigma}(r) \tag{2.55}$$

since (using eqns (2.34) and (2.48))

$$V^{\sigma}_{n_a\ell_a j}(\delta_a\ r\ R_a) = V^{-\sigma}_{n_a\ell_a j}(\delta_a\ r\ R_a) \quad . \tag{2.56}$$

With the help of a Clebsch-Gordan expansion, the product of two associated Legendre polynomials can be expressed in terms of one :

$$P_j^{\sigma}(x)\ P_k^{\lambda}(x) = \sum_{\mu=|j-k|}^{|j+k|} C_{\mu jk}^{\ \sigma\lambda}\ P_{\mu}^{\sigma-\lambda}(x) \tag{2.57}$$

And thus one can write

$$\psi_a(\mathbf{r}_a)^* \; \psi_b(\mathbf{r}_b) = \delta_a^{1-n_a} \, \delta_b^{1-n_b} \sum_{j=0}^{\infty} \; \sum_{\sigma=-j}^{j} \; \sum_{\lambda=-\ell_b}^{\ell_b} \; \sum_{k=|\lambda|}^{\infty} \quad \times$$

$$\times \quad e^{i(\lambda-\sigma)\bar{\phi}_b} \, W_{ja,b}^{-\sigma}(r) \, W_{kb}^{\lambda}(r) \sum_{\mu} C_{\mu jk}^{\sigma\lambda} \, P_{\mu}^{\lambda-\sigma}(\cos\bar{\theta}_b) \qquad (2.58)$$

or, in a simpler notation,

$$\psi_a(\mathbf{r}_a)^* \; \psi_b(\mathbf{r}_b) = \sum_{\mu\nu} f_{\mu b}^{\nu}(r) \, P_{\mu}^{\nu}(\cos\bar{\theta}_b) \, e^{i\nu\bar{\phi}_b} \qquad (2.59)$$

where

$$f_{\mu b}^{\nu}(r) = \delta_a^{1-n_a} \, \delta_b^{1-n_b} \sum_{j=0}^{\infty} \sum_{k} \sum_{\sigma} C_{\mu jk}^{\sigma,\nu+\sigma} \, W_{ja,b}^{-\sigma}(r) \, W_{kb}^{\nu+\sigma}(r). \qquad (2.60)$$

The Clebsch-Gordan coefficients with their recurrence relations are given in Appendix D. The summations over μ in eqn.(2.58), and over k and σ in eqn.(2.60), include all values for which the coefficients $C_{\mu jk}^{\sigma\lambda}$ do not vanish.

(iv) Expressing the Product Function in the Spatial Frame of Reference :

Finally, one wants to express the product (2.59) in the axial frame in which the integration over $\mathbf{r}$ is performed in eqn.(2.32). This is the frame in which the coordinates of the point Q are (r, θ, ϕ). Euler angles to rotate the axial frame from the direction $(\pi+\Phi_b, \pi-\Theta_b, 0)$ to the direction $(0, 0, 0)$ are $(\pi+\Phi_b, \pi-\Theta_b, 0)^{-1} = (\pi, \pi-\Theta_b, -\Phi_b)$. Thus one can write eqn.(2.59) as

$$\psi_a(\mathbf{r}_a)^* \; \psi_b(\mathbf{r}_b) = \sum_{\mu\nu} f_\mu^\nu(r) \; P_\mu^\nu(\cos\theta) \; e^{i\nu\phi} \tag{2.61}$$

where

$$f_\mu^\nu(r) = \sum_{\eta=-\mu}^{\mu} D_\mu^{\eta\nu}(\pi, \; \pi-\Theta_b, \; -\Phi_b) \; f_{\mu b}^{\;\eta}(r) \tag{2.62}$$

(v) Conversion to the one-variable integral :

Using eqn.(2.61) one can write eqn.(2.32) as

$I_{ab}(\mathbf{R}_a, n_a, \ell_a, m_a, \delta_a; \; \mathbf{R}_b, n_b, \ell_b, m_b, \delta_b; \; 0) \; = \; I_{ab} \; =$

$$= \sum_{\mu\nu} \int_{r=0}^{\infty} \int_{\theta=0}^{\pi} \int_{\phi=0}^{2\pi} \frac{r^2 dr \;\, d\theta \;\, d\phi \;\, \sin\theta}{r} \; f_\mu^\nu(r) \; P_\mu^\nu(\cos\theta) \; e^{i\nu\phi} \tag{2.63}$$

or,

$$I_{ab} = \sum_{\mu\nu} 2\pi\delta_{o\nu} \int_0^\infty r dr \; f_\mu^\nu(r) \int_0^\pi \sin\theta d\theta \; P_\mu^\nu(\cos\theta) \tag{2.64}$$

or,

$$I_{ab} = 2\pi \sum_\mu \int_0^\infty r dr \; f_\mu^o(r) dr \; 2 i^\mu \; \delta_{\mu o} \tag{2.65}$$

or,

$$I_{ab} = 4\pi \int_0^\infty r \; f_o^o(r) \; dr \tag{2.66}$$

In going from eqn.(2.64) to eqn.(2.65) one has used[33]

$$\int_{-1}^{1} P_\mu^o(x) \; dx = \int_{-1}^{1} P_\mu(x) \; dx = 2 \; i^\mu \; j_\mu(0) = 2 \; i^\mu \; \delta_{\mu o} \; j_o(0) = 2 \; i^\mu \; \delta_{\mu o} \tag{2.67}$$

Using eqn.(2.62), eqn.(2.66) can be written as

$$I_{ab} = 4\pi \int_0^\infty r\, f_{ob}^{o}(r)dr \tag{2.68}$$

since,

$$D_{o}^{oo}(\pi,\ \pi-\Theta_b,\ -\Phi_b) = 1 \quad . \tag{2.69}$$

Using eqn (2.60) and putting back the normalization contants, eqn.(2.68) can be written as

$$I_{ab} = 4\pi N_a N_b \int_0^\infty r\,dr\ \delta_a^{1-n_a}\ \delta_b^{1-n_b} \sum_{j=0}^{\infty} \sum_{k} \sum_{\sigma} C_{ojk}^{\sigma\sigma}\ W_{ja,b}^{-\sigma}(r)\ W_{kb}^{\sigma}(r)\ . \tag{2.70}$$

Since, C is zero if $|j-k| \leqq 0$ is not satisfied, one can replace $C_{ojk}^{\sigma\sigma}$ by $C_{ojj}^{\sigma\sigma}\ \delta_{jk}$ and write eqn.(2.70) as

$$I_{ab} = 4\pi N_a N_b \delta_a^{1-n_a}\ \delta_b^{1-n_b} \int_0^\infty r\,dr \sum_{j=0}^{\infty} \sum_{\sigma} C_{ojj}^{\sigma\sigma}\ W_{ja,b}^{-\sigma}(r)\ W_{jb}^{\sigma}(r) \tag{2.71}$$

(vi) Back from imaginary to the real form :

One should remember that the wave functions are real to start with and the conversion to the complex form was employed to simplify the mathematical analysis. At this stage, one can revert to the real form again for the convenience of the computations.

With the help of eqn.(2.54), one can rewrite eqn.(2.71) as

$$I_{ab} = 4\pi N_a N_b \delta_a^{1-n_a}\ \delta_b^{1-n_b} \int_0^\infty r\,dr \sum_{j=0}^{\infty} [Z] \tag{2.72}$$

where

$$[Z] = \sum_{\sigma=-\ell_b}^{\ell_b} \sum_{\tau=-\ell_a}^{\ell_a} C_{ojj}^{\sigma\sigma} \, W_{jb}^{\sigma}(r) \, D_j^{\tau,-\sigma}(\alpha_{ab} \, \beta_{ab} \, \gamma_{ab}) \, W_{ja}^{\tau}(r) \qquad (2.73)$$

Using eqns (2.39), (2.40), (2.42) and (2.52), the above equation can be written as

$$\begin{aligned} [Z] = \sum_{\sigma=-\ell_b}^{\ell_b} \sum_{\tau=-\ell_a}^{\ell_a} C_{ojj}^{\sigma\sigma} \, & \frac{1(i)}{2}\left[D_{\ell_b}^{m_b\sigma}(\alpha_b \, \beta_b \, \gamma_b) \pm D_{\ell_b}^{-m_b\sigma}(\alpha_b \, \beta_b \, \gamma_b)\right] \times \\ & \times V_{n_b\ell_b j}^{\sigma}(\delta_b \, r \, R_b) \; e^{-i\sigma\gamma_{ab}} \; d_{\tau,-\sigma}^{j}(\cos\beta_{ab}) \; e^{i\tau\alpha_{ab}} \times \\ & \times \frac{1(i)}{2}\left[D_{\ell_a}^{m_a\tau}(\alpha_a \, \beta_a \, \gamma_a) \pm D_{\ell_a}^{-m_a\tau}(\alpha_a \, \beta_a \, \gamma_a)\right] V_{n_a\ell_a j}^{\tau}(\delta_a \, r \, R_a) \qquad (2.74) \end{aligned}$$

In the above equation, the factor of $\frac{1}{2}$ before, and the +ve sign in the middle of the square brackets are for the positive or zero m-values. These are replaced by $\frac{i}{2}$ and the -ve sign, respectively, for the negative m-values. Replacing $\cos\beta_{ab}$ by t_{ab}, etc., and using eqns (2.39), (2.40) and (2.42) again, the above equation is replaced by

$$\begin{aligned} [Z] = \sum_{\sigma=-\ell_b}^{\ell_b} \sum_{\tau=-\ell_a}^{\ell_a} C_{ojj}^{\sigma\sigma} \, & V_{n_b\ell_b j}^{\sigma}(\delta_b \, r \, R_b) \, V_{n_a\ell_a j}^{\tau}(\delta_a \, r \, R_a) \, d_{\tau,-\sigma}^{j}(t_{ab}) \times \\ & \times \frac{1(i)}{2}\left[e^{i(m_b\alpha_b+\sigma(\gamma_b-\gamma_{ab}))} \, d_{m_b\sigma}^{\ell_b}(t_b) \pm e^{i(-m_b\alpha_b+\sigma(\gamma_b-\gamma_{ab}))} \, d_{-m_b\sigma}^{\ell_b}(t_b)\right] \times \\ & \times \frac{1(i)}{2}\left[e^{i(m_a\alpha_a+\tau(\gamma_a+\gamma_{ab}))} \, d_{m_a\tau}^{\ell_a}(t_a) \pm e^{i(-m_a\alpha_a+\tau(\gamma_a+\gamma_{ab}))} \, d_{-m_a\tau}^{\ell_a}(t_a)\right]. \end{aligned}$$

$$- - - (2.75)$$

Using the equalities $d_{\tau\sigma}^{j}(t) = d_{-\tau,-\sigma}^{j}(t)$, $V_{n\ell j}^{m}(\delta \, r \, R) = V_{n\ell j}^{-m}(\delta \, r \, R)$ and $C_{ojj}^{\sigma\sigma} = C_{ojj}^{-\sigma,-\sigma}$ (see Appendices B, C and D, respectively), the above equation can be written as

$$[Z] = \sum_{\sigma=0}^{\ell_b} \sum_{\tau=0}^{\ell_a} C_{0jj}^{\sigma\sigma} \, V^{\sigma}_{n_b\ell_b j}(\delta_b \; r \; R_b) \, V^{\tau}_{n_a\ell_a j}(\delta_a \; r \; R_a) \times$$

$$\times \; (1-\frac{\delta_{0\sigma}}{2})(1-\frac{\delta_{0\tau}}{2}) \; ([X]+[Y]) \qquad (2.76)$$

Here [X] is given by

$$\begin{aligned}
[X] = {} & d^{j}_{\tau,-\sigma}(t_{ab}) \times \\
& \times \Bigg[\frac{1(i)}{2}\Big[e^{i(m_b\alpha_b+\sigma(\gamma_b-\gamma_{ab}))} d^{\ell_b}_{m_b\sigma}(t_b) \pm e^{i(-m_b\alpha_b+\sigma(\gamma_b-\gamma_{ab}))} d^{\ell_b}_{-m_b\sigma}(t_b) \Big] \times \\
& \times \frac{1(i)}{2}\Big[e^{i(m_a\alpha_a+\tau(\gamma_a+\gamma_{ab}))} d^{\ell_a}_{m_a\tau}(t_a) \pm e^{i(-m_a\alpha_a+\tau(\gamma_a+\gamma_{ab}))} d^{\ell_a}_{-m_a\tau}(t_a) \Big] + \\
& + \frac{1(i)}{2}\Big[e^{i(m_b\alpha_b-\sigma(\gamma_b-\gamma_{ab}))} d^{\ell_b}_{m_b-\sigma}(t_b) \pm e^{i(-m_b\alpha_b-\sigma(\gamma_b-\gamma_{ab}))} d^{\ell_b}_{-m_b-\sigma}(t_b) \Big] \times \\
& \times \frac{1(i)}{2}\Big[e^{i(m_a\alpha_a-\tau(\gamma_a+\gamma_{ab}))} d^{\ell_a}_{m_a-\tau}(t_a) \pm e^{i(-m_a\alpha_a-\tau(\gamma_a+\gamma_{ab}))} d^{\ell_a}_{-m_a-\tau}(t_a) \Big] \Bigg]
\end{aligned}$$

$$- - - \; (2.77)$$

Expanding the right hand side of the above equation and combining the proper pair of the exponential terms, [X] can be written as a purely real function of sines and cosines :

$$\begin{aligned}
[X] = {} & \frac{1}{2} \, d^{j}_{\tau,-\sigma}(t_{ab}) \times \\
& \times \Big[d^{\ell_b}_{m_b\sigma}(t_b) \, d^{\ell_a}_{m_a\tau}(t_a) \; \mathrm{fun}_1(m_b\alpha_b+\sigma(\gamma_b-\gamma_{ab})+m_a\alpha_a+\tau(\gamma_a+\alpha_{ab})) + \\
& + d^{\ell_b}_{-m_b\sigma}(t_b) \, d^{\ell_a}_{-m_a\tau}(t_a) \; \mathrm{fun}_2(-m_b\alpha_b+\sigma(\gamma_b-\gamma_{ab})-m_a\alpha_a+\tau(\gamma_a+\alpha_{ab})) + \\
& + d^{\ell_b}_{m_b\sigma}(t_b) \, d^{\ell_a}_{-m_a\tau}(t_a) \; \mathrm{fun}_3(m_b\alpha_b+\sigma(\gamma_b-\gamma_{ab})-m_a\alpha_a+\tau(\gamma_a+\alpha_{ab})) + \\
& + d^{\ell_b}_{-m_b\sigma}(t_b) \, d^{\ell_a}_{m_a\tau}(t_a) \; \mathrm{fun}_4(-m_b\alpha_b+\sigma(\gamma_b-\gamma_{ab})+m_a\alpha_a+\tau(\gamma_a+\alpha_{ab})) \Big]
\end{aligned}$$

$$- - - \; (2.78)$$

where the functions, fun, are defined as :

$$\left.\begin{array}{lll}
\mathrm{fun}_1(\zeta) = & \cos(\zeta) & ;\ m_a \geqq 0 \text{ and } m_b \geqq 0 \\
 & -\cos(\zeta) & ;\ m_a < 0 \text{ and } m_b < 0 \\
 & \sin(\zeta) & ;\ m_a \geqq 0 \text{ and } m_b < 0 \\
 & \sin(\zeta) & ;\ m_a < 0 \text{ and } m_b \geqq 0, \\
\mathrm{fun}_2(\zeta) = & \cos(\zeta) & ;\ m_a \geqq 0 \text{ and } m_b \geqq 0 \\
 & -\cos(\zeta) & ;\ m_a < 0 \text{ and } m_b < 0 \\
 & -\sin(\zeta) & ;\ m_a \geqq 0 \text{ and } m_b < 0 \\
 & -\sin(\zeta) & ;\ m_a < 0 \text{ and } m_b \geqq 0, \\
\mathrm{fun}_3(\zeta) = & \cos(\zeta) & ;\ m_a \geqq 0 \text{ and } m_b \geqq 0 \\
 & \cos(\zeta) & ;\ m_a < 0 \text{ and } m_b < 0 \\
 & \sin(\zeta) & ;\ m_a \geqq 0 \text{ and } m_b < 0 \\
 & -\sin(\zeta) & ;\ m_a < 0 \text{ and } m_b \geqq 0, \\
\text{and} & & \\
\mathrm{fun}_4(\zeta) = & \cos(\zeta) & ;\ m_a \geqq 0 \text{ and } m_b \geqq 0 \\
 & \cos(\zeta) & ;\ m_a < 0 \text{ and } m_b < 0 \\
 & -\sin(\zeta) & ;\ m_a \geqq 0 \text{ and } m_b < 0 \\
 & \sin(\zeta) & ;\ m_a < 0 \text{ and } m_b \geqq 0
\end{array}\right] . \qquad (2.79)$$

Similarly [Y], as appearing in eqn.(2.76), is given by

$$\begin{aligned}
[Y] = {} & \frac{1}{2}\, d^{j}_{\tau\sigma}(t_{ab}) \quad x \\
& x \Big[d^{\ell_b}_{m_b\sigma}(t_b)\, d^{\ell_a}_{m_a,-\tau}(t_a)\, \mathrm{fun}_1(m_b\alpha_b+\sigma(\gamma_b-\gamma_{ab})+m_a\alpha_a-\tau(\gamma_a+\alpha_{ab})) + \\
& + d^{\ell_b}_{-m_b\sigma}(t_b)\, d^{\ell_a}_{-m_a,-\tau}(t_a)\, \mathrm{fun}_2(-m_b\alpha_b+\sigma(\gamma_b-\gamma_{ab})-m_a\alpha_a-\tau(\gamma_a+\alpha_{ab})) + \\
& + d^{\ell_b}_{m_b\sigma}(t_b)\, d^{\ell_a}_{-m_a,-\tau}(t_a)\, \mathrm{fun}_3(m_b\alpha_b+\sigma(\gamma_b-\gamma_{ab})-m_a\alpha_a-\tau(\gamma_a+\alpha_{ab})) + \\
& + d^{\ell_b}_{-m_b\sigma}(t_b)\, d^{\ell_a}_{m_a,-\tau}(t_a)\, \mathrm{fun}_4(-m_b\alpha_b+\sigma(\gamma_b-\gamma_{ab})+m_a\alpha_a-\tau(\gamma_a+\alpha_{ab})) \Big]
\end{aligned}$$

$$- - - \quad (2.80)$$

Finally, using eqns (2.72) and (2.76) one can write

$$I_{ab} = 4\pi N_a N_b \delta_a^{1-n_a}\,\delta_b^{1-n_b} \int_0^\infty r\,dr \sum_{\sigma=o}^{\ell_b} \sum_{\tau=o}^{\ell_a} \sum_{j=o}^{\infty} (1-\frac{\delta_{o\sigma}}{2})(1-\frac{\delta_{o\tau}}{2}) \times$$

$$\times\ ([X]+[Y])\ C_{ojj}^{\sigma\sigma}\ V^{\sigma}_{n_b\ell_b j}(\delta_b\ r\ R_b)\ V^{\tau}_{n_a\ell_a j}(\delta_a\ r\ R_a) \qquad (2.81)$$

In this equation, the integration is performed numerically using Lobatto quadrature,[35] of order 64. This technique requires conversion of the limits of integration to the interval (-1,1). Making the change of variable $r = \frac{1+x}{1-x}$, eqn.(2.81) converts to

$$I_{ab} = 4\pi N_a N_b \delta_a^{1-n_a}\,\delta_b^{1-n_b} \int_{-1}^{1} \frac{2(1+y)}{(1-y)^3}dy \sum_{\sigma=o}^{\ell_b} \sum_{\tau=o}^{\ell_a} \sum_{\max(\sigma,\tau)}^{\infty} (1-\frac{\delta_{o\sigma}}{2})(1-\frac{\delta_{o\tau}}{2}) \times$$

$$\times\ ([X]+[Y])\ C_{ojj}^{\sigma\sigma}\ V^{\sigma}_{n_b\ell_b j}(\delta_b\ \frac{1+y}{1-y}\ R_b)\ V^{\tau}_{n_a\ell_a j}(\delta_a\ \frac{1+y}{1-y}\ R_a)\ , \qquad (2.82)$$

which can be written approximately as

$$I_{ab} = 8\pi N_a N_b \delta_a^{1-n_a}\,\delta_b^{1-n_b} \sum_{k=2}^{63} H_k \frac{1+y_k}{(1-y_k)^3} \sum_{\sigma=o}^{\ell_b} \sum_{\tau=o}^{\ell_a} \sum_{\max(\sigma,\tau)}^{\infty} (1-\frac{\delta_{o\sigma}}{2})(1-\frac{\delta_{o\tau}}{2}) \times$$

$$\times\ ([X]+[Y])\ C_{ojj}^{\sigma\sigma}\ V^{\sigma}_{n_b\ell_b j}(\delta_b\ \frac{1+y_k}{1-y_k}\ R_b)\ V^{\tau}_{n_a\ell_a j}(\delta_a\ \frac{1+y_k}{1-y_k}\ R_a) \qquad (2.83)$$

The abscissae y_k and the corresponding weights H_k of the Lobatto quadrature of order 64 are given in Appendix E. Since the integrand in eqn.(2.82) vanishes at both limits, the summation in eqn.(2.83) is performed only from k=2 to k=63.

To calculate $V_e'(\mathbf{r})$ in eqn.(2.29), about 2000 multi-centre Coulomb integrals of type (2.83) are required. Computational details concerning the saving of computer memory and time are given in Appendix F.

3. Effects of Field Penetration, Friedel Oscillations and Atomic Polarization on Adsorption of He onto W :

In Sect.1, the electric field has been assumed to be given by a step function, i.e. constant outside the metal and zero inside, and the penetration of this field has been included in an ad hoc manner. In this section, this model is improved in a number of ways, most importantly by including the field penetration (taking the Friedel oscillations into account) and the atomic polarization effects (which were not included previously, in order to keep the analysis simple). These modifications of the theory do not lead to qualitatively new results for the field adsorption of rare gases. However, they are absolutely essential to describe field evaporation of metal atoms (see Chap. IV). Obviously, if neither polarization of the top-most metal atom nor the penetration of the electric field into the metal are considered, no field evaporation can occur.

Inclusion of atomic polarization effects is straightforward within the framework of the ASED-MO model (see Sect.1a(ii)). In dealing with field penetration effects, the present work is guided by recent jellium model results[27,28] in strong electric fields, that have shown that the effective metal surface shifts inward with increasing electric fields by as much as half an angstrom, and that the region over which the electric field drops to zero, i.e., the region of the induced surface charge density, is about an angstrom wide (FWHM) and narrows with increasing field.

a) Field Penetration

A proper theory of field adsorption must include a self-consistent determination of the externally applied electric field in the vicinity of the adsorbing particle. This has not been done so far. What are available are model calculations, using functional density methods within the jellium model of a metal, of the excess charge induced by a sheet of charges located a large distance away from the metal surface.[27,28] Schmickler and Henderson[27] minimize the Hohenberg-Kohn-Sham energy functional[36] with respect to a family of density trial functions

$$n(z) = n_+ \times \left[\begin{array}{ll} 1 - A\,e^{\alpha z}\cos(\gamma z+\delta) & ;\ z < 0 \\ & \\ B\,e^{-\beta z} & ;\ z > 0\ . \end{array} \right. \qquad (2.84)$$

Here z is taken to be zero for the jellium edge. Their main conclusion is that the centre of mass, z_0, of the induced charge density (i.e., the effective image plane of the charge situated outside the jellium) lies one-half to one angstrom outside the jellium edge, and it (z_0) moves inward with increasing surface charge, i.e., the applied electric field. Recall that the jellium edge is typically put half an interplanar distance outside the top-most lattice plane.

Gies and Gerhardts[28] produced self-consistent calculations of the electron distribution at a (flat) jellium surface in a strong static electric field. They found that the centre of mass, z_0, of the induced charge density shifts, again, towards the jellium with increasing fields, eventually penetrating at the unrealistically high electric field of 10.8 V/Å, some 0.35 Å into the jellium (for a metal with a Wigner-Seitz radius r_s=3). r_s is defined as the radius, in units of the Bohr length

(a_0=0.529Å), of a sphere whose volume is equal to the volume per conduction electron. Field emission of ions is expected to precede such dramatic field penetration. They also found that the width, Ω, of the induced charge density decreases slightly with increasing field, from some 1.9Å, in zero or weak fields, to 1.7Å for large fields. Ω and z_0 have been reported in Table 2.3 for various values of electric fields. Ω, z_0 and λ (the wave length of the Friedel oscillations) for a weak inducing fields are given in Table 2.4 for various r_s values.

It should be stressed once more that these model calculations are for a flat, structureless metal (jellium) surface. The major additional complication in the case of field adsorption and field evaporation arises from the fact that electric fields are greatly enhanced at the adsorption sites, namely at kink sites, at terraces, and around small atom clusters on top of extended planes. Such inhomogeneities are extremely difficult to calculate reliably. All one can do at present is to incorporate some of the insight gained in the above jellium calculations, together with the calculations of Lang and Kohn,[37] into the cluster calculations of Sect.1. The findings below will highlight the necessity to perform a self-consistent calculation.

In an attempt to incorporate field penetration effects in the present cluster calculations, a number of simplifying assumptions are made. First of all, it is assumed that the electric field has only a z-component that, in addition, only depends on z. Employing a parametrization of the excess charge density, similar to eqn.(2.84) with Friedel oscillations on the metal side and an approximate exponential decay on the vacuum side, one can use Poisson's equation (one-dimensional) to calculate the electric field in the surface region (see

Table 2.3: The width (FWHM), Ω, and the centre of mass, z_0, of the induced surface charge density for various external static electric fields, F_0, for $r_s = 3$ as obtained from Ref.28. z_0 is measured from the jellium edge, which itself is separated from the first lattice plane by half an interplanar spacing. Positive z-direction is towards the vacuum.

F_0(V/Å)	z_0(Å)	Ω(Å)
0(limit)[a]	0.75	1.90
1.0	0.50	1.80
2.0	0.35	1.74
3.0	0.23	1.70
4.0	0.15	1.66
5.0	0.05	1.64
6.0	-0.03	1.64
7.0	-0.11	1.63
7.5	-0.15	1.63

a. The weak field results are similar to those of Lang and Kohn.[37]

Table 2.4: Ω, z_0 and λ for a weak inducing field for different r_s values as taken from Ref.37. See Table 2.3 for the details. λ is the wavelength of the Friedel oscillations.

r_s(a.u.)	z_0(Å)	Ω(Å)	λ(Å)
2	0.85	1.64	1.73
4	0.69	2.20	3.46
6	0.63	2.65	5.20

Appendix G). The field again features oscillations, decaying into the metal, and an exponential rise to the asymptotic constant value, F_0, in vacuo. Examples of electric fields, F, and associated field potentials, V_F (see eqn.(2.12)), are depicted in Fig.2.16 for the Wigner-Seitz radius $r_s = 3$ and $F_0 = 1$, 3 and 5 V/Å. It is important to note that, although the electric field has reached its maximum value, F_0, some 2 Å above the surface where adsorption typically takes place, the associated energy is only a fraction of its value had the field been approximated as being constant all the way to the position of the top metal atom, as done in Sect.1. On the other hand, taking the field constant up to the image plane at z_0, identified as the centre of mass of the field-induced surface charge (also known as the position of the effective metal surface), yields a very good approximation to the field energy a few angstroms above the surface.

b) Atomic Polarization Effects

To improve the previous account of the electric field effects (in addition to its penetration), within the framework of the cluster calculations, one should also consider the $\alpha = \beta$ terms in eqn.(2.15),

$$\int \psi_i^{\alpha}(\mathbf{r})^* \, [\, V_F(z) - V_F(z_\alpha) \,] \, \psi_j^{\alpha}(\mathbf{r}) \, d^3\mathbf{r} \quad , \qquad (2.85)$$

which account for the atomic polarization. Expressions for $V_F(z)$ are given in Appendix G for both $z < z_0$ and $z > z_0$. To evaluate the matrix elements (2.85) analytically, it is convenient to express $V_F(z)$ as a power series in z.

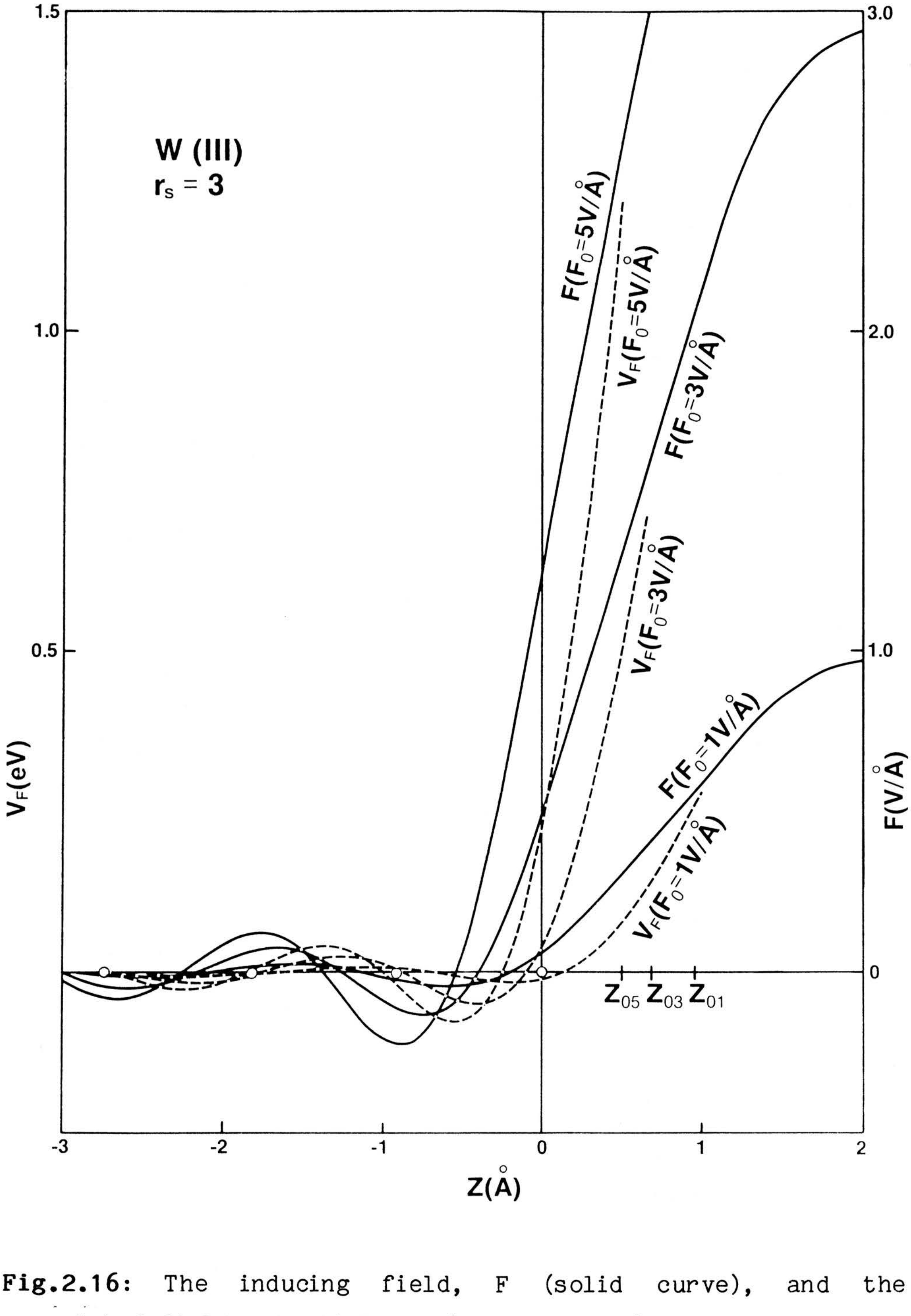

Fig.2.16: The inducing field, F (solid curve), and the associated field potential, V_F (dashed curve), as obtained from the prescription of Appendix G. Small circles denote the positions of the lattice planes parallel to the W(111) surface. z_{01}, z_{03} and z_{05} are the centres of the induced surface charge density for F_0 = 1, 3 and 5 V/Å, respectively.

For the surface W atoms (see Fig.2.16) $V_F(z)$ is approximated as

$$V_F(z) = E_0 + E_2 (z-z_m)^2 \tag{2.86}$$

where z_m is the position of the first minimum (on the left of z_0), in the V_F curve. E_0 is the energy at z_m and E_2 is determined from the best fit. E_0, z_m, and E_2 are given in Table 2.5 for different field strengths, F_0. For the adsorbed He atom (~ 2 Å away from the surface W atoms), one should note that over the extent of its orbitals, the electric field, F, varies little. Therefore, one can employ a Taylor expansion to get

$$V_F(z) - V_F(z_\alpha) = (z-z_\alpha)\; e\; F(z_\alpha) + \frac{1}{2!} (z-z_\alpha)^2\; e\; F'(z_\alpha) + \cdot\cdot \tag{2.87}$$

ASED-MO theory takes $\psi_i^{\alpha}(\mathbf{r})$ in (2.85) to be Slater type orbitals. The matrix elements of z, z^2, etc., between different orbitals on the same atom, are given in Appendix H. To check the appropriateness of these wavefunctions and the corresponding matrix elements for the present situation, the polarizability of free atoms is calculated. To demonstrate the method and to make connection with the phenomenological approaches, a two-level atom, for example, helium with only 1s and 2p levels included, is considered. The Hamiltonian matrix then reads

$$\begin{bmatrix} H_{11} & H_{21} \\ H_{12} & H_{22} \end{bmatrix} \tag{2.88}$$

with

Table 2.5: E_0, E_2 and z_m, as appearing in eqn.(2.86), for the W(111) surface. z_0 is the centre of mass of the induced charge density and z_1 is as obtained from eqn.(2.99). z=0 has been taken for the surface W atoms.

			$r_s = 3$			$r_s = 1.5$		
F_0(V/Å)	E_0(eV)	E_2(eV/Å)	z_0(Å)	z_m(Å)	z_1(Å)	z_0(Å)	z_m(Å)	z_1(Å)
1	-0.018	0.18	0.96	-0.16	0.30	1.26	0.42	0.16
2	-0.034	0.40	0.81	-0.30	0.33	1.11	0.28	0.17
3	-0.050	0.63	0.69	-0.41	0.34	0.99	0.16	0.18
4	-0.065	0.86	0.61	-0.46	0.33	0.91	0.11	0.18
5	-0.079	1.10	0.51	-0.55	0.33	0.81	0.01	0.18
6	-0.092	1.34	0.43	-0.59	0.31	0.73	-0.04	0.17
7	-0.105	1.59	0.35	-0.62	0.28	0.65	-0.08	0.15

$$\left.\begin{aligned} H_{11} &= H_{1s,1s} = E_{1s} + V_F(z_\alpha) + \frac{1}{2}\, e\, F'(z_\alpha)\, x_1 \\ H_{12} &= H_{21} = H_{1s,2p} = e\, F(z_\alpha)\, x_3 \\ H_{22} &= H_{2p,2p} = E_{2p} + V_F(z_\alpha) + \frac{1}{2}\, e\, F'(z_\alpha)\, x_2 \end{aligned}\right] \tag{2.89}$$

where

$$\left.\begin{aligned} x_1 &= \langle 1s|(z-z_\alpha)^2|1s\rangle \\ x_2 &= \langle 2p|(z-z_\alpha)^2|2p\rangle \\ x_3 &= \langle 1s|(z-z_\alpha)|2p\rangle \end{aligned}\right] \tag{2.90}$$

Diagonalizing (2.88), one finds that the lowest eigenvalue (which for He corresponds to the state occupied by two electrons) is

$$E(F) = \frac{1}{2}\,(H_{22}+H_{11}) - \sqrt{\frac{1}{4}\,(H_{22}-H_{11})^2 + H_{12}^2}\ . \tag{2.91}$$

This is a highly non-linear function of the electric field and its derivative. In a weak and slowly varying field F, the change in total energy due to this field is

$$E(F) - E(0) \approx -\frac{1}{2}\kappa F^2 + \kappa_h F^4 + \kappa_{g_1} F' + \kappa_{g_2} F^2 F' + \kappa_{g_3} F^2 F'^2\ , \tag{2.92}$$

from which one can determine the polarizability,

$$\kappa = \frac{4\, e^2\, x_3^{\,2}}{E_{2p}-E_{1s}}\ , \tag{2.93}$$

the hyperpolarizability,

$$\kappa_h = \frac{2\, e^4\, x_3^{\,4}}{(E_{2p}-E_{1s})^3}\ , \tag{2.94}$$

and the constants in the field gradient correction terms

$$\kappa g_1 = e\ x_1 \tag{2.95}$$

$$\kappa g_2 = \frac{e^3\ (x_2-x_1)\ x_3{}^2}{(E_{2p}-E_{1s})^2} \tag{2.96}$$

$$\kappa g_3 = -\ \frac{e^4\ (x_2-x_1)^2\ x_3{}^2}{2(E_{2p}-E_{1s})^3}\quad . \tag{2.97}$$

The present theory thus includes all the contributions to the binding energy usually considered in phenomenological models.[4] Note, however, that the weak field approximation in the present numerical work is not invoked. The size of the various terms in eqn.(2.92) for He field adsorption will be commented upon later. At this stage, it should be pointed out that the inclusion of only 1s and 2p Slater orbitals for helium in the basis set gives a polarizability that is about a factor four too large for He; the case for W is the same, with a basis set of 6s, 6p and 5d orbitals. Therefore, the matrix elements of z have been reduced by a factor of two and those of z^2 by four before including the polarizability effects in the cluster calculations.

For $r_s = 1.5$, z_0 is replaced by z_0+0.3 Å.[37] z_m for $r_s = 1.5$ is obtained using the following simple prescription

$$(z_m-z_0)_{r_s=1.5} = \frac{\Omega_{r_s=1.5}}{\Omega_{r_s=3}}\ (z_m-z_0)_{r_s=3}\quad . \tag{2.98}$$

The values of Ω's are obtained using Table 2.4. E_0 and E_2 are kept the same. The corresponding z_1 values (see Appendix G), which match the field potentials at $z = z_0$, and as obtained from the equation

$$E_0 + E_2\ (z_0-z_m)^2 = e\ F_0\ z_1 \ln 2\quad , \tag{2.99}$$

are also given in Table 2.5, together with z_0 and z_m for $r_s = 1.5$.

c) Results of Field Adsorption of He

The numerical results of the cluster calculations in which the field penetration and the polarization effects have been included are now presented. Fig.2.17 shows the adsorption energy of helium adsorbed on a W cluster in a field, F_0, of 4 V/Å. For a big cluster, the total energy, E, is several hundred eV, whereas the adsorption energy, or the activation energy, as obtained from the difference of the two E's taken at z_{min} and at the activation barrier, varies on a scale less than an eV. This fact signals an inherent difficulty for (big) cluster calculations to produce accurate numerical results for adsorption energies.

Fig.2.17 shows the adsorption energy curves of He adsorbed on the apex of the near tetrahedral W_4 cluster (as described in Sect.1b(i)). In curve (a), all the polarization effects have been neglected, i.e., the energies in eqns (2.5) and (2.8), for the adsorbing He and also for the top-most W atom, have been shifted only by the local field energy. A reduced activation energy of about 0.2eV is obtained, as compared to 0.6eV in the previous calculation (of Sect.1), in which the asymptotic field is taken constant all the way to the position of the top-most W atom. The difference is due to the reduced field energy at the position of the He atom and to the shift on the top-most W atom. These latter two effects decrease the influence of the bonding due to the second-order perturbation expression (2.22), while affecting the two-body repulsive energy very little. Upon including the linear polarization term for the He atom (curve (b)), the activation energy is reduced and the adsorption potential widens. Including the linear polarization term for the top-most W atom, as well (curve (c)), reduces the activation energy

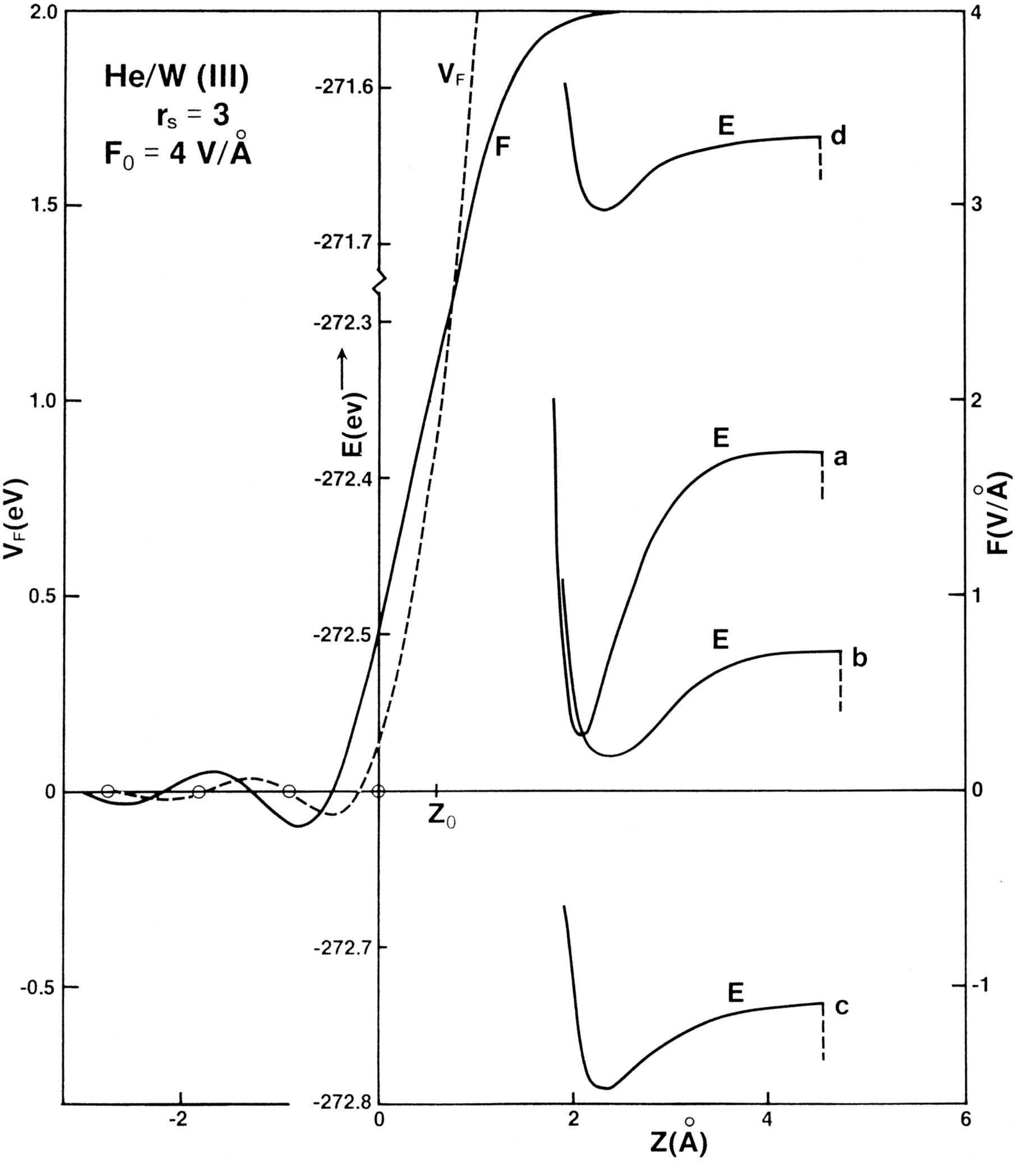

Fig.2.17: See Fig.2.16 for the details of F, V_F and z_0. E is the total energy of the He-W_4 cluster. (a), (b), (c) and (d) denote the inclusion of different terms in the Hamiltonian, as discussed in Sect.3c.

further. Finally, the inclusion of the z- and z^2-matrix elements (curve (d)) for He and for the top-most W, results in an activation energy of only 0.04eV in a field F_0 = 4V/Å. The complete field dependence of the activation energy, the position of the adsorption potential minimum, and the charge transfer on the He atom is depicted in Fig.2.18 for r_s = 3. The activation energy is a maximimum in fields between 6 and 7V/Å. This maximum should not be observable experimentally because the underlying W substrate starts to field evaporate around 5.5V/Å. The cluster size dependence has also been checked, by calculating a few points for He adsorbed on a W_{14} cluster. The results are within 20% of those in Fig.2.18. The adsorption properties for He on W(111), based on the r_s = 1.5 model of the jellium metal, and as given in Fig.2.19, vary within similar bounds. The results of the two r_s values can also help estimate the variation in the activation energy due to uncertainty in the jellium model calculations, which would not be more than 20%. The change in other quantities will be much smaller. These results clearly indicate that a reliable theory of field adsorption must include a very detailed treatment of the electric field at the metal surface around the adsorption site, preferably in a self-consistent manner.

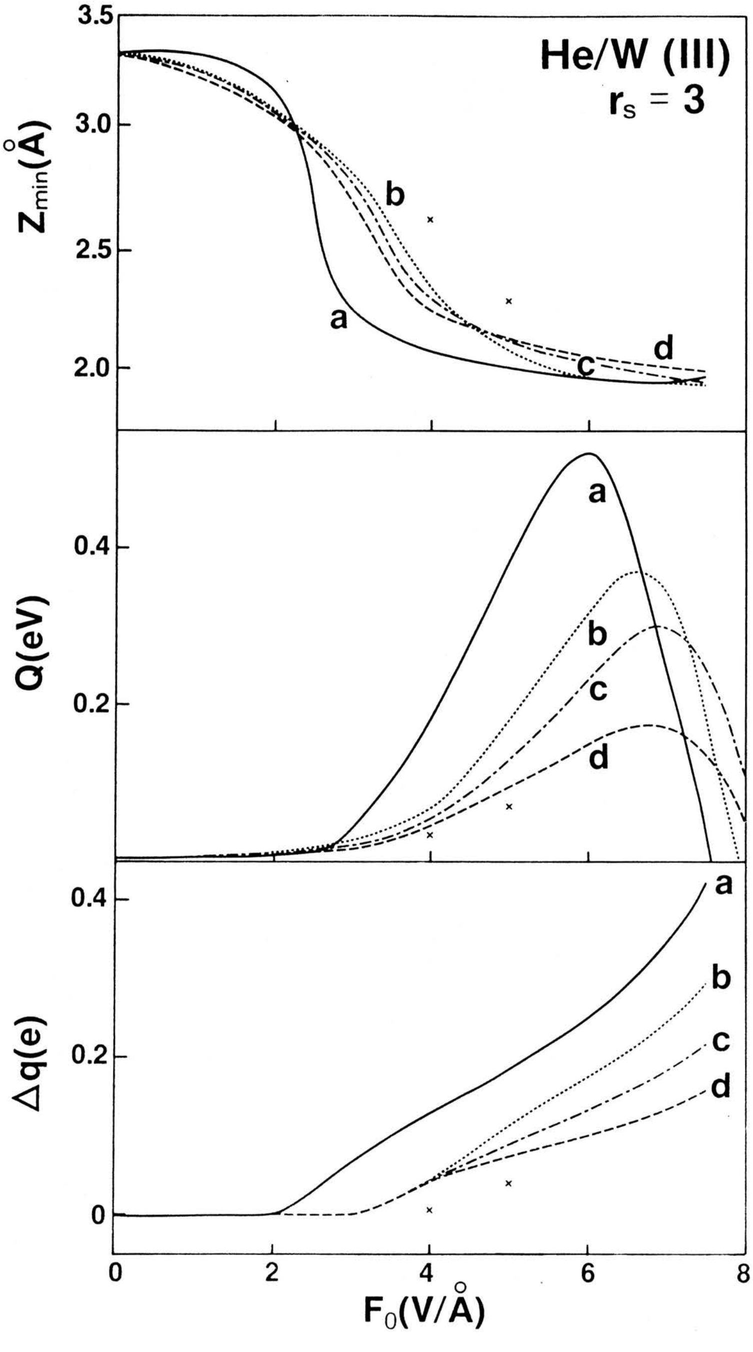

Fig.2.18: The position z_{min} of the adsorption potential minimum for the He-W_4 cluster, the activation energy Q, and the charge transfer Δq on the He atom as a function of the field strengths, F_0. (a), (b), (c) and (d) denote the inclusion of different terms in the Hamiltonian, as discussed in Sect.3c. The x - marks are for the He-W_{14} cluster (for the (d) curves).

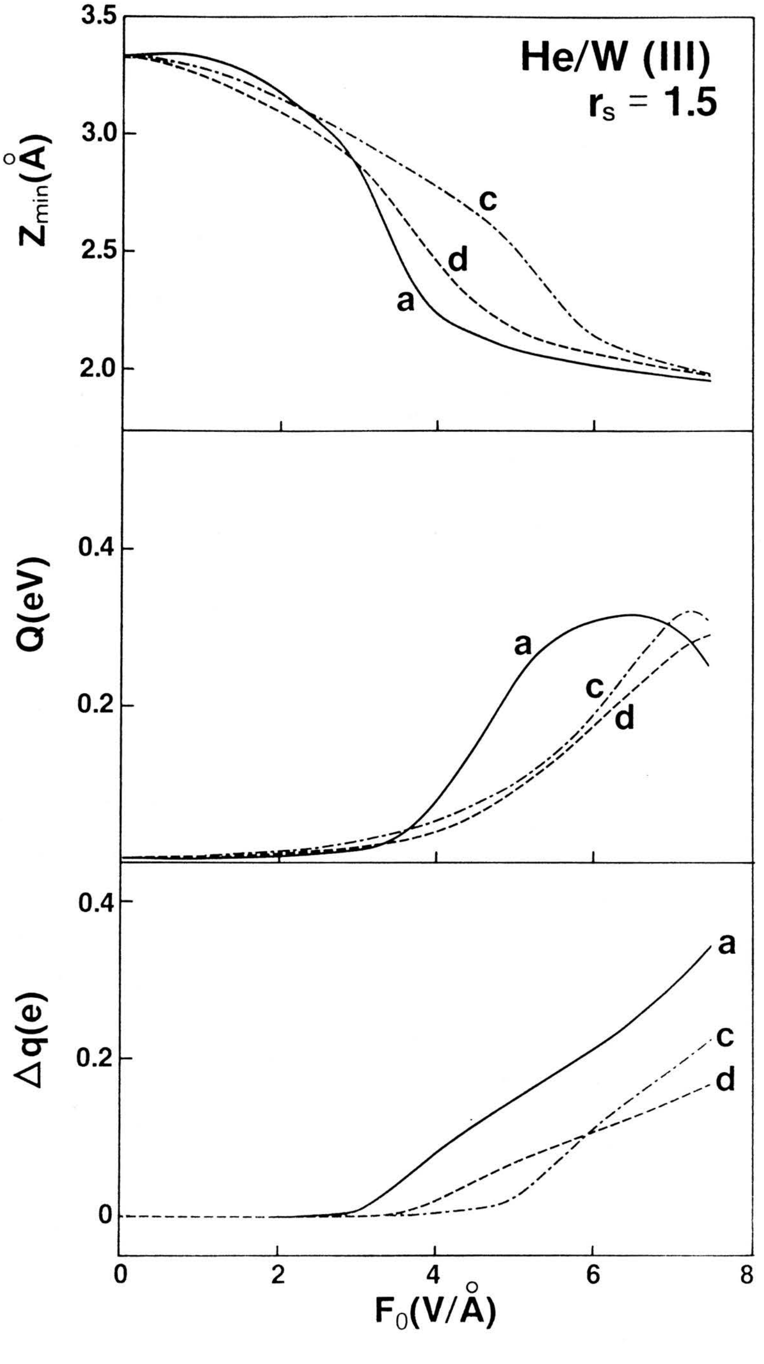

Fig.2.19: Same as Fig.2.18, but for r_s = 1.5.

CHAPTER III

Field Adsorption of H_2 and H_3 :

Hydrogen is the simplest of all the atoms in structure, but at the same time it is probably the most interesting as far as its adsorption properties are concerned. An addition of a few percent of hydrogen to helium as the image gas in a field ion microscope (FIM) surprisingly produces a very sharp helium ion image at the two-thirds of the normal best image voltage (BIV).[1] This strange effect is of practical use for imaging the less refractory metals. H^+, H_2^+ and metal hydride ions are also occasionally detected in the field desorption spectrum of FIM. This chapter deals with the relatively simple and basic phenomena of adsorption of H_2 and H_3 onto a metal surface (W(111)), and their formation and dissociation in the absence of, and also in the presence of, an electric field. These properties of H_2 and H_3 are studied using the ASED-MO theory and its formulation, as described and used in the first section of the previous chapter. Only the 1s orbital for the hydrogen atom is included in the calculation as the basis for which 1.2 $\mathring{A}^{-1}$ is taken as the Slater exponent[2] and -13.6 eV for the ionization energy of this 1s level. The choice of these parameters gives the right bond-length of 0.74Å for a free H_2 molecule, but the predicted binding energy is twice as great as the experimental value of 4.75 eV. It is hoped that the following results thus obtained will represent the character of the system qualitatively and to some extent quantitatively.

(i) H_2 :

As the H_2 molecule approaches the W(111) surface, from the gas phase, it physisorbs weakly. The energy of adsorption is in the range 0.3 - 0.6 eV, depending upon the site of the surface and the orientation of the molecule. The adsorption is physisorption in the sense that the molecular bond length, ξ, of H_2, varies only about 2% from its free space bond length, and the charge transfer to the H_2, molecule is negligible, as given in Table 3.1. There is an energy barrier of 1.0 to 1.8 eV, again depending on the configuration of the system, between this physisorbed precursor state[3] and the chemisorbed phase, where the H_2 molecule dissociates into two H atoms which are then trapped by the surface. This is in agreement with the evidence of a physisorbed molecular layer over the primary chemisorbed state (the energy of chemisorption is about 1.5 eV/particle).[4] Table 3.1 also lists the energy required for the molecule to go through these two channels, from its physisorbed state, namely, the separation channel (H_2 molecule going back to the gas phase) and the dissociation channel (the chemisorbed state). In presence of an electric field, the activation energy for the separation channel increases about ten-fold while the dissociation energy on the surface is greatly reduced (except in the case when the H_2 molecule approaches the surface upright). There is a gradual change from the physisorbed state to the chemisorbed state as the field strength is increased.

Fig.3.1 represents the arrangements of W atoms for the (111) surface and Fig.3.2 shows the different orientations of H_2 molecule on this surface at various sites. Configurations (1) and (2) (see Fig.3.2)

Table 3.1: Activation energy, Q, for the two channels for H_2 adsorption onto W(111), for various configurations (as given in Fig.3.2). z_1 is the separation of the closest H atom from the surface W atoms plane, z is the distance of the centre of mass of the H_2 molecule from this plane and ξ is the bond length of the two H atoms. Δq_1 and Δq_2 are charge transfers on the two H atoms at the (local) minimum position (in the H_2 - upright configuration Δq_1 is the charge on the H atom closest to the surface). The numbers appearing below the configuration number are the atom numbers which constitute the W-cluster (see Fig.3.1). Results are also presented for linear W-H-H (see Fig.3.7).

Configuration	F (V/Å)	Q (eV)		z_1^{min} (Å)	z^{min} (Å)	ξ^{min} (Å)	Δq_1 (e)	Δq_2 (e)
		Separ. Chann.	Dissoc. Chann.					
(1) upright	0	0.3	1.7	2.24	2.60	0.722	-0.02	-0.05
1 8 9 10	1	3.5	2.0	1.83	2.21	0.753	-0.07	0.01
	2	1.6	0.4	1.71	2.13	0.843	-0.12	0.3
(2) flat	0	0.3	1.5		2.11	0.745	-0.04	-0.04
1 3 4 8	1	4.2	0.4		1.47	0.766	-0.06	-0.06
14 15 17	2	--	--	--	--	--	--	--
(3) flat	0	0.3	1.0		2.07	0.74	-0.04	-0.04
1 2 3 8	1	4.4	0.2		0.93	0.795	-0.06	-0.06
10 14 17	2	--	--	--	--	--	--	--
(4) flat	0	0.6	1.0		0.904	0.756	-0.08	-0.08
1 2 3 8	1	5.6	0.4		0.07	0.795	-0.15	-0.15
10 11 14	2	5.6	0.2		-0.05	0.808	-0.15	-0.15

Table 3.1 (continued):

Configuration	F (V/Å)	Q (eV)		z_1^{min} (Å)	z^{min} (Å)	ξ^{min} (Å)	Δq_1 (e)	Δq_2 (e)
		Separ. Chann.	Dissoc. Chann.					
(5) flat	0	0.3	1.5		2.01	0.756	-0.03	-0.03
1 3 4 8	1	4.4	0.6		1.14	0.768	-0.09	-0.09
14 15 17	2	3.6	0.2		0.74	0.822	-0.06	-0.06
(6) flat	0	0.4	1.3		2.26	0.74	-0.06	-0.06
1 2 5 9	1	4.0	0.8		2.09	0.781	-0.04	-0.04
10 14 15	2	2.4	0.2		1.89	0.849	0.02	0.02
(7) flat	0	0.3	1.4		2.23	0.746	-0.05	-0.05
1 2 3 5	1	3.8	0.8		2.08	0.782	-0.04	-0.04
6 9 14	2	2.2	0.2		1.88	0.843	0.02	0.02
(8) upright	0	0.5	1.8	0.74	1.12	0.754	-0.03	-0.05
1 2 3 8	1	5.0	1.4	0.373	0.746	0.747	-0.11	-0.08
10 11 14	2	4.4	2.8	-0.06	0.311	0.746	-0.15	-0.04
(9) upright	0	0.4	1.7	1.26	1.64	0.746	-0.03	-0.06
1 3 4 8	1	4.2	2.2	1.16	1.54	0.761	-0.08	-0.03
14 15 21	2	3.0	2.4	1.08	1.47	0.781	-0.12	0.05
H_2 - W	0	0.2	1.7	2.42	2.80	0.754	-0.01	-0.03

The values are good to only two significant figures. However, these figures are retained for comparisions.

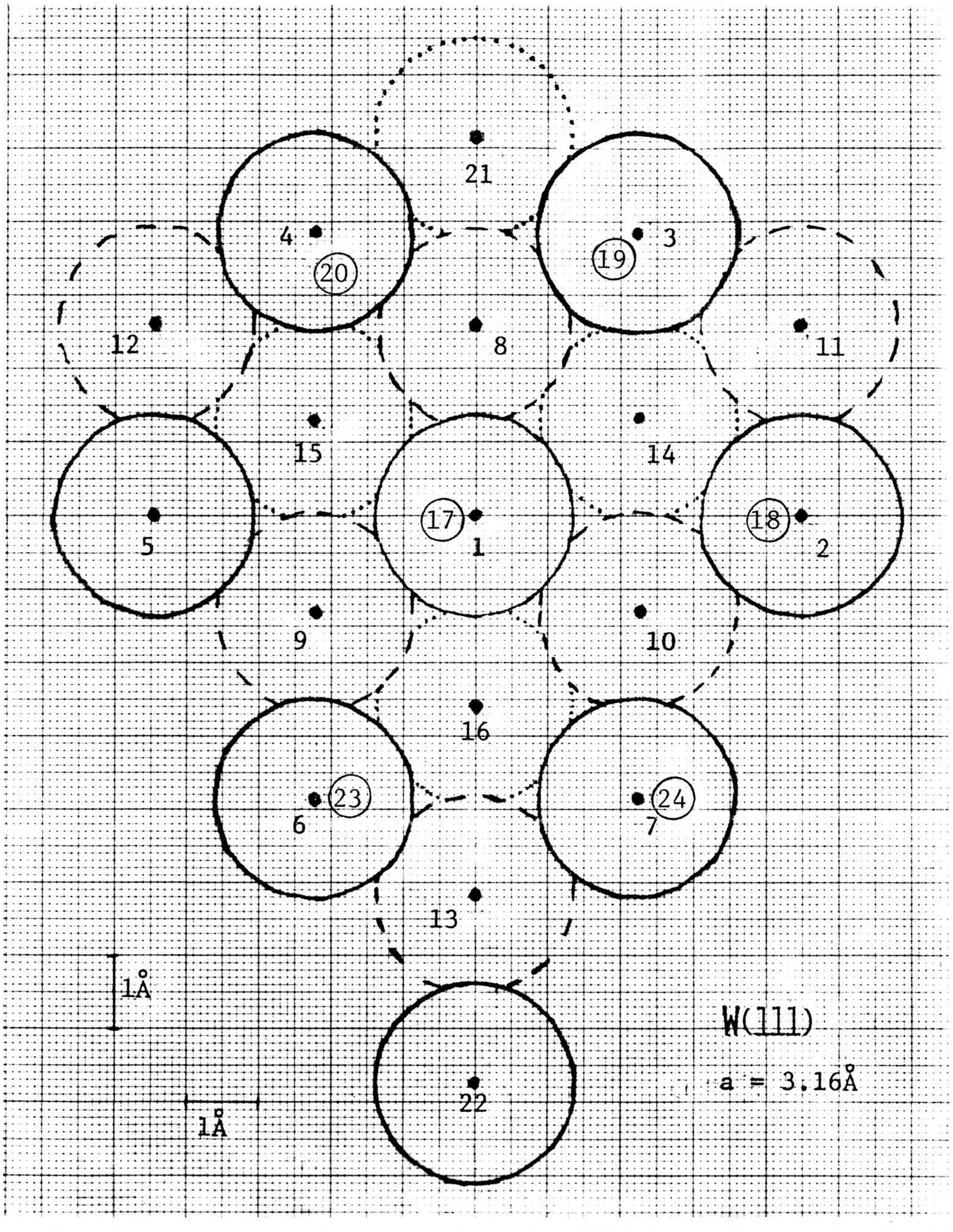

Fig.3.1: Arrangement of atoms for the W(111) surface. The lattice constant, a, for the b.c.c. structure is 3.16Å. The full circles represent the surface atoms (1 to 7 and 22), the dashed circles represent the atoms from the second layer (8 to 13), and the dotted circles represent the atoms from the third layer (14 to 16 and 21). The fourth layer atoms are below the surface atoms, for which the atom numbers have been circled (e.g. atom 17 is below atom 1, 18 below 2, etc.). The separation between adjacent layers is $a/2\sqrt{3}$ and the nearest neighbour distance is $\sqrt{3}\,a/2$.

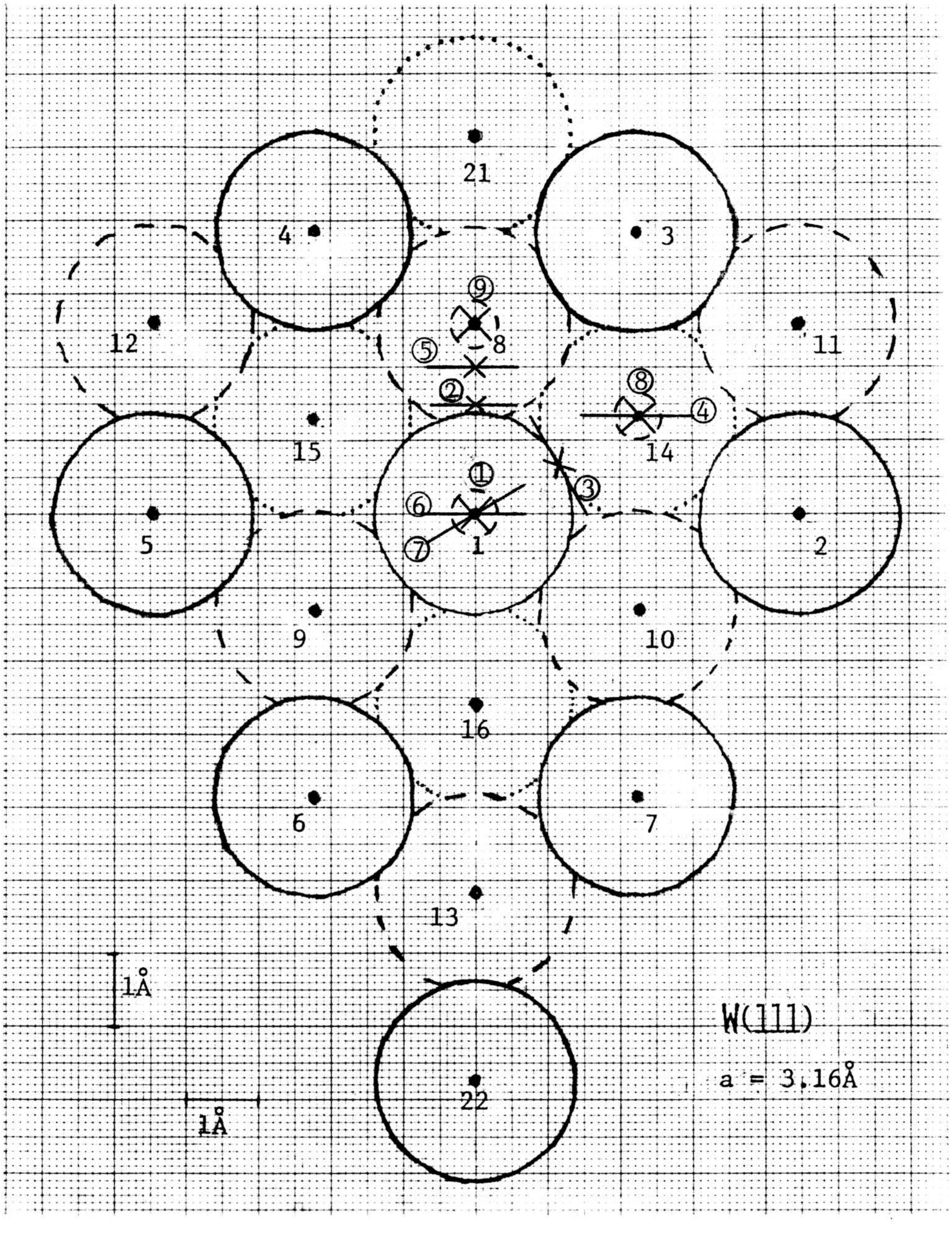

Fig.3.2: Different configurations of H_2 molecule approaching the W(111) surface. A ✕ and a bar (—) show the centre of mass of a flat molecule and the orientation of the H-H bond, respectively. A ✕ with a dashed circle represents H_2 upright on the surface. The circled numbers represent the configuration numbers as referred to in the text and in Table 3.1. Table 3.1 also gives the molecule numbers (as given in Fig.3.1) for these configurations.

will be discussed in more detail below, where the H_2 molecule approaches the surface as upright and as flat, respectively. The results for other configurations are also presented and analysed on the basis of those for configurations (1) and (2).

In configuration (1), the H_2 molecule approaches the surface as upright above a W atom and is trapped in the surface potential with the energy of adsorption ~ 0.3eV in the absence of a field (Fig.3.3). The contour plots of the ground state energy for this configuration are given in Fig.3.4 for F = 0, 1, and 2V/Å. The bond length, ξ, between the two H atoms increases from 0.72Å to 0.75 and 0.84Å in the presence of the field of 1 and 2V/Å, respectively. The distance, z_1, between the top W atom and the closest H atom decreases greatly from 2.37Å to 1.84 and 1.7Å, respectively, in these fields (see Table 3.1). At a higher field of ~ 2.2V/Å the H-H bond is broken and the farthest H atom is ripped off by this field, leaving behind the other H atom to be chemisorbed. The force constants for the H_2 molecule have been calculated using eqn.(2.9) for the equilibrium positions (the physisorbed states) and have been presented in Table 3.2, together with the corresponding wave numbers for various fields. With an increase of the field, the force constant decreases and the potential well becomes shallower. The perspective view of the ground state energy surface of H_2, corresponding to the contour of Fig.3.4, is given in Fig.3.5, for F=0 and F=1V/Å. The contour plots, similar to the ones in Fig.3.4, are given in Fig.3.6 but this time these show z_1 vs. ξ as compared to the z (the distance between the centre of mass of the H_2 molecule and the plane containing the surface W atoms) vs. ξ. The range of ξ is also increased considerably to study the dissociation property of H_2 on the W surface. The contour plot of the

Table 3.2: Force constant and the corresponding wave numbers for H_2.

	Free H_2		H_2/W(111) (Config.1)		
	Expr.[(a)]	Present theory	F=0	F=1V/Å	F=2V/Å
Force const. (milli dyne/Å)	5.23	7.98	8.72	8.23	2.94
Wave no. (cm^{-1})	4200	5180	5420	5270	3150

(a) G. Herzberg, Molecular spectra and molecular structure I. Spectra of Diatomic Molecules (Van Nostrand Reinhold Company, N. Y., 1950)

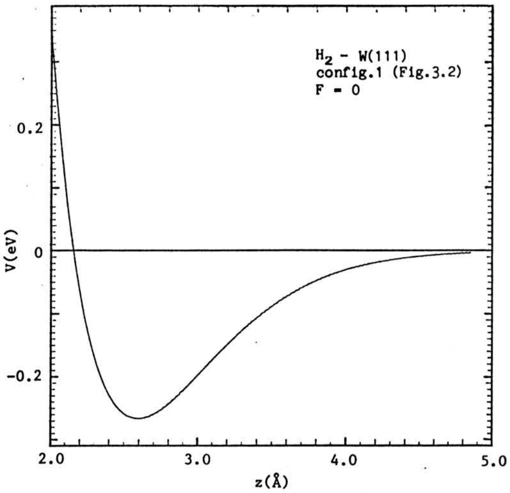

Fig.3.3: Surface potential V for H_2 upright on the near tetrahedral W_4 cluster (Config.1). Bond length, ξ, between the two H atoms changes from 0.74Å to 0.72Å as H_2 comes from its gas phase to the potential minimum.

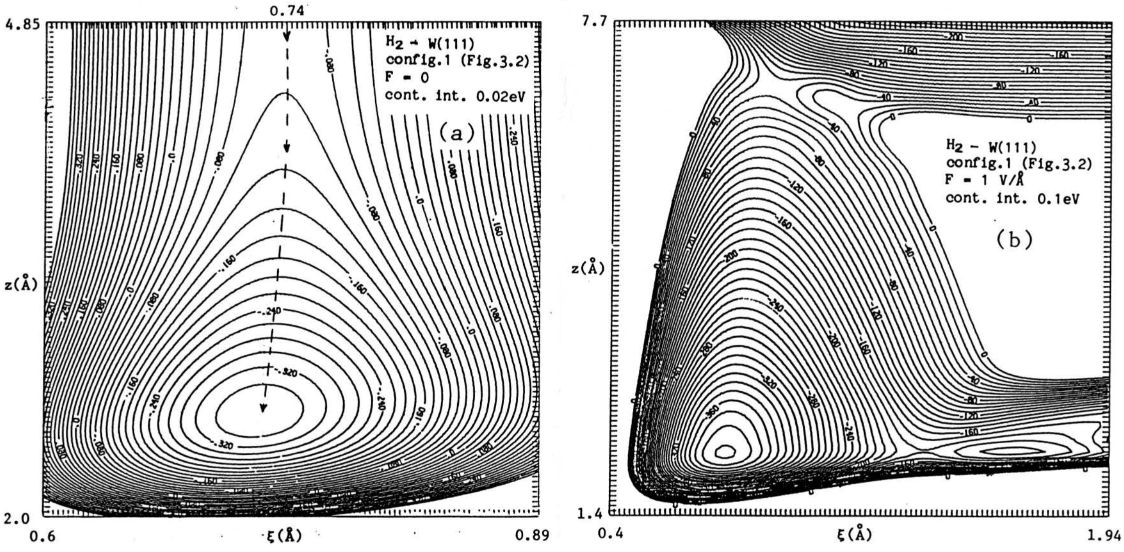

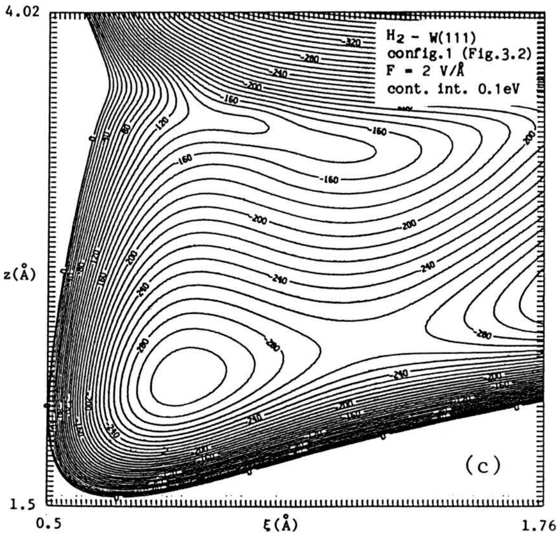

Fig.3.4: Contour plot of the ground-state energy surface of H_2 interacting with a tungsten cluster (Config.1) for (a) F=0, (b) F=1V/Å, and (c) F=2V/Å. z is the distance of the centre of mass of the H_2 molecule from the surface (top W atom) and ξ is the H-H bond length.

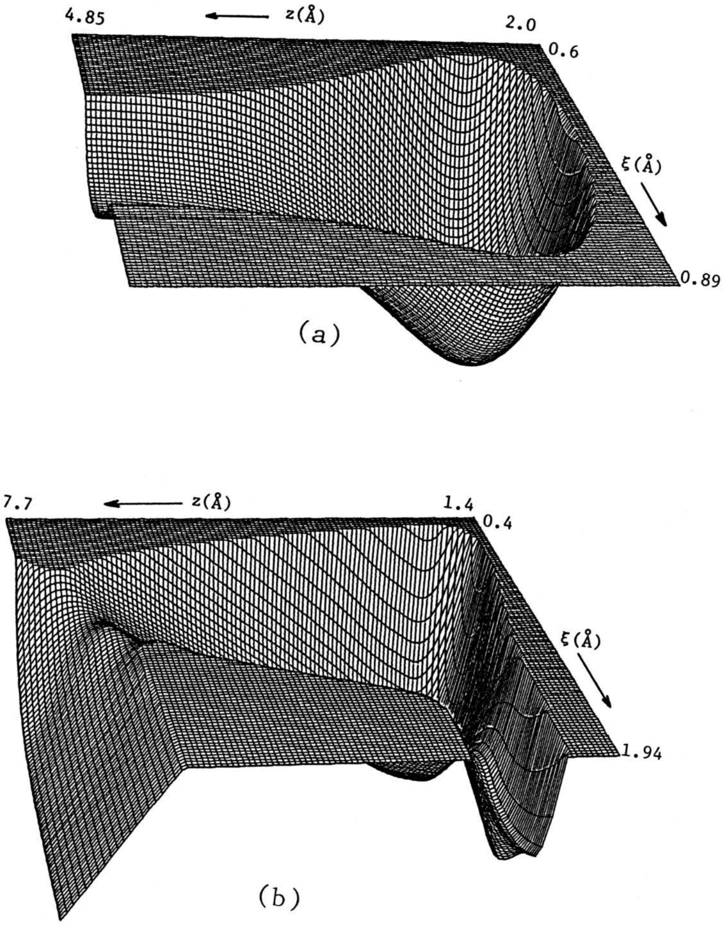

(a)

(b)

Fig.3.5: Perspective view of the ground-state energy surface corresponding to the contour map of Fig.3.4 for (a) F=0 and (b) F=1V/Å.

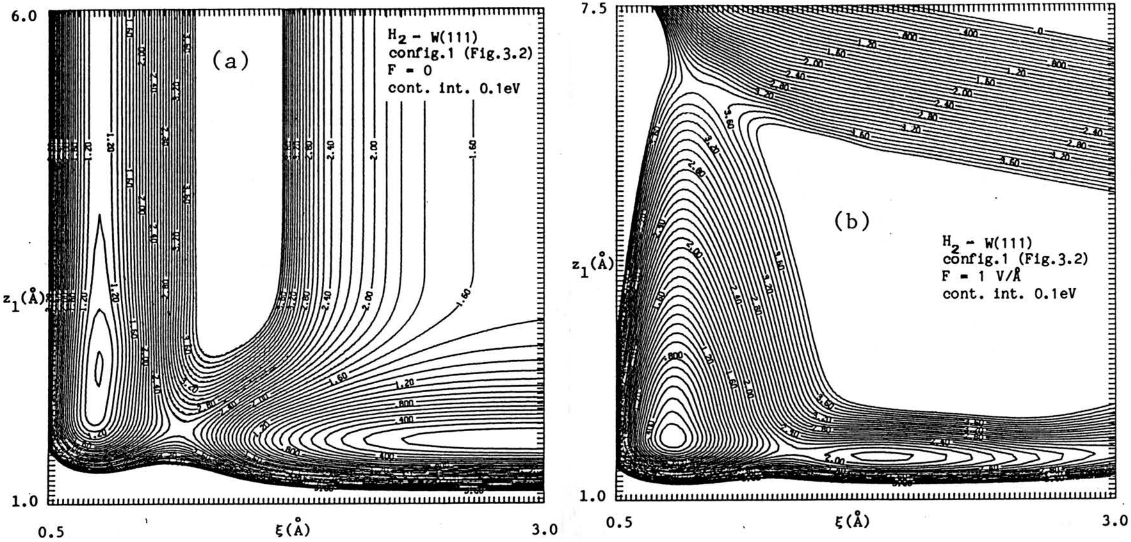

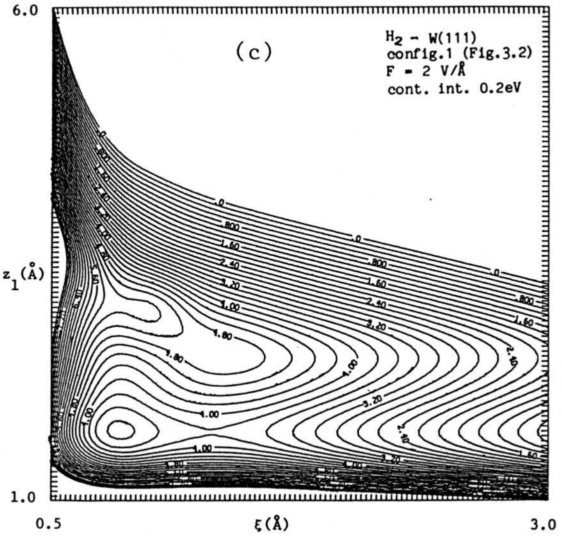

Fig.3.6: Contour plot of the ground-state energy surface of H_2 interacting with a tungsten cluster (Config.1) for (a) F=0, (b) F=1V/Å and (c) F=2V/Å. z_1 is the distance between the top surface atom and the closest H atom and ξ is the H-H bond length.

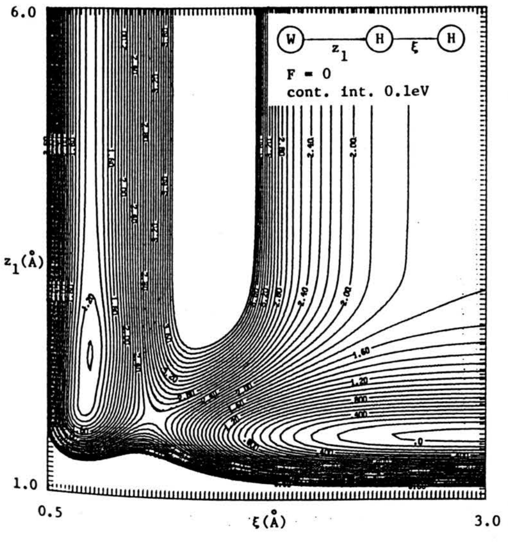

Fig.3.7: Contour plot of the ground-state energy surface of H_2 interacting with a W atom in zero field.

ground-state energy of H_2 and W (linear configuration) is presented in Fig.3.7. The similarity between Figs 3.6a and 3.7 facilitates the study of the adsorption of H_2 onto W. For $z_1 \geqq 2Å$ the closed shell of the 1s orbital of the H_2 molecule remains almost intact. If z_1 is decreased at the expense of an energy of about 1.5eV, the covalent bonding between the H atoms is broken, and instead there is a formation of a stronger bond between the W and the closest H atoms, giving rise to a tungsten hydride.

In configuration (2), a H_2 molecule approaches the surface with the H-H bond parallel to it. The contour maps of the energy of the system as a function of z and ξ are given in Fig.3.8 for F = 0, 1 and 2V/Å. Three dimensional perspective views of the energy surfaces are depicted in Fig.3.9 for F=0 and 1V/Å. In Fig.3.9a (F=0), an adsorbing molecule approaches the surface through the entry valley (arrow in the left upper corner in Fig.3.8a) first encountering a shallow minimum where it can be trapped in a weakly physisorbed precursor state P. Eventually it will try to climb over the saddle point, S, by streching its bond length ξ. If successful, the bond will break and the two dissociated H atoms will be trapped at the surface at D. They can even diffuse into the metal. For energetic reasons, the system will try to hug the path of steepest ascent and descent; this path is commonly parametrized by a reaction coordinate; the path's energetics are illustrated in Fig.3.10. Basically the same thing happens for F=1V/Å where dissociation is energetically more favourable. This barrier from physisorption to chemisorption disappears for the field strength of 2V/Å.

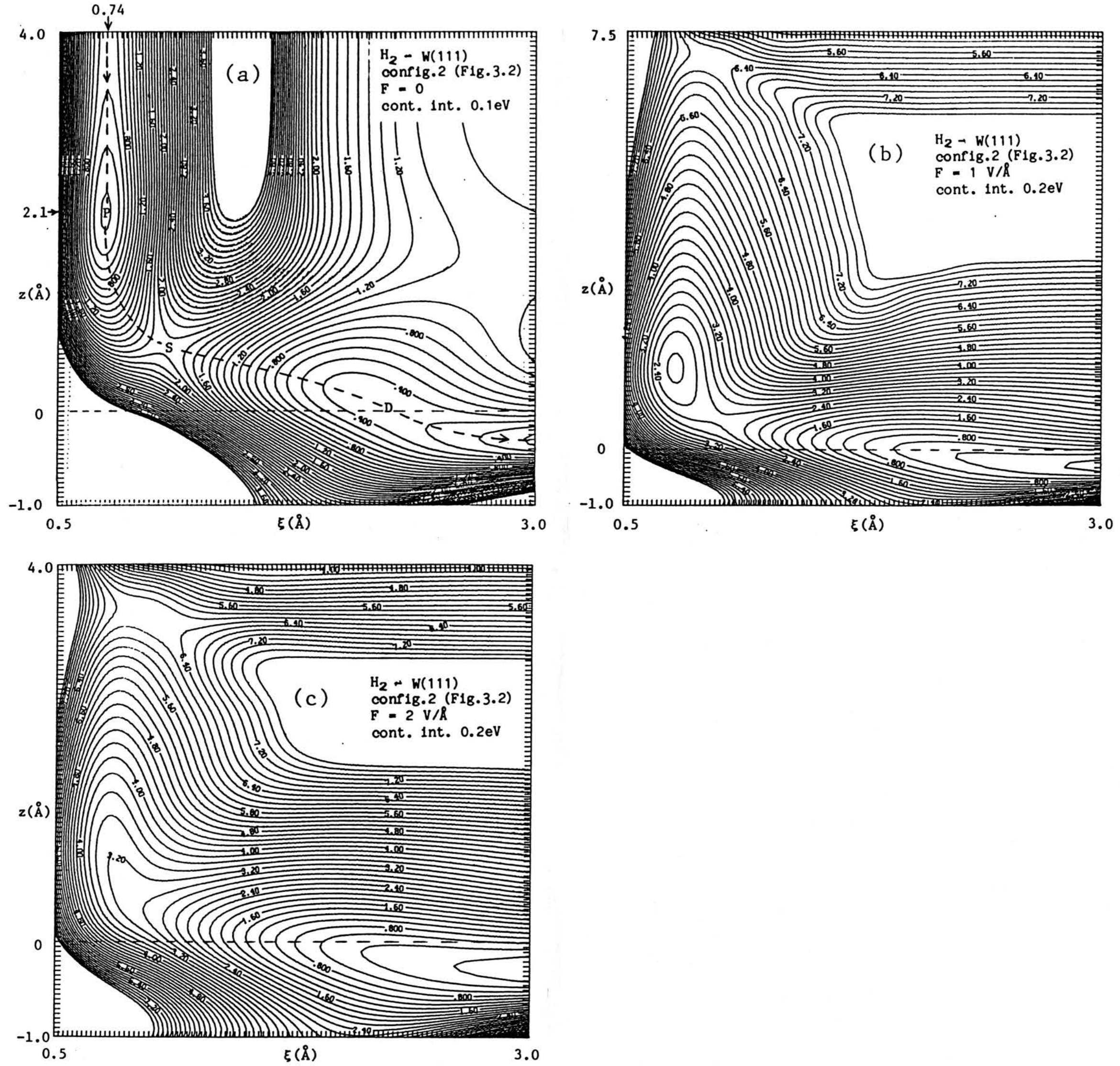

Fig.3.8: Contour plot of the ground-state energy surface of H_2 interacting with a tungsten cluster (Config.2) for (a) F=0, (b) F=1V/Å, and (c) F=2V/Å. z is the distance of the centre of mass of the H_2 molecule from the surface (top W atom) and ξ is the H-H bond length.

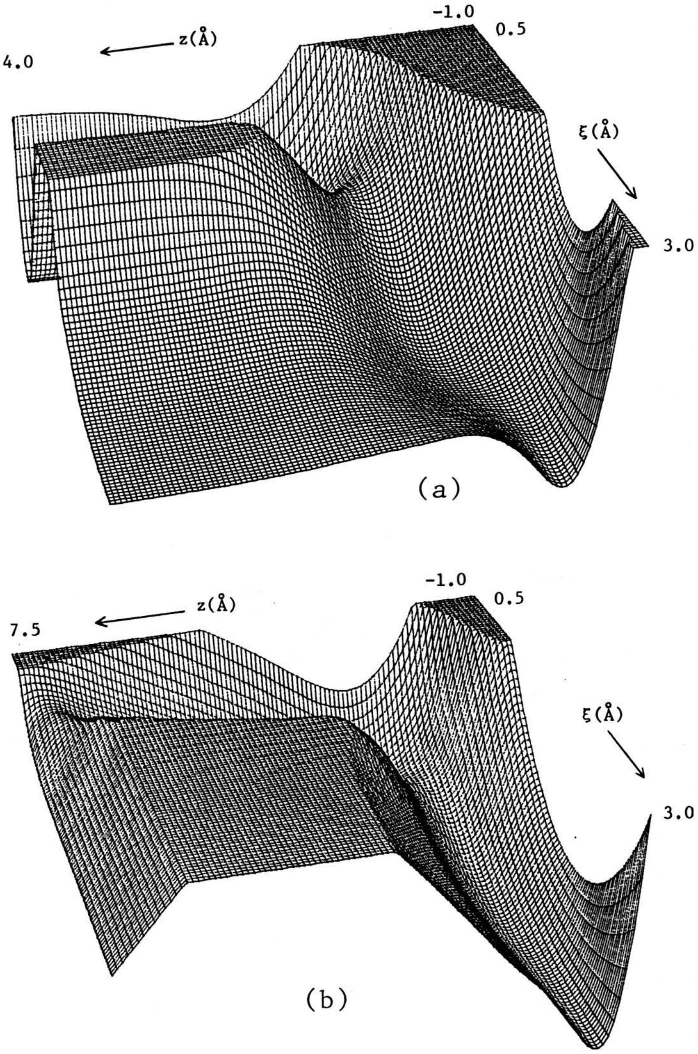

Fig.3.9: Perspective view of the ground-state energy surface corresponding to the contour map of Fig.3.8 for (a) F=0 and (b) F=1V/Å.

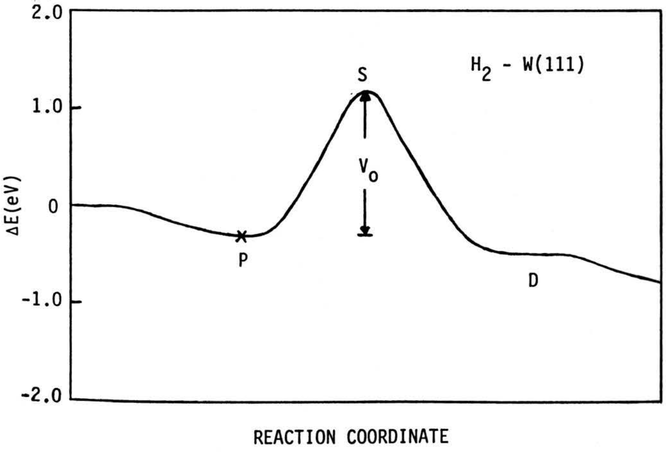

Fig.3.10: Change in ground-state energy of H_2 interacting with a tugsten cluster (Config.2) along the reaction coordinate as shown in Fig.3.8a.

Essentially, for configurations (3 to 7), the description for configuration (2) also applies. Looking at Fig.3.2 and the energy surface contour maps (Figs 3.11 to 3.15), one observes that unlike the rare gases, H has a tendency to bind more on three fold sites. In configuration (3) one H atom prefers the site close to W atoms, numbered 1, 8 and 14, and the other H prefers the site close to 1, 8 and 15. A similar thing happens for configuration (4). In configurations (8) and (9) (the energy surface contour maps of z_1 vs. ξ are given in Figs 3.16 and 3.17), the stretching of the bond is relatively small (as compared to the H_2 molecule approaching the surface as flat) as one increases the field strength. The reason is: the H atom, adjacent to the surface, sits in the groove of the three-fold site, allowing the farthest H atom to move even closer due to an increased orbital overlap. (Remember that at the three-fold site the H-W two-body repulsion energy is small.)

(**ii**) H_3 :

In free space H_3 does not form. Energetically, it is more favourable to dissociate into a H_2 molecule (the calculated binding energy is 9.63eV) and an H atom. This phenomenon is illustrated in Fig.3.18 for a linear arrangement of three H atoms where, for the saddle point $\xi_1=\xi_2=1\text{Å}$, the binding energy is 8.98eV. In Fig.3.19, a non-linear configuration of three H atoms has been considered and a contour map is presented as a function of ξ (the separation between two H atoms) and z (the distance between the third H atom and the centre of mass of the other two). Again the most probable configuration is H_2+H. Fig.3.19 shows also that a linear configuration is preferred to a non-linear one with a

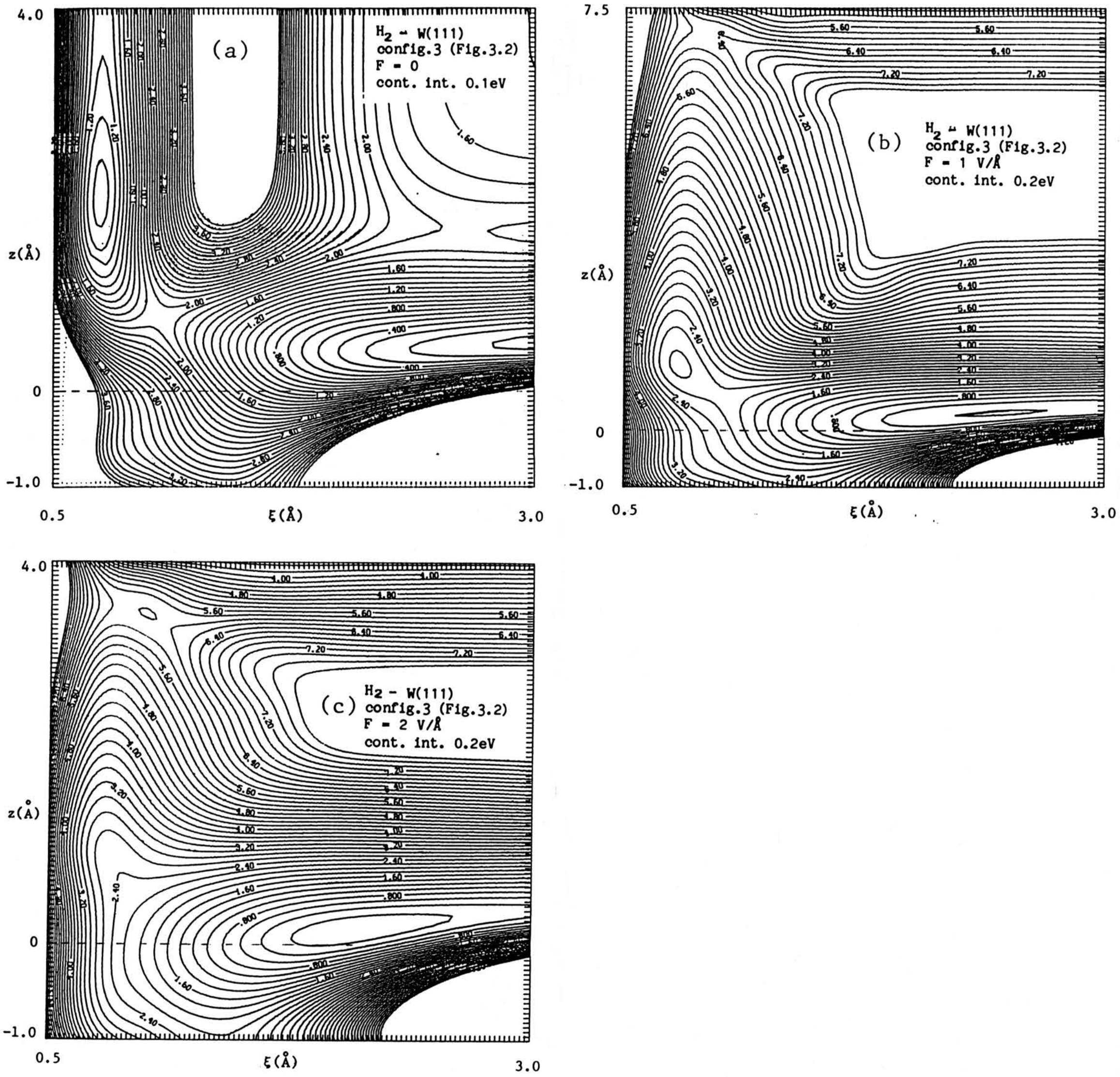

Fig.3.11: Same as Fig.3.8, but for configuration 3.

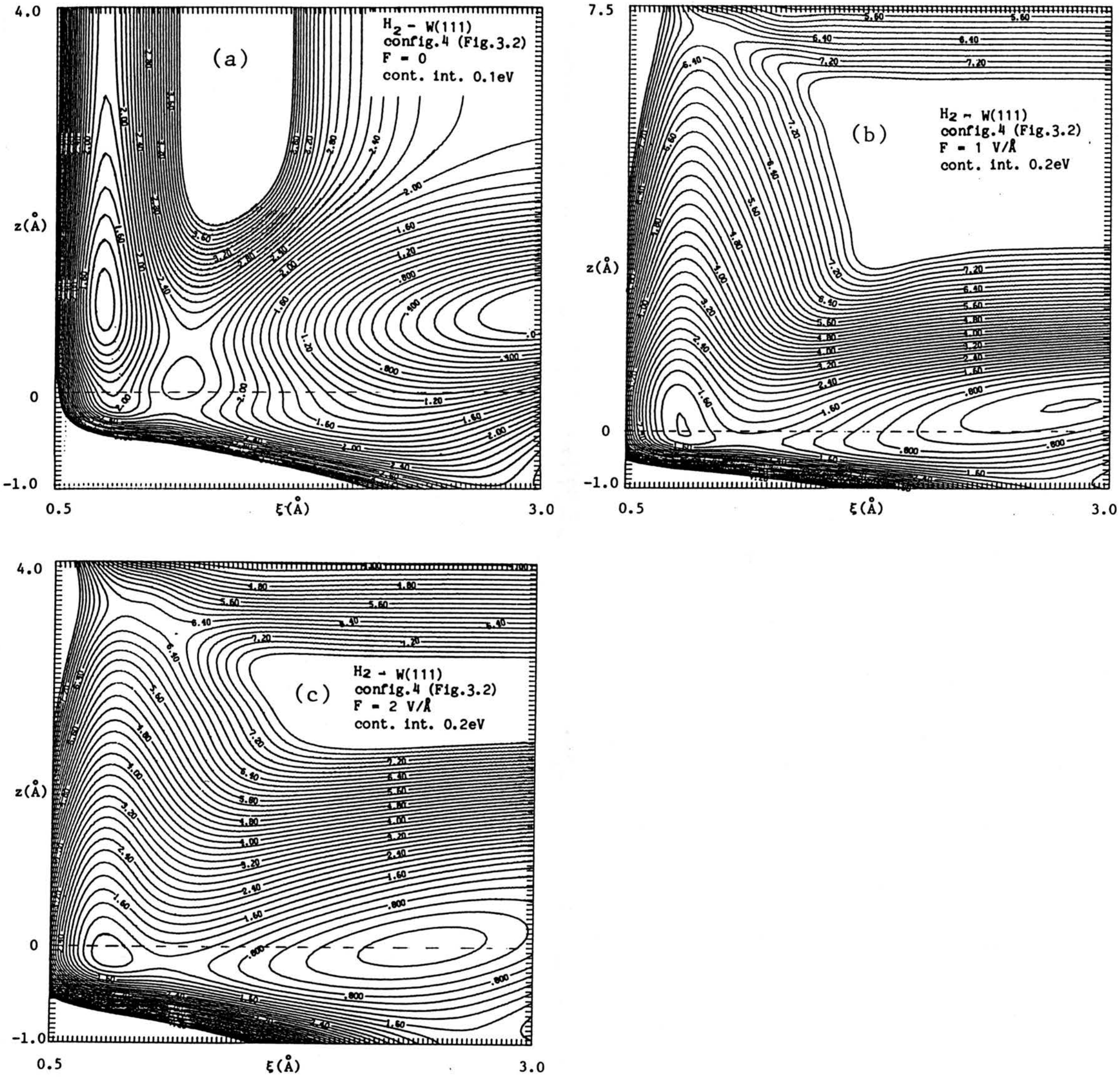

Fig.3.12: Same as Fig.3.8, but for configuration 4.

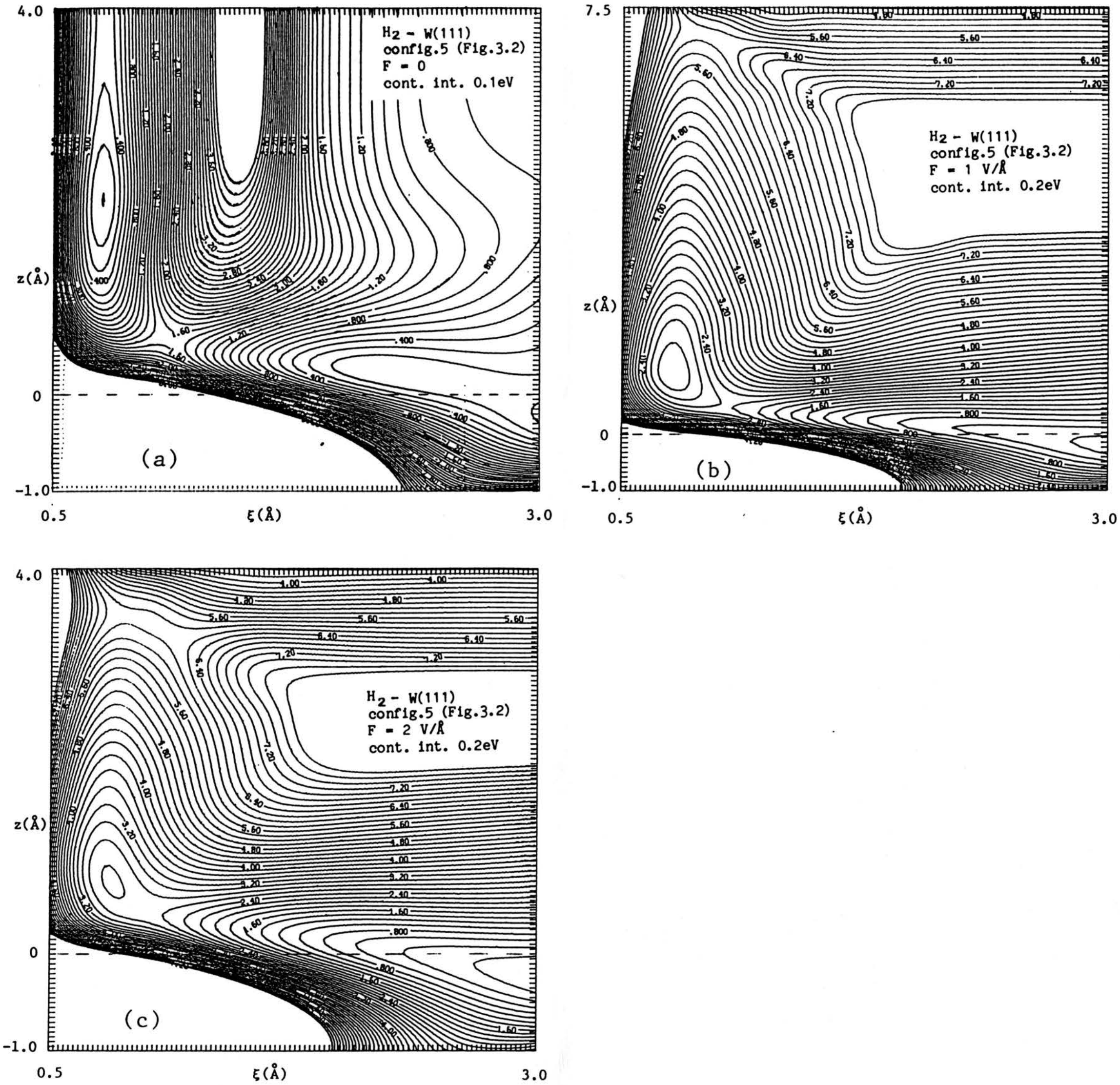

Fig.3.13: Same as Fig.3.8, but for configuration 5.

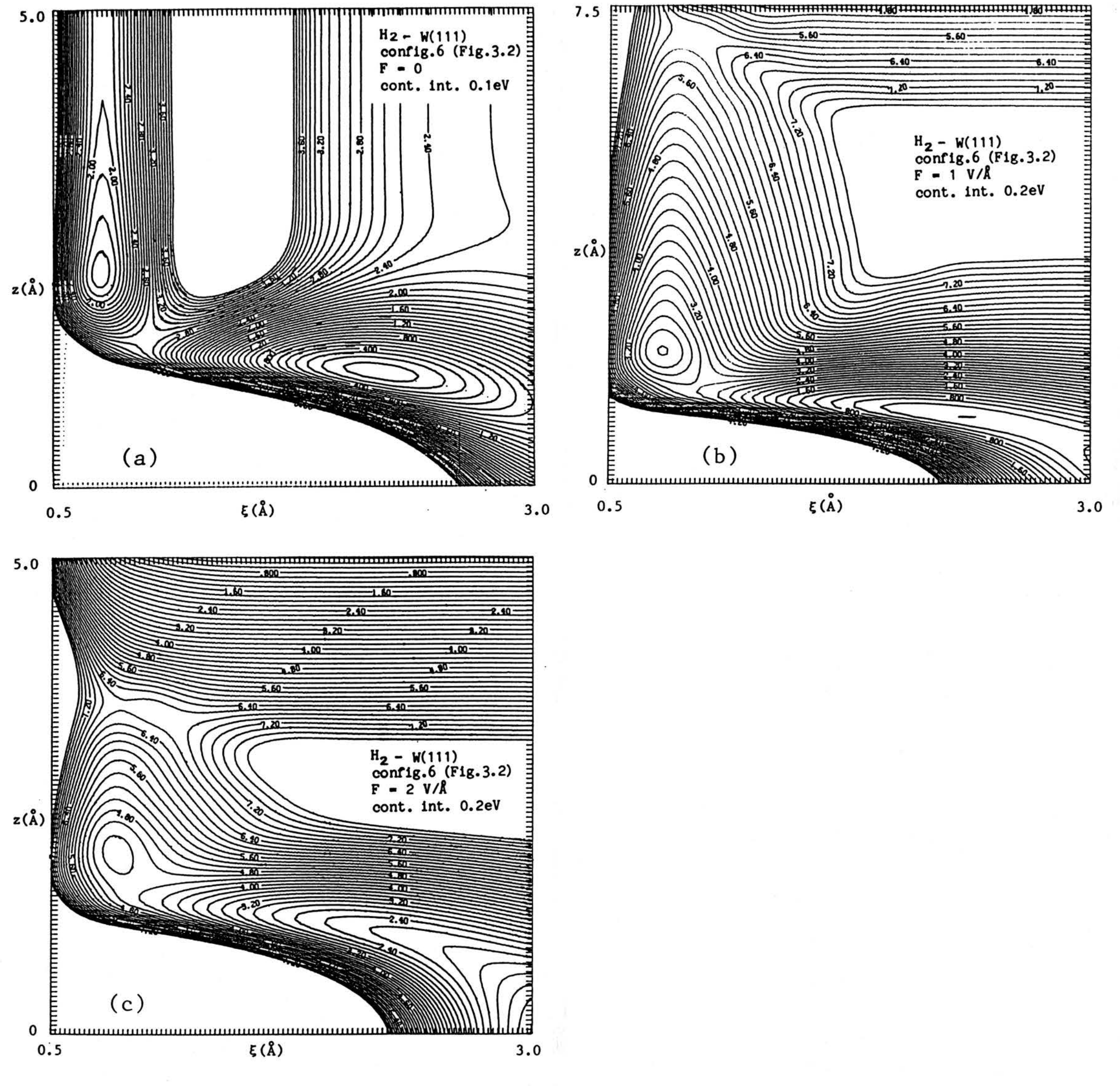

Fig.3.14: Same as Fig.3.8, but for configuration 6.

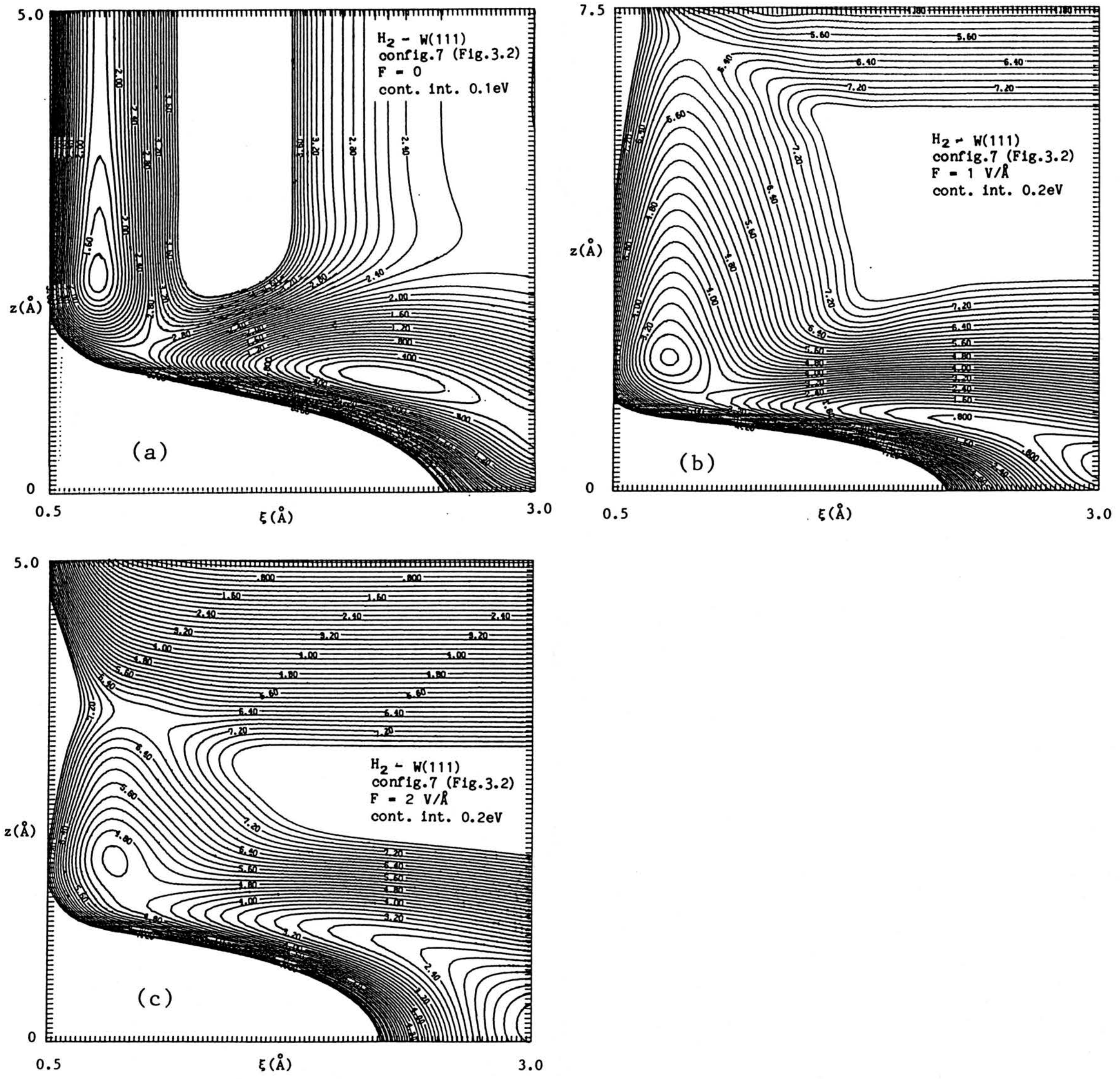

Fig.3.15: Same as Fig.3.8, but for configuration 7.

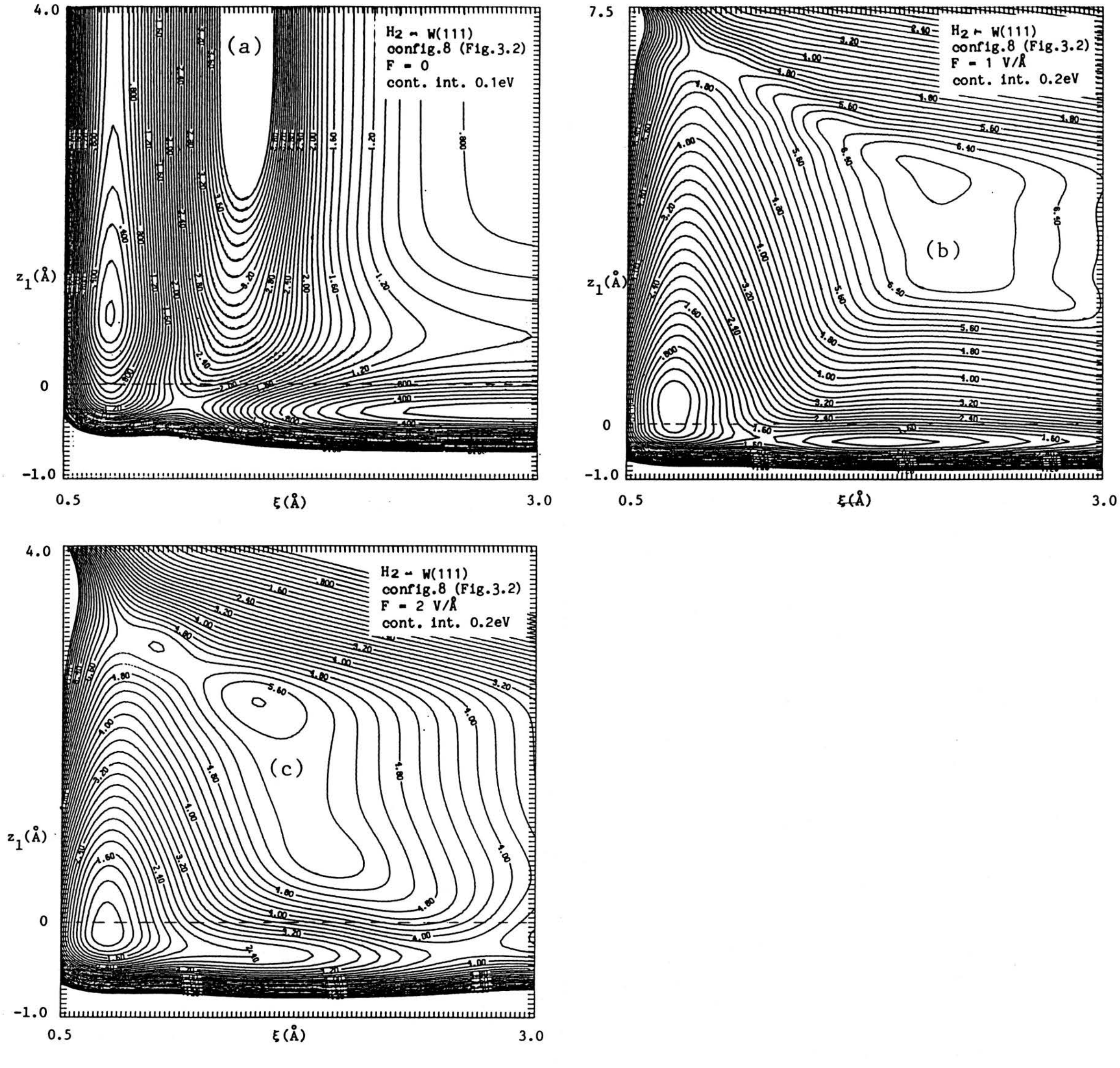

Fig.3.16: Same as Fig.3.6, but for configuration 8.

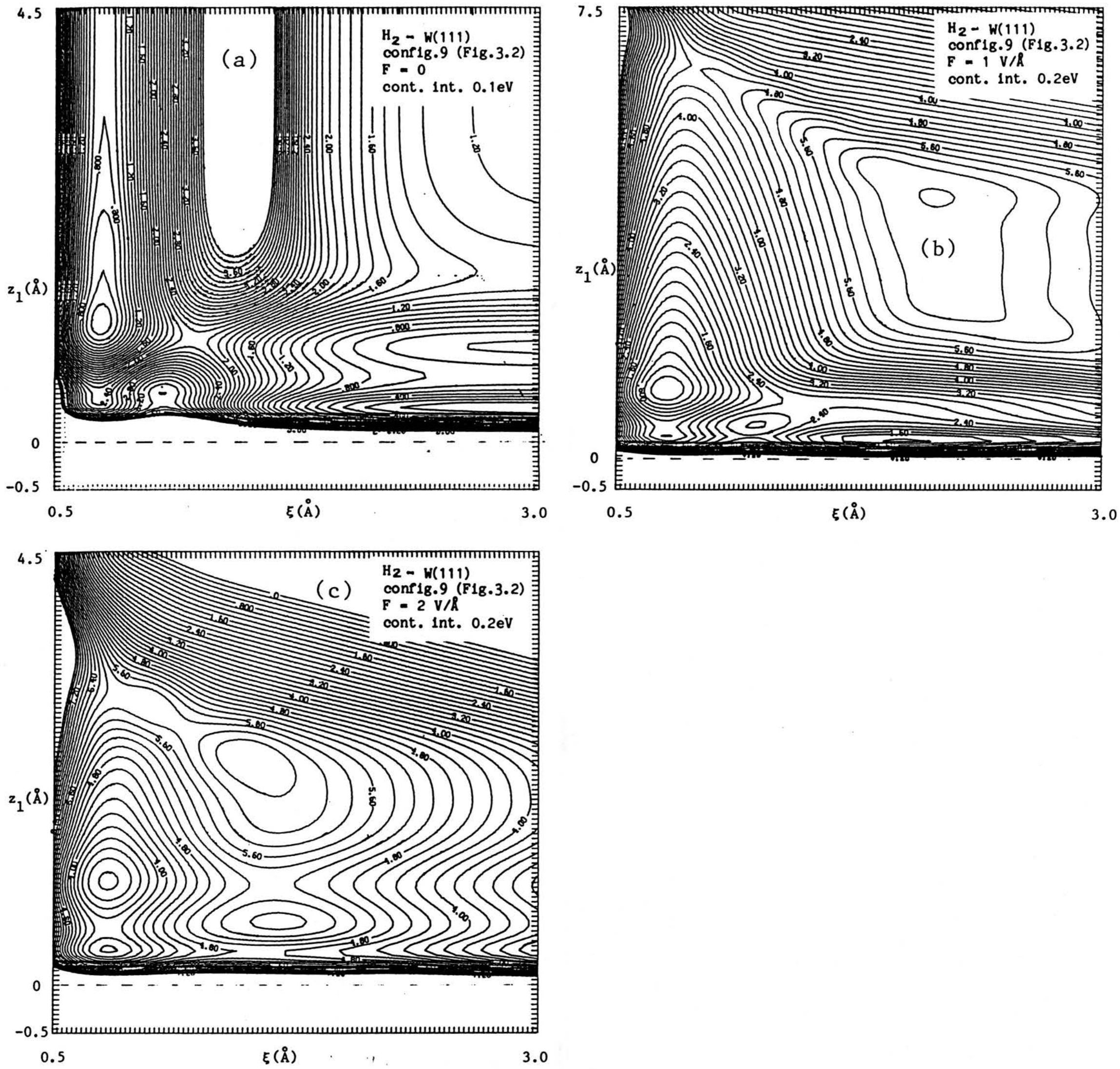

Fig.3.17: Same as Fig.3.6, but for configuration 9.

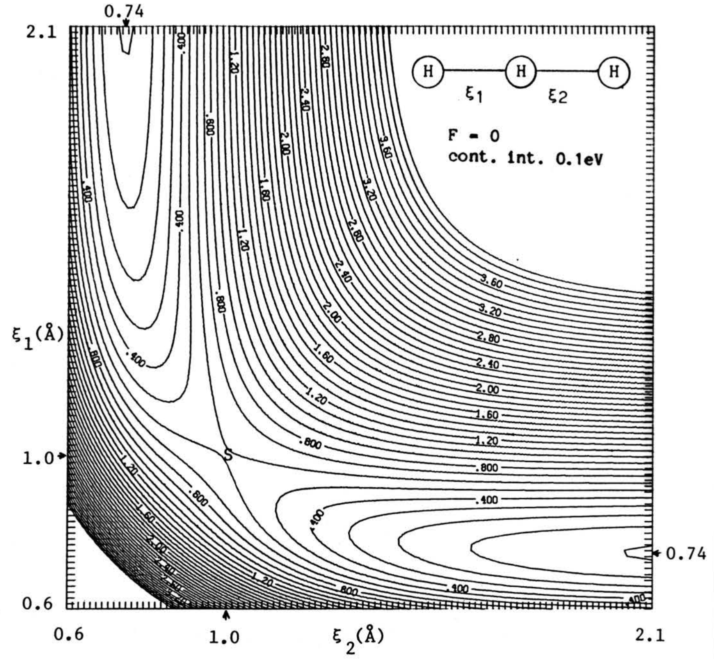

Fig.3.18: Contour plot of the ground-state energy surface of the linear H_3 in zero field. Energetically it is favourable to form $H + H_2$ (with bond length of 0.74Å). S is the saddle point corresponding to $\xi_1 = \xi_2 = 1.0$Å.

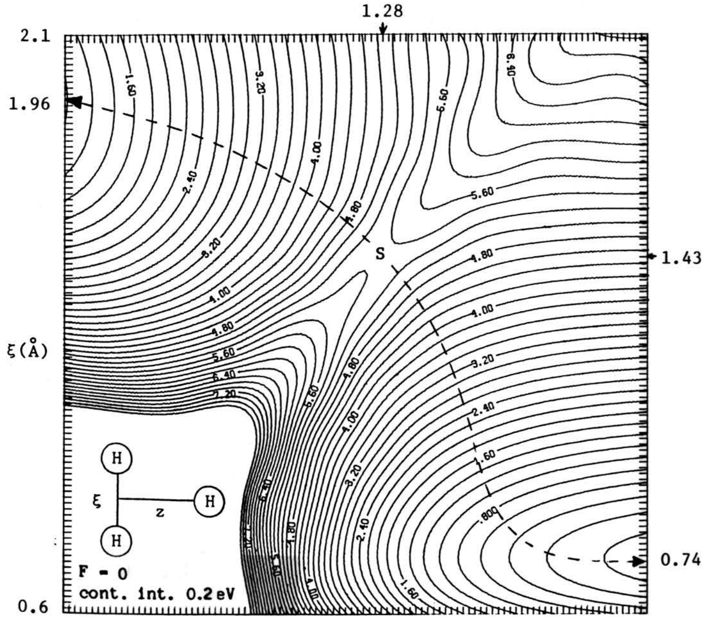

Fig.3.19: Contour plot of the ground-state energy surface of the non-linear H_3 in zero field. Energetically it is favourable to form $H + H_2$ (with bond length of 0.74Å). The linear configuration is more likely than the non-linear configuration. S is the saddle point corresponding to the equilateral triangle of side 1.45Å.

saddle point, S, representing the situation when all the three H atoms form an equilateral triangle with side of length 1.45Å. Liu[5] and Siegbahn[6] have obtained similar results with their $\xi_1=\xi_2=0.93$Å being the saddle point.

Next the adsorption of linear H_3 onto $W_4(111)$ (configuration 1 of Fig.3.2) is considered, increasing from zero field to a field where the local minimum disappears. The existence of linear H_3 is confirmed in the presence of a surface.[7,8] The calculations are presented in Table 3.3. z_1 is the distance between the surface atom and the closest H atom. ξ_1 is the distance between the middle H atom and the one adjacent to the surface, and ξ_2 is the distance between the middle H atom and the outer one. M is defined as

$$M = \frac{\xi_2}{\xi_1} \tag{3.1}$$

Table 3.3 lists the activation energy for the two channels, namely the separation channel and the dissociation channel, for various M-values. For the field of about 1.7V/Å the desorption occurs sideways; that is, the path is in between these two channels. Figs 3.20 to 3.24 give contour maps for the ground state energy surface as a function of z_1 and ξ_1 for different M-values and for different fields. The most stable configuration for H_3 onto W(111) is when M =0.75, for which the calculated energy of adsorption is about 2.0eV as comapred to 1.8eV (Ernst and Block[7]) and 3.0eV (Tsong and Kinkus[8]). The plots as presented in Figs 3.20 to 3.24 give a general feeling of H_3 adsorption and its field desorption. However, most likely there will be formation of H_2 and H (to be chemisorbed on the surface) pairs instead of all three H dissociating through the dissociation channel as considered above.

Table 3.3: Activation energy, Q, for various channels for H_3 (linear and upright) adsorption onto $W_4(111)$. z_1 is the separation of the closest H atom from the top W atom, ξ_1 is the distance between this H and the middle one, and M is the ratio of ξ_2 to ξ_1, where ξ_2 is the separation between the two H atoms farthest from the surface. Δq_1, Δq_2 and Δq_3 are the charges on the H atoms closest to the surface, the middle one and the farthest one, respectively, at the (local) minimum position.

M	F	Q(eV)			z_1^{min}	ξ_1^{min}	Δq_1	Δq_2	Δq_3
	(V/Å)	Separ. Chann.	Dissoc. Chann.	Sideways	(Å)	(Å)	(e)	(e)	(e)
0.7	0	2.0	3.3		1.61	1.24	-0.41	0.016	-0.1
	1.0	5.1	4.2		1.55	1.23	-0.32	-0.023	-0.02
	1.8			0.4	1.51	1.25	-0.23	-0.075	0.12
	2.0	--	--	--	--	--	--	--	--
0.8	0	2.0	3.0		1.61	1.14	-0.39	0.016	-0.15
	1.0	4.4	3.8		1.55	1.13	-0.31	-0.024	-0.044
	1.7			0.8	1.53	1.14	-0.23	-0.073	0.075
	1.8			0.4	1.54	1.14	-0.21	-0.08	0.11
0.9	0	1.8	2.6		1.63	1.06	-0.37	0.017	-0.2
	1.0	4.0	3.6		1.56	1.05	-0.28	-0.02	-0.094
	1.7			0.65	1.56	1.06	-0.21	-0.067	0.11
	1.8			0.25	1.56	1.06	-0.19	-0.072	0.15
1.0	0	1.7	2.5		1.64	1.01	-0.34	0.016	-0.26
	1.0	3.5	3.3		1.58	0.99	-0.26	-0.014	-0.12
	1.7			0.35	1.59	1.0	-0.18	-0.056	0.11
	1.8			0.05	1.6	1.0	-0.17	-0.051	0.19
1.1	0	1.4	2.3		1.67	0.96	-0.32	0.017	-0.32
	1.0	3.0	3.0		1.59	0.94	-0.24	-0.008	-0.16
	1.7			0.08	1.62	0.95	-0.16	-0.042	0.11
	1.8	--	--	--	--	--	--	--	--

The values are good to only two significant figures. However, these figures are retained for comparisions.

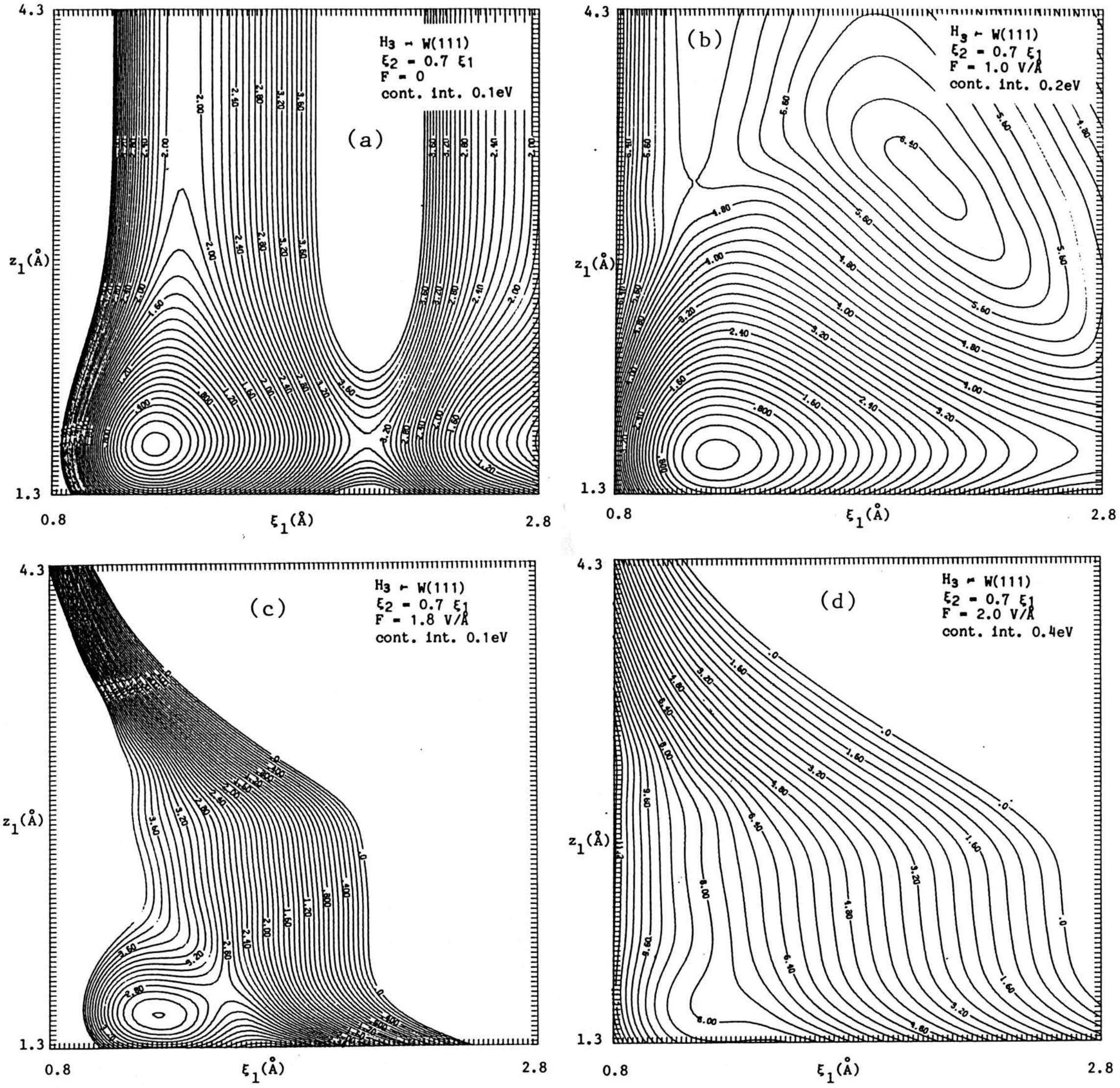

Fig.3.20: Contour plot of the ground-state energy surface of the linear and upright H_3 interacting with the W(111) surface (Config.1 of Fig.3.2) for various field strengths. z_1 is the distance between the surface atom and the closest H atom; ξ_1 is the distance between this H atom and the middle one, and ξ_2 is the distance between the middle H atom and the one farthest from the surface.

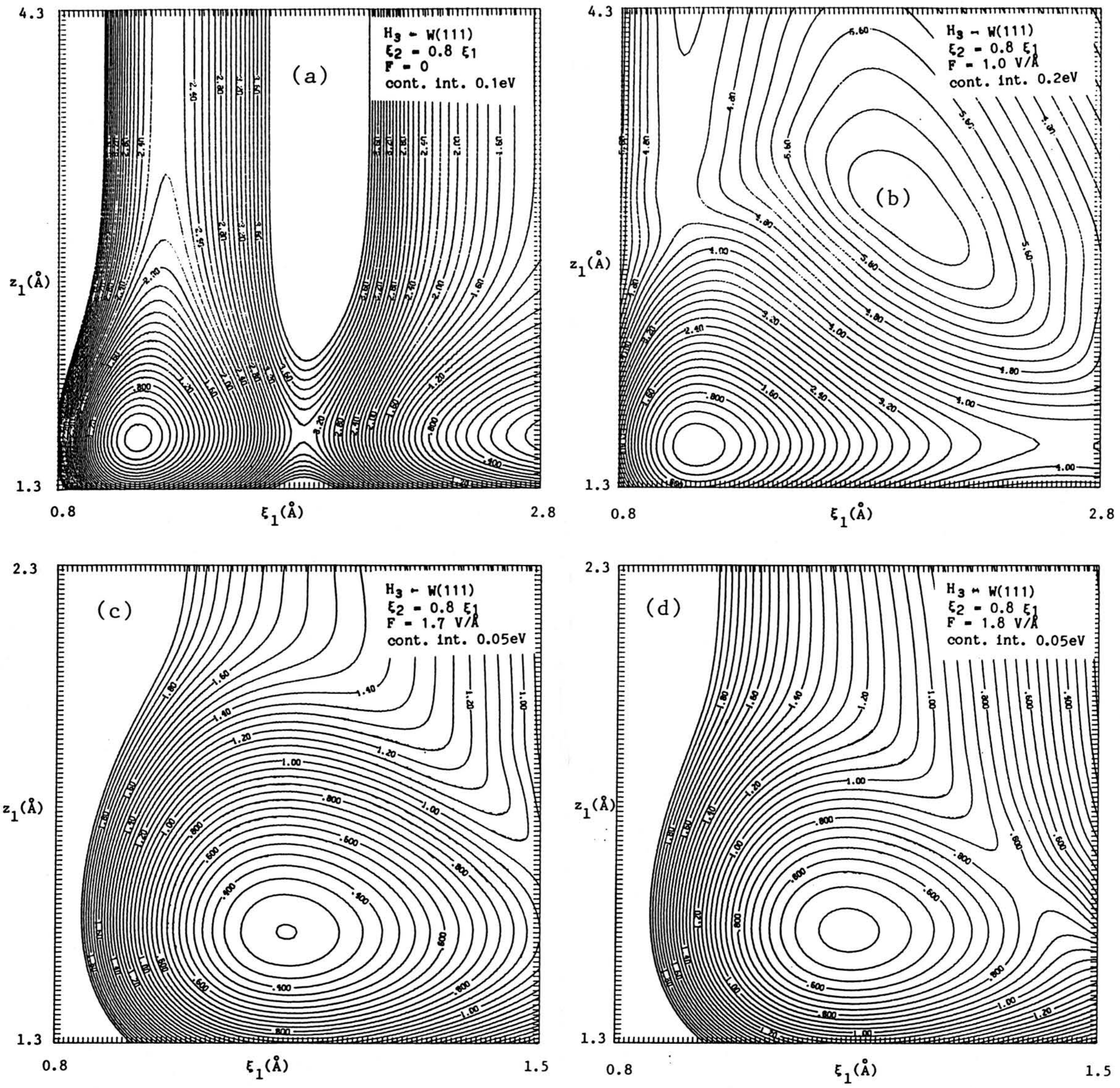

Fig.3.21: Same as Fig.3.2, but for $\xi_2 = 0.8\ \xi_1$.

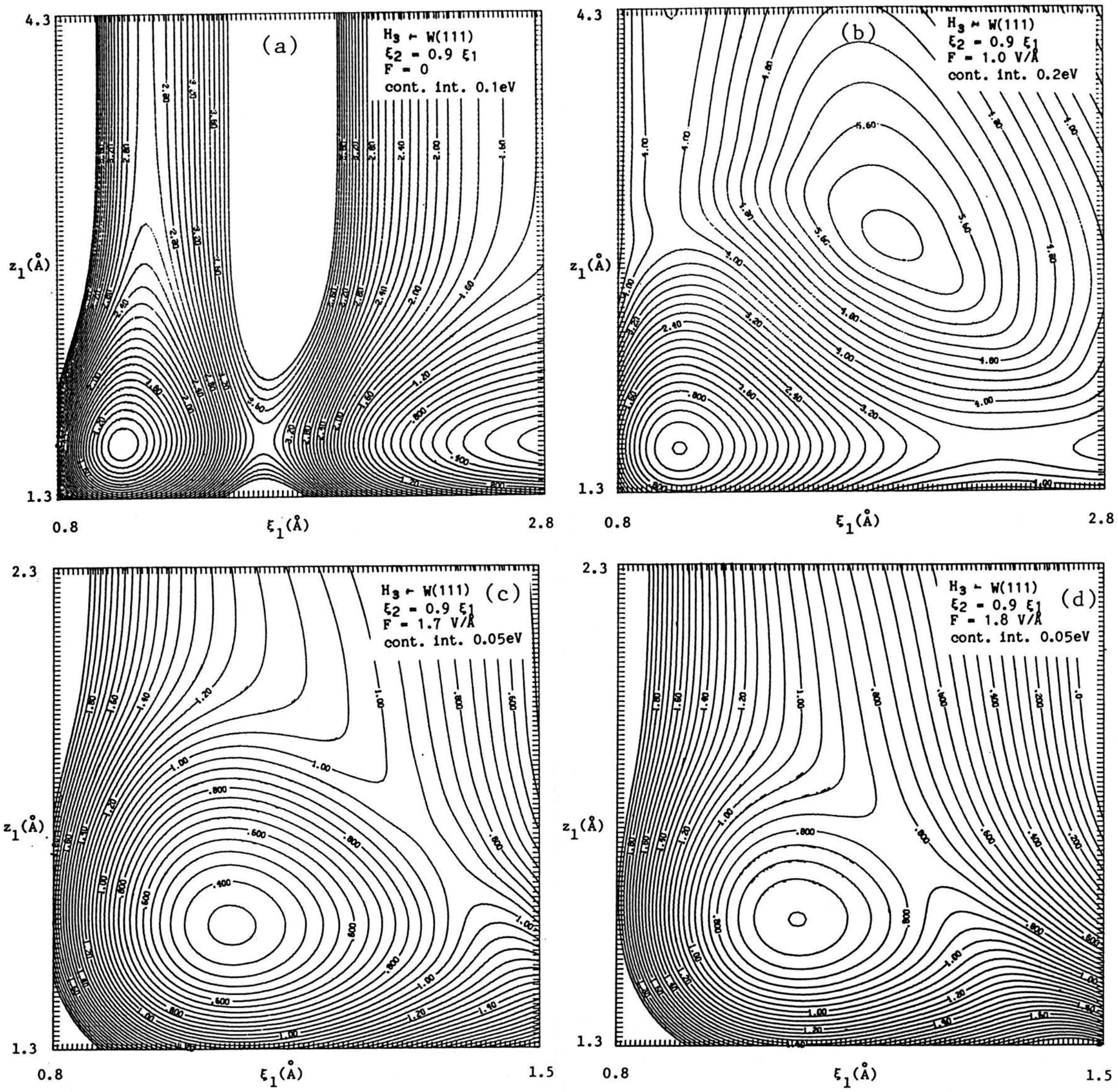

Fig.3.22: Same as Fig.3.2, but for $\xi_2 = 0.9\ \xi_1$.

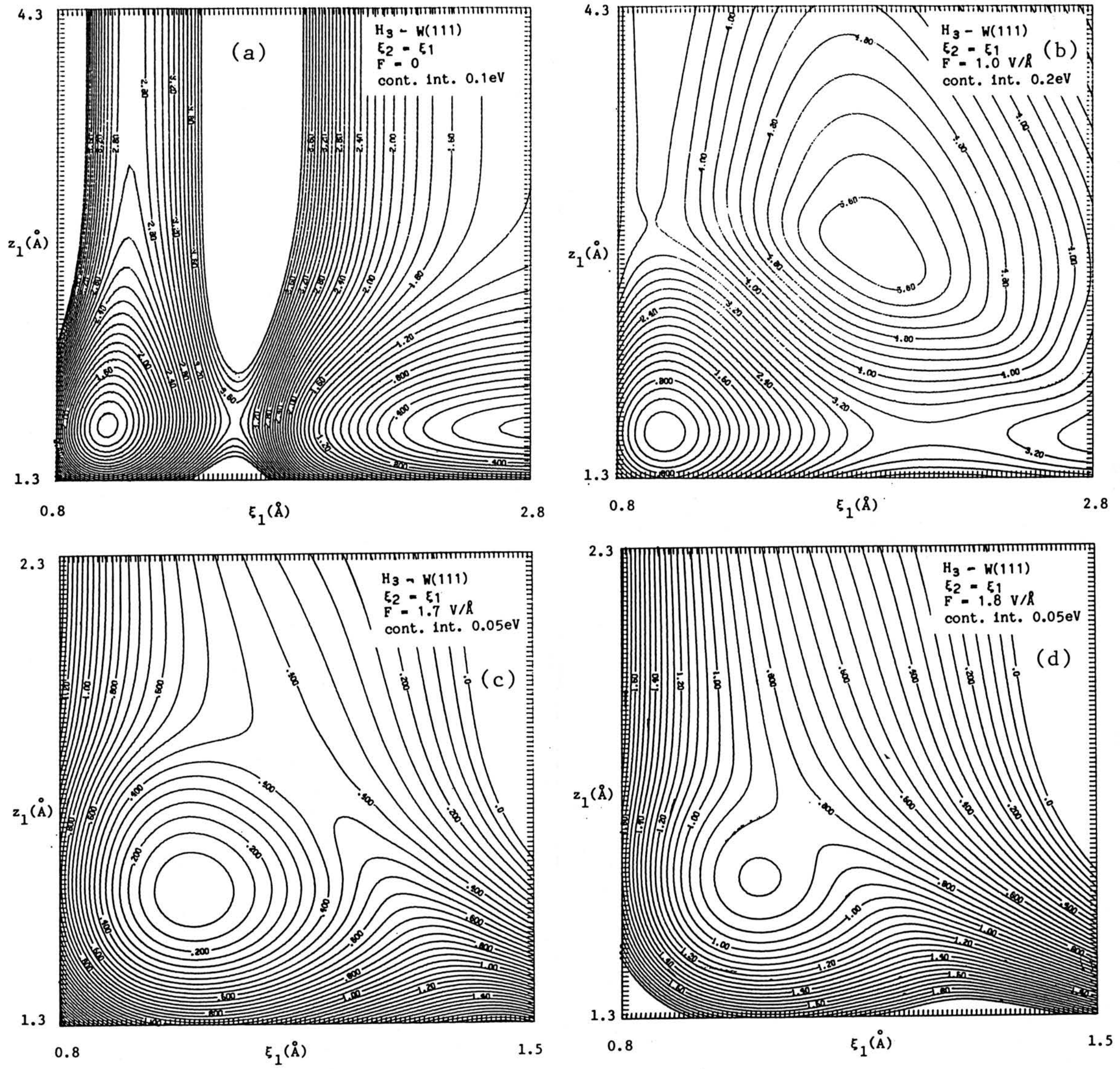

Fig.3.23: Same as Fig.3.2, but for $\xi_2 = \xi_1$.

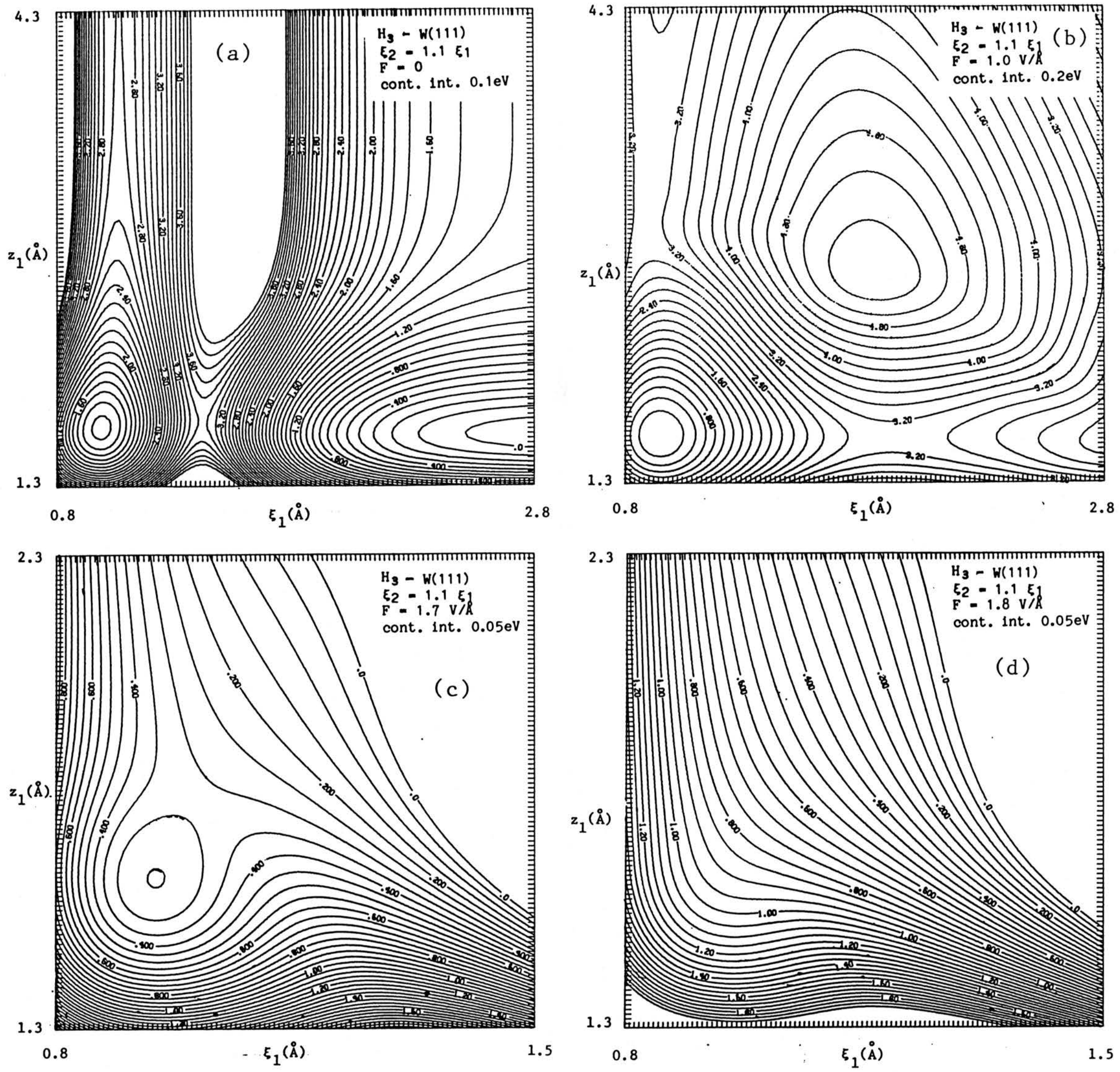

Fig.3.24: Same as Fig.3.2, but for $\xi_2 = 1.1\ \xi_1$.

CHAPTER IV

Field Evaporation:

The process of field desorption is commonly known as field evaporation when the desorbing particles are the metal ions themselves. In field ion microscopy, the field ion tip itself evaporates in very strong fields. The ASED-MO theory of Chapt.II.1 has been used to study the field evaporation properties of the tungsten metal. The effects of field penetration, Friedel oscillations and polarizations, as described in Sect.3 of Chapt.II, have been considered, as they are very important for a correct description of the phenomenon of field evaporation.

An electric field at the surface of the metal induces an excess charge which, by way of Poisson's equation, results in a spatially varying field that penetrates into the metal in an oscillatory way. In jellium model calculations one allows the electrons and the electric field to adjust self-consistently, keeping the ionic contribution smeared out as a uniform positive background. In a real metal, the ion cores in the surface region will, of course, also adjust their positions. They move inward (outward) if the excess surface charge leads to enhanced (decreased) occupation of bonding orbitals or to decreased (enhanced) occupation of antibonding orbitals. As the ion cores adjust their position, the electrons and the electric field have to follow in a self-consistent manner. This latter self-consistency can, unfortunately, not be accounted for in the jellium model calculations. The numerical cluster calculations below, however, indicate that the adjustment of the ion cores is minimal.

Experiments suggest that field evaporation of metal atoms most likely occurs at steps, kinks and edges, or for small clusters of atoms, on larger planes. Theory should calculate the electric field, the electron density, and the geometry of the ion cores for such configurations self-consistently. It is not presently possible to do this. To demonstrate, however, the interesting effects to be expected from such a calculation, the results of the cluster calculations are presented, in which the self-consistency requirement of the electric field has been neglected, and, rather, it has been again taken from the jellium model calculations.

In Fig.4.1, the energy of a W atom on the three-fold site of a tetrahedral W_4 cluster is plotted, with the electric field applied in the direction perpendicular to the plane containing the three atoms (compare with Fig.2.17). It is noted first that in the absence of a field the binding energy of the top-most W atom is about 6.8eV as compared to the experimental cohesive energy of 8.2eV per particle. (The position of the fourth atom nearest to the top W atom has been adjusted to give the correct equlibrium position of the top W atom with respect to the three W atoms of the tetrahederal in zero field.)

In Fig.4.2, the results of the calculation with polarization effects on the top-most W atom included or absent (see Sect.3c of Chapt.II) have been compared. Of significance is the fact that in all of these calculations, the equilibrium position of the top-most atom does not shift as a function of field strength. Note also that in any of these approximate schemes the activation barrier dissappears between 4 and about 7V/Å. It is felt that an attempt to fit the experimental data accurately by adjusting the local electric field would detract from the

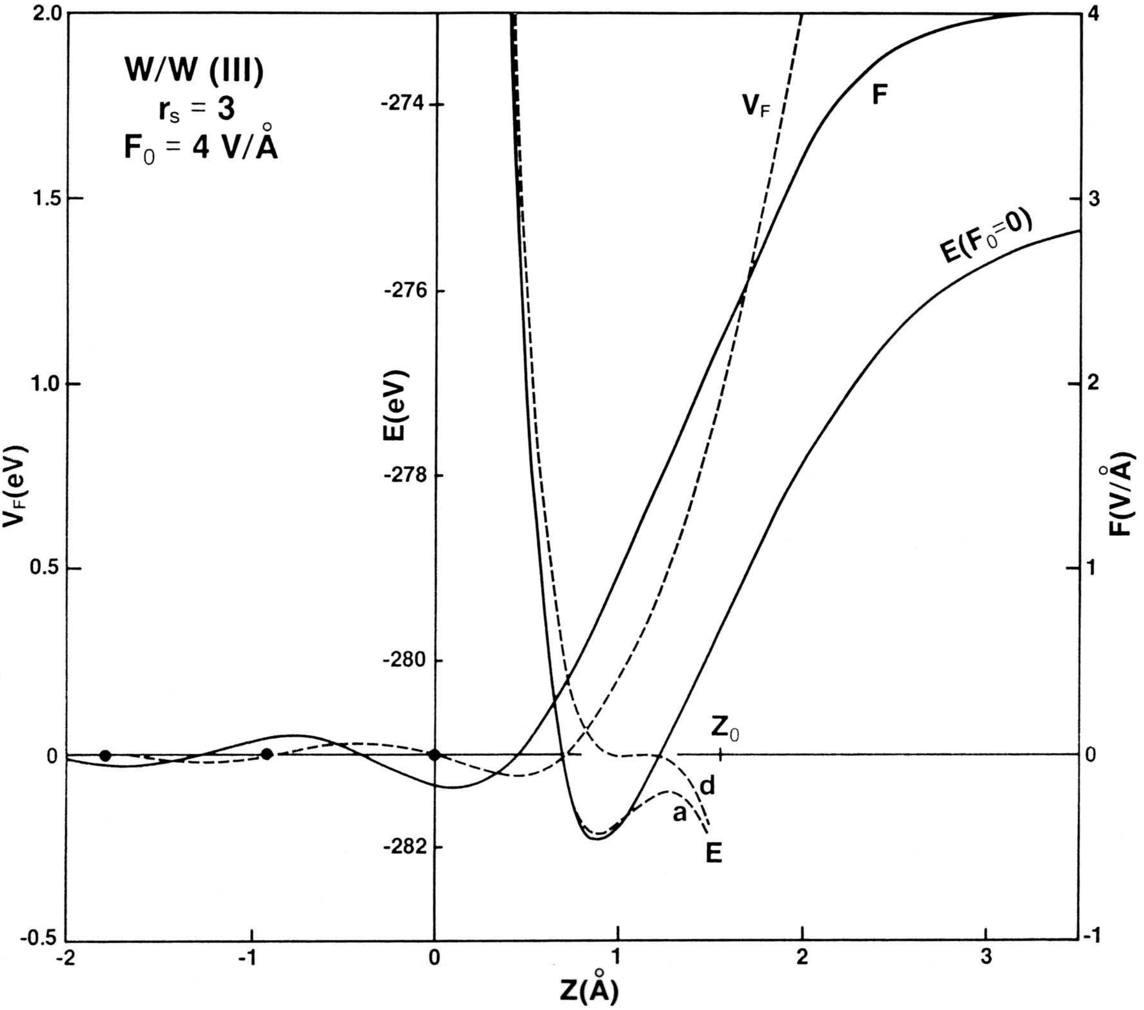

Fig.4.1: The inducing field, F, the associated field potential, V_F (defined in eqn.(2.12)), and the total energy, E, of the W cluster. Small circles denote the positions of the lattice planes parallel to the W(111) surface. z=0 corresponds to the second layer atoms. The surface atom is the desorbing atom involved in the field evaporation process. z_0 is the centre of the induced charge density for F_0=4v/Å. (a) and (d) denote the inclusion of different terms in the Hamiltonian, as described in Sect.3c. (See Figs 2.16 and 2.17 also.)

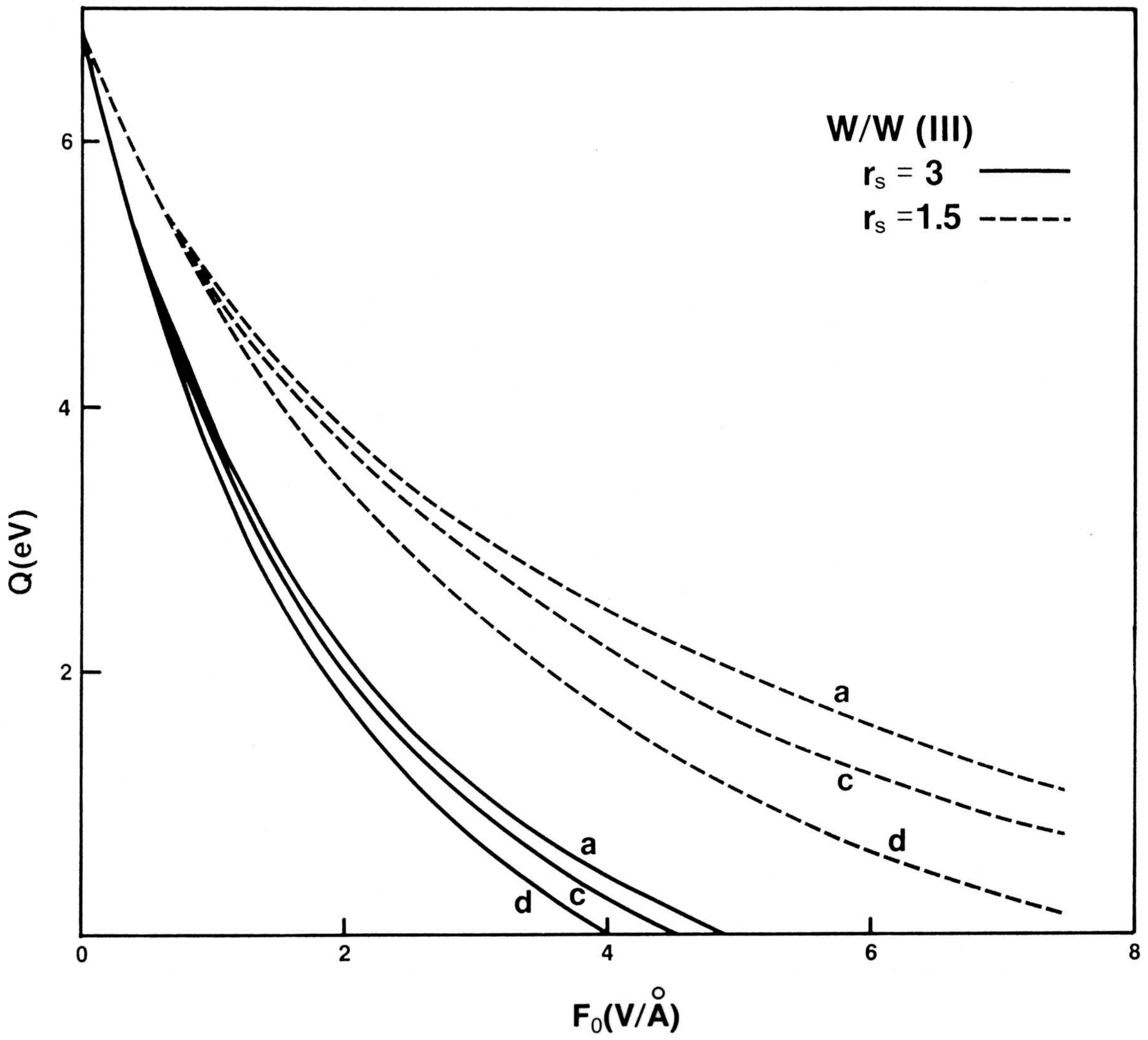

Fig.4.2: The activation energy Q for the W-W_4 cluster as a function of the field strengths, F_0 for two Wigner-Seitz radii. (See Fig.2.18 and Sect.3c of Chapt.II for the description of (a), (c) and (d)).

message of these model calculations, which is that a better and quantitative understanding of field adsorption and field evaporation can only come about once the local electric field at a field ion emission tip has been calculated microscopically and, above all, self-consistently with the local electron density and ion geometry.

Appendix A

Euler Angles and Rotation Operations

The Euler angles, (α,β,γ), refer to the following ordered operations on a set of coordinate axes: (1) rotation by an angle, α, about the z-axis; (2) rotation by an angle, β $(0\leqq\beta\leqq\pi)$, about the new y-axis; and (3) rotation by an angle, γ, about the new z-axis. This convention is called the y-convention, and is the one adapted to this work. (In the x-convention, one performs the second rotation about the new x-axis.) It should be noted that the polar coordinates θ,ϕ (with respect to the original frame) of the final rotated z-axis are identical with the Euler angles β,α, respectively. In other words, the rotation, carrying the polar-axis from its reference position to the ray or the direction defined by (θ,ϕ), has the Euler angles (ϕ,θ,x). Here x is arbitrary and, for simplicity, will always be set equal to zero.

In connection with the evaluation of the D - matrices, as appearing in eqn.(2.39), one frequently needs the Euler angles, (α,β,γ), which rotate the axial system. They are obtained according to the following scheme. Suppose a point has the polar coordinates (θ_1,ϕ_1) in the first axial system and (θ_2,ϕ_2) in the second. The first axial system is defined here as having the orientation given by the Euler angles, $(\alpha_1,\beta_1,\gamma_1) = (\phi_1,\theta_1,0)$, and the second as having the orientation given by $(\alpha_2,\beta_2,\gamma_2) =(\phi_2,\theta_2,0)$. The Euler angles, which take the axial system from the orientation $(\alpha_1,\beta_1,\gamma_1)$ to the orientation $(\alpha_2,\beta_2,\gamma_2)$, are (α, β, γ). Symbolically

$$(\alpha,\beta,\gamma)\ (\alpha_1,\beta_1,\gamma_1) = (\alpha_2,\beta_2,\gamma_2) \quad . \tag{A1}$$

The inverse operation is given according to the following scheme

$$(\alpha,\beta,\gamma)^{-1} = (\pi-\gamma,\beta,\pi-\alpha) \quad . \tag{A2}$$

(α,β,γ) are obtained in terms of $(\alpha_1,\beta_1,\gamma)$ and $(\alpha_2,\beta_2,\gamma_2)$, using the following set of equations:

$$\cos\beta = \cos\beta_1 \cos\beta_2 + \sin\beta_1 \sin\beta_2 \cos(\alpha_2-\alpha_1) \tag{A3}$$

$$\alpha = -\gamma_1 + \theta \tag{A4}$$

$$\gamma = \gamma_2 - \chi \tag{A5}$$

where θ and χ are given by the following set of equations:

$$\sin\theta = \frac{\sin\beta_2 \sin(\alpha_2-\alpha_1)}{\sin\beta} \tag{A6}$$

$$\cos\theta = \frac{-\sin\beta_1 \cos\beta_2 + \cos\beta_1 \sin\beta_2 \cos(\alpha_2-\alpha_1)}{\sin\beta} \tag{A7}$$

$$\sin\chi = \frac{\sin\beta_1 \sin(\alpha_2-\alpha_1)}{\sin\beta} \tag{A8}$$

$$\cos\chi = \frac{\cos\beta_1 \sin\beta_2 - \sin\beta_1 \cos\beta_2 \cos(\alpha_2-\alpha_1)}{\sin\beta} \tag{A9}$$

Using the pair of eqns (A6) and (A7), one can precisely know in which quadrant the value of θ lies. Similarly, the use of eqns (A8) and (A9) gives a single value of χ between 0 & 2π.

If $\sin\beta = 0$, eqns (A4) to (A9) are replaced by the following two equations:

$$\alpha = (\alpha_2-\alpha_1)\cdot\mathrm{sgn}(\cos\beta_1) \tag{A10}$$

$$\gamma = \gamma_2 - \gamma_1 \cos\beta \tag{A11}$$

Appendix B

d - Matrices and their Recursion Relations

The d - matrices, as defined in eqn.(2.42), are given by

$$d^{\ell}_{m\sigma}(t) = \frac{(\ell+m)!}{(\ell+\sigma)!} \left[\frac{1+t}{2}\right]^{\ell} \sum_{s} (-1)^{s+m} \binom{\ell-\sigma}{m+s} \binom{\ell+\sigma}{\ell-s} \left[\frac{1-t}{1+t}\right]^{s+(m+\sigma)/2} \quad ; m,\sigma \geqq 0 \qquad \text{(B1)}$$

To get the d - matrices for all possible combinations of +ve and -ve values of m and σ, one uses

$$d^{\ell}_{m\sigma}(t) = d^{\ell}_{-m,-\sigma}(t) = (-1)^{\ell+m+\sigma}\, d^{\ell}_{m,-\sigma}(-t) = (-1)^{\ell+m+\sigma}\, d^{\ell}_{-m\sigma}(-t) \qquad \text{(B2)}$$

The sum over s in eqn.(B1) includes all values for which the binomial coefficients are defined. The use of eqn.(B1) is very inefficient for computation, relative to recurrence relations, which hold for these d - matrices. One starts with

$$d^{o}_{oo}(t) = 1 \qquad \text{(B3)}$$

and

$$d^{1}_{oo}(t) = t \quad , \qquad \text{(B4)}$$

and finds $d^{\ell}_{m\sigma}(t)$ for all $\ell, m, \sigma \geqq 0$ using the following three equations :

$$d^{\sigma}_{m\sigma}(t) = \frac{(1-t)^{(\sigma-m)/2} \quad (1+t)^{(\sigma+m)/2}}{2^{\sigma} \quad (\sigma-m)!} \quad ; \sigma \geqq m \geqq 0 \qquad \text{(B5)}$$

$$d^{m}_{m\sigma}(t) = \frac{(-1)^{m-\sigma}\,(2m)!}{2^{m}\,(m+\sigma)!}\,(1-t)^{(m-\sigma)/2}\,(1+t)^{(m+\sigma)/2} \quad ;m \geqq \sigma \geqq 0 \qquad (B6)$$

$$\frac{(\ell+\sigma+1)(\ell-m+1)}{\ell+1}\,d^{(\ell+1)}_{m\sigma}(t) - (2\ell+1)\left[\ell - \frac{m\sigma}{\ell(\ell+1)}\right] d^{\ell}_{m\sigma}(t) + {}$$

$$+ \frac{(\ell-\sigma)(\ell+m)}{\ell}\,d^{(\ell-1)}_{m\sigma}(t) = 0 \quad ; (\ell-1) \geqq (m,\sigma) \geqq 0 \quad (B7)$$

Here $d^{\ell}_{m\sigma}(t)$ is defined as zero whenever $\ell<m$ or $\ell<\sigma$. Situations may arise where one can have $\sigma=m$ and $t=1$. In these cases the first term in the numerator of eqn.(B5) is defined as 1, or t is replaced by a number infinitesimally different from t.

Appendix C

The V - Functions and their Recurrence Relations

To obtain the $V^m_{n\ell j}(\delta,r,R)$, as given by eqn.(2.48), in a more amenable form, and to develop recurrence relations between them, extensive use is made of relations (2.45) and Fig.2.15. For brevity, the subscript a is dropped and, subsequently, the argument of the V - functions will also be omitted in this appendix. In certain limiting situations eqn.(2.48) may be integrated to give

$$V^o_{noo}(\delta,r,R) = \frac{1}{2rR\delta^2}\left[(\delta|R-r|)^{n+1} A_n(\delta|R-r|) - (\delta(R+r))^{n+1} A_n(\delta(R+r))\right] \quad (C1)$$

and

$$V^o_{ooj}(\delta,r,R) = (2j+1)\, k_j(\delta r_+)\, i_j(\delta r_-) \quad , \quad (C2)$$

where r_+ and r_- are the greater and lesser, respectively, of R and r. $k_j(x)$ and $i_j(x)$ are spherical Bessel functions and $A_n(x)$ is a function closely related to them. The following relations hold for these functions

$$\frac{2j+1}{x}\, i_j(x) = i_{j+1}(x) - i_{j-1}(x) \quad (C3)$$

$$\frac{2j+1}{x}\, k_j(x) = k_{j+1}(x) - k_{j-1}(x) \quad (C4)$$

with

$$\left.\begin{aligned} i_o(x) &= x^{-1}\sinh x \\ i_{-1}(x) &= -x^{-1}\cosh x \\ k_o(x) &= x^{-1} e^{-x} \\ k_{-1}(x) &= x^{-1} e^{-x} \end{aligned}\right] \quad . \quad (C5)$$

Also

$$A_n(x) = \frac{n}{x} A_{n-1}(x) + A_o(x) \quad (C6)$$

with
$$A_o(x) = x^{-1}\, e^{-x} \tag{C7}$$

For larger j values, eqn.(C3) fails to give correct values (on computation) for $i_j(x)$. Instead, a method due to Corbatò (Ref.34, Chap.II) is used and $i_j(x)$ is generated from higher to lower values by assuming that: (i) $i_{J+1}(x) = 0$ for sufficiently large J, and (ii) the ratio $r_J(x) = \frac{i_{J+1}(x)}{i_J(x)}$ is zero for this J (presently J has been set to 200). Using eqns (C3) and (C5), one gets

$$r_{j-1}(x) = \frac{-x}{2j + 1 - x\, r_j(x)} \tag{C8}$$

where
$$r_j(x) = \frac{i_{j+1}(x)}{i_j(x)} \quad . \tag{C9}$$

$r_j(x)$ is generated by downward recurrence until one reaches r_o. Then, starting from the computationally convenient formula for i_o,

$$i_o(x) = \frac{e^{|x|}}{1 + |x| - x\, r_o(x)} \tag{C10}$$

one succesively determines the $i_j(x)$ for increasing j by use of the previously obtained $r_j(x)$ values (using eqn.(C8)) and eqn.(C9)

Using eqns (C2) and (C10), one can obtain a relatively simple recurrence relation for V^o_{ooj} :

$$V^o_{oo,j+1} = \frac{2j+3}{x_+} V^o_{ooj}\, r_j(x_-) + \frac{2j+3}{2j-1} V^o_{oo,j-1}\, r_j(x_-)\, r_{j-1}(x_-) \quad , \tag{C11}$$

with
$$V^o_{ooo} = \frac{e^{-x_1}}{x_+\,(1 + x_+ - x_-\, r_1(x_-))} \tag{c12}$$

$$V^o_{oo1} = 3 \left[\frac{e^{-x_1}}{x_+} + \frac{e^{-x_1}}{x_+^{\,2}} \right] \frac{r_1(x_-)}{1 + x_- - x_-\, r_1(x_-)} \tag{C13}$$

$$\left.\begin{array}{l} x_+ = \delta\, r_+ \quad ;\ (x_+ \neq 0) \\ x_- = \delta\, r_- \\ x_1 = \delta\, |R-r| \\ x_2 = \delta\, (R+r) \end{array}\right] \tag{C14}$$

The recurrence relations for V^o_{noo} are

$$V^o_{n+1,oo} = (n+1)\, V^o_{noo} + \frac{x_1^{\,n+1}\, e^{-x_1} - x_2^{\,n+1}\, e^{-x_2}}{2\,\delta^2\, r\, R} \tag{C15}$$

with $$V^o_{ooo} = \frac{1}{2\,\delta^2\, r\, R}\, [e^{-x_1} - e^{-x_2}] \;. \tag{C16}$$

Both expressions (C12) and (C16), although completely different in form, give the same value for V^o_{ooo}.

As mentioned earlier, using relations (2.45) and Fig.2.15, one can have various recurrence relations holding true for the V - functions for all possible values of n, ℓ, m and j .(Note that $V^m_{n\ell j} = V^{-m}_{n\ell j}$, from eqns (2.34) and (2.48)). Those needed for present purposes are :

$$V^m_{n+2,\ell j} = \delta^2(R^2+r^2)V^m_{n\ell j} + 2\delta^2 rR\left[\frac{j-m}{2j-1}\, V^m_{n\ell,j-1} + \frac{j+m+1}{2j+3}\, V^m_{n\ell,j+1}\right] \tag{C17}$$

$$\frac{\ell-m+1}{2\ell+1}\, V^m_{n+1,\ell+1,j} + \frac{\ell+m}{2\ell+1}\, V^m_{n+1,\ell-1,j} =$$
$$= \delta R\, V^m_{n\ell j} + \delta r\left[\frac{j-m}{2j-1}\, V^m_{n\ell,j-1} + \frac{j+m+1}{2j+3}\, V^m_{n\ell,j+1}\right] \tag{C18}$$

$$V^{m+1}_{n+1,\ell-1,j+1} - V^{m+1}_{n+1,\ell+1,j+1} =$$
$$= (2\ell+1)\, \delta R\, \left[\frac{1}{2j+5}\, V^m_{n\ell,j+2} - \frac{1}{2j+1}\, V^m_{n\ell j}\right] \tag{C19}$$

$$\frac{2m-1}{\delta R}\, V^{m-1}_{n,m-1,j} = (n-m)\, V^{m}_{n-1,mj} - V^{m}_{nmj} \tag{C20}$$

$$\begin{aligned}\frac{2m-1}{\delta R}\left[V^{m-1}_{n,m-1,j} + V^{m-1}_{n+1,m-1,j}\right] &= \\ &= (n-m)\left[V^{m}_{nmj} + V^{m}_{n-1,m,j}\right] - V^{m}_{n+1,mj}\end{aligned} \tag{C21}$$

$$\begin{aligned}\frac{1}{\delta^2 Rr} V^{m}_{n+1,mj} &= -(n-m)\left[\frac{1}{2j+3} V^{m}_{n-1,m,j+1} - \frac{1}{2j-1} V^{m}_{n-1,m,j-1}\right] + \\ &+ \left[\frac{1}{2j+3} V^{m}_{nm,j+1} - \frac{1}{2j-1} V^{m}_{nm,j-1}\right]\end{aligned} \tag{C22}$$

$$V^{m}_{m+1,mj} = -\frac{2m-1}{\delta R}\left[V^{m-1}_{m,m-1,j} + V^{m-1}_{m+1,m-1,j}\right] \tag{C23}$$

and

$$\begin{aligned}\frac{R^2+r^2}{rR}\, V^{m}_{nmj} &= -\frac{2j+m+n+3}{2j+3}\, V^{m}_{nm,j+1} + \frac{n+m+1-2j}{2j-1}\, V^{m}_{nm,j-1} + \\ &+ \frac{1}{2j+3}\, V^{m}_{n+1,m,j+1} - \frac{1}{2j-1}\, V^{m}_{n+1,m,j-1}\end{aligned} \tag{C24}$$

Appendix D

Clebsch-Gordan Coefficients

The Clebsch-Gordan coefficients, as used in eqn.(2.57), are determined from the properties of the associated Legendre function (2.34). For these coefficients

$$C_{\mu jk}^{\sigma\tau} = C_{\mu kj}^{\tau\sigma} = C_{\mu jk}^{-\sigma,-\tau} \quad . \tag{D1}$$

Note that $C_{\mu jk}^{\sigma\tau} = 0$ if $j < |\sigma|$, if $k < |\tau|$, if $\mu < |\tau-\sigma|$, if $\mu+j+k$ is not even, or if $|j-k| \leqq \mu \leqq |j+k|$ is not satisfied. However, relatively simple combinations of μ, j, k, σ and τ are required for the present purposes, as is evident from eqn.(2.71). They are

$$C_{o\sigma\sigma}^{\sigma\sigma} = \frac{(2\sigma)!}{2\sigma+1} \tag{D2}$$

$$C_{ojj}^{\sigma\sigma} = \frac{2j-1}{j-\sigma}\,\frac{j+\sigma}{2j+1}\,C_{o,j-1,j-1}^{\sigma\sigma} \quad . \tag{D3}$$

Appendix E

Abscissae and Weights of Lobatto Quadrature :

The Lobatto Quadrature formula (Ref.35, Chap.II) of order n for an integral (normalized to the interval (-1,1)) is

$$\int_{-1}^{1} f(x)\,dx = H_{1n}\, f(-1) + \sum_{k=2}^{n-1} H_{kn}\, f(x_{kn}) + H_{nn}\, f(+1) \tag{E1}$$

where the abscissae x_{kn} are the zeroes of the first derivative of the Legendre polynomial of order n-1, i.e. they are solutions to the equation

$$\frac{d}{dx} P_{n-1}(x) = 0 \quad . \tag{E2}$$

The weight coefficients H_{kn} are given by

$$H_{kn} = \frac{2}{n(n-1)} \left[P_{n-1}(x_{kn}) \right]^{-2} \tag{E3}$$

The formula (E1) is exact for all polynomials f(x) of degree $\leqq 2n-3$. This can be written in an alternative and symmetric form as

$$\int_{-1}^{1} f(x)\,dx = H_{-m,n}\, f(-1) + \sum_{k=-m+1}^{m-1} H_{kn}\, f(x_{kn}) + H_{mn}\, f(+1) \tag{E4}$$

with $x_{-k,n} = -\, x_{kn}$ and $H_{-k,n} = H_{kn}$. For odd n, n=2m+1, and for even n, n=2m. The positive abscissae x_{kn} and the corresponding weights H_{kn} are given in Table E1 for n=64. The weight coefficients satisfy the sum rule

$$\sum_{k=-m}^{m} H_{kn} = 2 \quad . \tag{E5}$$

Table E1: The abscissae and the corresponding weights of the Lobatto quadrature for n=64 (from Ref.35, Chap.II).

Abscissae	Weights
1.000000000000	0.000496031746
0.998179871502	0.003056008245
0.993902726703	0.005496016204
0.987192676603	0.007921289790
0.978066662831	0.010327002367
0.966547110369	0.012707399197
0.952662235789	0.015056683988
0.936446027476	0.017369116385
0.917938173510	0.019639040723
0.897183967846	0.021860903512
0.874234200658	0.024029268144
0.849145034543	0.026138828614
0.821977867308	0.028184422666
0.792799181826	0.030161044499
0.761680383408	0.032063857058
0.728697625089	0.033888203884
0.693931621291	0.035629620524
0.657467450313	0.037283845460
0.619394346138	0.038846830538
0.579805480068	0.040314750882
0.538797732717	0.041684014251
0.496471456936	0.042951269834
0.452930232232	0.044113416447
0.408280611290	0.045167610126
0.362631859226	0.046111271084
0.316095686196	0.046942090027
0.268785974019	0.047658033802
0.220818497497	0.048257350376
0.172310641088	0.048738573122
0.123381111650	0.049100524408
0.074149647946	0.049342318477
0.024736727622	0.049463363621

Appendix F

Computational Details

The position, where the potential for an electron is required, is chosen as the origin, and with respect to this point, say P, the spherical polar coordinates (R_a,Θ_a,Φ_a) and (R_b,Θ_b,Φ_b) of the atoms A and B, respectively, are obtained. These angles give $(\alpha_a,\beta_a,\gamma_a)$ and $(\alpha_b,\beta_b,\gamma_b)$, where γ_a and γ_b are arbitrary and are presently set to zero. (However, the final results have been checked to be independent of the choice of γ_a and γ_b.) Thus $(\alpha_{ab}, \beta_{ab}, \gamma_{ab})$ are obtained easily (see Appendix A) and are stored in a common block to be passed over to other subroutines and functions where they are required. For the present purposes, the number of Clebsch-Gordan coefficients required is $3(j_{max}+1)$, where j_{max} is the number where one wants to stop summing the infinite series in eqn.(2.81) or (2.83). It turns out that the choice of $j_{max} = 25$ gives numerical results good up to at least three significant figures. For large R_a and R_b (> 10 Å), the convergence is not good and one needs j_{max} greater than 25. The numerical results have been tested by obtaining the simple overlap integrals, i.e. without $\frac{1}{r}$ term in the integrand of eqn.(2.32). The Clebsch-Gordan coefficients are also put in a common block. Similarly, the rotation d-matrices and other functions, not including r, are calculated before integration is performed and are put in a common block. The V-functions depend on r and these are the only functions, combined with some simple polynomial of r, are calculated in a function program over which integration is performed.

For a particular r, the V-functions are generated using recurrence relations (Appendix C) for all possible values of m, n, ℓ and j, and then summations over σ, τ and j are performed before integration is done. In the whole operation, the most time consuming step is the calculation of the V-functions. During the integration process, these V-functions are calculated several times for both R_a and R_b and for several values of r. For the electron-potential (2.29), one needs to calculate about 2000 multi-centre Coulomb integrals of type (2.32). Among these 2000-odd integrals there will be some having the same value, depending on the choice of the axial frame, but to keep track of these and put them back into the calculations is a formidable task and is subject to error. Thus they are all calculated systematically. (The matrix, containing these integrals, is symmetric about the diagonal.)

To make the whole operation feasible and more efficient at the cost of a little less accuracy, integration is performed using Lobatto quadrature of the order 64. This is done after making a transformation by a change of variable to the limit (-1,1).

Once it was decided to use the Lobatto quadrature for the integration, the V-functions were calculated for 62 values of r (the two end points are excluded since the integrand is zero at these points) for all values of R (R_a, R_b, etc., depending on the number of atoms in the cluster), m, n, ℓ and j, and stored in computer's memory. The V-functions are symmetric for ± m. It turns out that, for the present purposes of a rare gas atom on the near tetrahedral structure of W_4 one needs to store (letting V go to V')

$$V'(3,4,26,3,62)$$

where the first index corresponds to three possible magnetic quantum numbers for the d-orbitals; the second index is for the combination of n, the principal quantum number and the Slater exponent, δ (remembering that there are two values of δ for the contracted d-orbitals for tungsten). The number 26 is equal to $j_{max}+1$. (j_{max} is 25 in the present case.) The next number, 3, gives the possible values of R (due to the symmetry of the W-cluster) with respect to the point P, where the electron-potential is needed. Finally, the number 62 corresponds to the different values of $r_k = \frac{1+y_k}{1-y_k}$ (k=2 to 63) for which the V are calculated for the Lobatto quadrature method (see eqn.(2.83)).

Lastly, the coefficients C appearing in eqn.(2.29), and which are the outcome of the diagonalization of the ASED-MO hamiltonian, are evaluated using the new coordinate system, where the origin coincides with the point P.

Appendix G

Electric Field and the associated Field Energy

For an asymptotic field of F_0=5V/Å, the width, Ω, of the induced surface charge density for r_s=3 is the same as the width in a weak field for r_s=2 (refer to Tables 2.3 and 2.4). In the absence of further information, one may assume that the nature of the induced surface charge densities for these two configurations is similar, i.e., the wavelength, λ, and the relative heights of the Friedel oscillations are the same, except that now z_0 is taken as given in Table 2.3. This induced surface charge density can then be approximated reasonably well as

$$\rho(z) \propto \frac{\sin(kz)}{z} \qquad \text{for} \quad -\infty < z < z_0 \tag{G1}$$

where $k = \frac{2\pi}{\lambda}$. Thus, using Poisson's equation, the field between $-\infty$ and z_0 can be given as

$$F(k,z) = \frac{F_0}{c'} \int_{-\infty}^{kz} \frac{\sin(kz')}{kz'}\, d(kz') \qquad ; \quad z < z_0 \tag{G2}$$

where the constant, c', in the above equation is obtained from the fact that $F(k,z_0)$ is half its maximum value, F_0. i.e.,

$$\frac{F_0}{2} = \frac{F_0}{c'} \int_{-\infty}^{kz_0} \frac{\sin(kz')}{kz'}\, d(kz') \tag{G3}$$

giving

$$c' = 2 \int_{-\infty}^{kz_0} \frac{\sin(kz')}{kz'}\, d(kz') \quad . \tag{G4}$$

Because of the Friedel oscillations on the metal side, the peak, z_p, of the induced surface charge density is shifted towards the metal from its centre of mass z_0. Eqn.(G2) can be written as

$$F(k,z) = \frac{F_0}{c'} \left[\int_{-\infty}^{kz_p} \frac{\sin(kz')}{kz'}\, d(kz') + \int_{kz_p}^{kz} \frac{\sin(kz')}{kz'}\, d(kz') \right] \tag{G5}$$

or,

$$F(k,z) = \frac{F_0}{c'} \left[\frac{\pi}{2} + \mathrm{Si}(kz-kz_p) \right] \quad . \tag{G6}$$

For other field strengths, it is assumed that λ and (z_0-z_p) are proportional to the corresponding Ω (as given in Table 2.3). λ and z_p thus obtained are given in Table G1, together with z_0 and Ω for the W(111) surface, taking $r_s = 3$.

Using eqn.(2.12), the field potential is given as

$$V_F(\mathbf{r}) = V_F(z) = \frac{e}{k} \int_{-\infty}^{kz} F(k,z')\, d(kz') \quad . \tag{G7}$$

In the above equation, $F(k,z)$ can again be approximated by $c''\frac{\sin(kz)}{kz}$. The prefactor, c'', is determined by minimizing the variation in V_F for the different choices of z_c (see below). Thus one can write

$$V_F(z) = \frac{e}{k} \left[\int_{-\infty}^{kz_c} F(k,z')\, d(kz') + \int_{kz_c}^{kz} F(k,z')\, d(kz') \right] \approx$$

$$\approx \frac{eF_0}{kc'} \left[1.1 \int_{-\infty}^{kz_c-\frac{\pi}{2}} \frac{\sin(kz')}{kz'} d(kz') + \int_{kz_c}^{kz} \left[\frac{\pi}{2} + \mathrm{Si}(kz'-kz_p) \right] d(kz') \right] =$$

$$= \frac{eF_0}{kc'} \left[1.1 \left[\frac{\pi}{2} + \mathrm{Si}(kz_c - \frac{\pi}{2} - kz_p) \right] + \int_{kz_c}^{kz} \left[\frac{\pi}{2} + \mathrm{Si}(kz'-kz_p) \right] d(kz') \right] \tag{G8}$$

for $-\infty < z < z_c$, with z_c a reasonably large negative (say $z_c \sim -2\lambda$).

Table G1: The centre of mass, z_0, the peak, z_p, the width, Ω, and the wavelength, λ, of the induced surface charge density for the W(111) surface, taking $r_s = 3$, for various inducing fields, F_0. $z = 0$ corresponds to the surface atoms.

F_0(V/Å)	z_0(Å)	z_p(Å)	Ω(Å)	λ(Å)
1	0.96	0.39	1.80	1.94
3	0.69	0.15	1.70	1.83
4	0.61	0.09	1.66	1.78
5	0.51	-0.01	1.64	1.76

The values are good to only two significant figures. However, these figures are retained for comparisions and computations.

For $z > z_0$, a convenient analytic form is adopted for the field:

$$F(z) = \frac{F_0}{1 + \exp(-\frac{z-z_0}{z_1})} \quad ; \; z > z_0 \, . \tag{G9}$$

This field results from an induced surface charge density

$$\rho(z) = \frac{1}{4\pi}\frac{dF}{dz} = \frac{1}{4\pi}\frac{F_0}{4z_1\cosh^2(\frac{z-z_0}{2z_1})} \tag{G10}$$

with centre of mass at z_0 and width, λ, given by

$$\lambda = 4z_1\cosh^{-1}\sqrt{2} = 3.5255 \; z_1 \tag{G11}$$

The field potential corresponding to the field (G9) is

$$V_F(z) = eF_0z_1\left[\frac{z-z_0}{z_1} + \ln\left[1 + \exp(-\frac{z-z_0}{z_1})\right]\right] \, . \tag{G12}$$

Both eqns (G6) and (G9) give the same value for the field, F, at $z = z_0$, which is $\frac{F_0}{2}$. The field potentials, as obtained using eqns (G8) and (G12), can be matched at $z = z_0$ by adjusting z_1 in eqn.(G12). F and V_F thus obtained are plotted in Fig.2.16 for F_0 = 1, 3 and 5 V/Å. The unrealistic, small kinks around $z = z_0$ in the F-curves, as a result of the matching of the two functions, have been smoothed out.

Appendix H

Matrix elements of the operator z^q between different orbitals

Using eqns (2.33), (2.34) and (2.36), the matrix element of the operator z (= $r\cos\theta$, for the z-axis as taken to be the polar axis) between 1s and $2p_z$ orbitals of He can be written as:

$$\langle 1s|z|2p_z;m=0\rangle = \int \psi_{1s}^{He}(\mathbf{r})^{*} \; z \; \psi_{(2p_z)}^{He}(\mathbf{r}) \; d^3\mathbf{r} =$$

$$= N(1,0,0,\delta_s)N(2,1,0,\delta_p)\int\int\int e^{-(\delta_s+\delta_p)r} \; r^4 \sin\theta \; \cos\theta \; d\theta d\phi dr \; P_1^0(\cos\theta) =$$

$$= \sqrt{\frac{3}{16\pi^2}\;\frac{(2\delta_s)^3\,(2\delta_p)^5}{2!\;4!}} \int_0^{2\pi} d\phi \int_0^{\infty} e^{-(\delta_s+\delta_p)r} \; r^4 dr \int_{-1}^{1} P_1^0(y) y dy =$$

$$= 32(\delta_s+\delta_p)^{-5} \; \delta_s^{3/2} \; \delta_p^{5/2} \quad . \qquad \text{(H1)}$$

The values of δ_s and δ_p are given in Table 2.1. Various matrix elements of z^q have been calculated, between the He orbitals, in a similar way, and are given in Table H1. It should be noted that the matrix elements of z^q are zero unless the following selection rules are satisfied:

$$\Delta m = |m_i - m_j| = 0$$

$$\Delta \ell = |\ell_i - \ell_j| = 2k \text{ for even } q, \text{ and } 2k+1 \text{ for odd } q;\; k=0,1,2,\cdots \qquad \text{(H2)}$$

For tungsten, it should be noted that the exponential terms in the 5d orbital expansions are replaced by

$$e^{-\delta_d r} = C_1 e^{-\delta_1 r} + C_2 e^{-\delta_2 r} \quad . \qquad \text{(H3)}$$

The normalized coefficients C_1 and C_2 are obtained from the unnormalized c's (Ref.24, Chap.II) as follows

Table H1: The matrix elments of z^q for the He orbitals.

	q=1 (Å)	q=2 (Å^2)	q=3 (Å^3)	q=4 (Å^4)
$\langle 1s\|z^q\|2p_z;m=0\rangle$	0.57983	0	1.0949	0
$\langle 1s\|z^q\|1s\rangle$	0	0.35117	0	0.55493
$\langle 2p_x;m=1\|z^q\|2p_x;m=1\rangle$	0	0.76531	0	2.3428
$\langle 2p_y;m=-1\|z^q\|2p_y;m=-1\rangle$	0	0.76531	0	2.3428
$\langle 2p_z;m=0\|z^q\|2p_z;m=0\rangle$	0	2.2959	0	11.714

Table H2: The matrix elments of z^q for the W orbitals.

	q=1 (Å)	q=2 (Å^2)	q=3 (Å^3)	q=4 (Å^4)
$\langle 6s\|z^q\|6s\rangle$	0	2.1745	0	11.223
$\langle 6p_x;m=1\|z^q\|6p_x;m=1\rangle$	0	2.6849	0	20.370
$\langle 6p_y;m=-1\|z^q\|6p_y;m=-1\rangle$	0	2.6849	0	20.370
$\langle 6p_z;m=0\|z^q\|6p_z;m=0\rangle$	0	8.0548	0	101.85
$\langle 5d_{x^2-y^2};m=2\|z^q\|5d_{x^2-y^2};m=2\rangle$	0	0.50744	0	1.3220
$\langle 5d_{z^2};m=0\|z^q\|5d_{z^2};m=0\rangle$	0	1.8606	0	11.898
$\langle 5d_{xy};m=-2\|z^q\|5d_{xy};m=-2\rangle$	0	0.50744	0	1.3220
$\langle 5d_{xz};m=1\|z^q\|5d_{xz};m=1\rangle$	0	1.5223	0	6.6101
$\langle 5d_{yz};m=-1\|z^q\|5d_{yz};m=-1\rangle$	0	1.5223	0	6.6101
$\langle 6s\|z^q\|6p_z;m=0\rangle$	1.3568	0	8.5101	0
$\langle 6p_z;m=0\|z^q\|5d_{z^2};m=0\rangle$	0.84587	0	8.0551	0
$\langle 6p_x;m=1\|z^q\|5d_{xz};m=1\rangle$	0.73254	0	3.4880	0
$\langle 6p_y;m=-1\|z^q\|5d_{yz};m=-1\rangle$	0.73254	0	3.4880	0
$\langle 6s\|z^q\|5d_{z^2};m=0\rangle$	0	1.3315	0	9.7746

$$C_1 = \frac{c_1}{\sqrt{c_1{}^2 + c_2{}^2 + 2c_1c_2\left[\frac{4\delta_1\delta_2}{(\delta_1+\delta_2)^2}\right]^{11/2}}} , \tag{H4}$$

with a similar expression for C_2. For W atoms, the various Slater exponents and the normalized C's are given in Table 2.1. To calculate the matrix elements of z^q between the W orbitals, the procedure is the same as described above for the He atom. Some of the typical matrix elements are

$$\langle 6p_z;m=0|z|5d_{z^2};m=0\rangle =$$

$$= 4\sqrt{\frac{11}{5}}\,(2\delta_p)^{13/2}\left[C_1(2\delta_1)^{11/2}(\delta_p+\delta_1)^{-13} + C_2(2\delta_2)^{11/2}(\delta_p+\delta_2)^{-13}\right] \tag{H5}$$

$$\langle 6s|z^2|5d_{z^2};m=0\rangle =$$

$$= 13\text{x}2^{14}\sqrt{\frac{11}{15}}\,\delta_s{}^{13/2}\left[C_1\delta_1{}^{11/2}(\delta_s+\delta_1)^{-14} + C_2\delta_2{}^{11/2}(\delta_s+\delta_2)^{-14}\right] \tag{H6}$$

$$\langle 6s|z^2|6s\rangle = \frac{182}{3}(2\delta_s)^{-2} \tag{H7}$$

$$\langle 5d_{xy};m=-2|z^2|5d_{xy};m=-2\rangle =$$

$$= \frac{270336}{7}\left[C_1^2\delta_1^{11}(2\delta_1)^{-13} + C_2^2\delta_2^{11}(2\delta_2)^{-13} + 2C_1C_2(\delta_1\delta_2)^{11/2}(\delta_1+\delta_2)^{-13}\right] \tag{H8}$$

Various matrix elements of z^q have been calculated in a similar way and the results are shown in Table H2.

REFERENCES:

Introduction:

1. K. Nath, Z. W. Gortel and H. J. Kreuzer, Van der Waals interaction of rare gases and hydrogen on semiconductor surfaces, Surf. Sci. **155** (1985) 596.
2. K. Nath, H. J. Kreuzer and A. B. Anderson, Field adsorption of rare gases, Surf. Sci. (1986) (in press).
3. H. J. Kreuzer and K. Nath, Field adsorption and evaporation, J. de Physique (1986) (in press).
4. K. Nath and H. J. Kreuzer, Field evaporation, (to be published).
5. K. Nath, H. J. Kreuzer and J. H. Block, Field adsorption of H_2 and H_3, (to be published).
6. Cz. Koziol, K. Faulian, E. Bauer, H. J. Kreuzer and K. Nath, Imaging of densely packed planes and rows by field ionization via adsorbed atoms, Surf. Sci. **169** (1986) 275.

Chapter I:

1. H. J. Kreuzer and Z. W. Gortel, Physisorption Kinetics, in Springer Series in Surface Sciences, Vol.1 (Springer-Verlag, Berlin, 1986).
2. G. Benedek and U. Valbusa, Eds, Dynamics of Gas Surface Interaction (Springer-Verlag, Berlin, 1982).
3. H. Hoinkes, Rev. Mod. Phys. **52** (1980) 933.
4. M. Cardillo, Ann. Rev. Phys. Chem. **32** (1981) 331
5. J. R. Smith, Ed., Theory of Chemisorption (Springer-Verlag, Berlin, 1980).
6. I. E. Dzyaloshinskii, E. M. Lifshitz and L. P. Pitaevskii, Adv. Phys. **10** (1961) 165.
7. D. Langbein, Theory of Van der Waals Attraction, in Springer Tracts in Modern Physics, Vol.72 (Springer-Verlag, Berlin, 1974).
8. C. Mavroyannis, Mol. Phys. **6** (1963) 593.
9. G. G. Kleiman and U. Landman, Phys. Rev. B **8** (1973) 5484.
10. A. D. McLachlan, Mol. Phys. **7** (1964) 381.
11. L. W. Bruch and H. Watanabe, Surf. Sci. **65** (1977) 619.

12. G. Vidali and M. W. Cole, Surf. Sci. **107** (1981) L374; **110** (1981) 10.

13. R. B. Laughlin, Phys. Rev. B **25** (1982) 2222.

14. L. D. Landau and E. M. Lifshitz, Statistical Physics, Part 1 (Pergamon Press, Oxford, 1980), Sect.123.

15. F. C. Jahoda, Phys. Rev. **107** (1957) 1261.

16. H. R. Philipp and E. A. Taft, Phys. Rev. **113** (1959) 1002.

17. M. Aven, D. T. F. Marple and B. Segall, J. Appl. Phys. **32** Suppl. (1961) 2261.

18. H. Ehrenreich, H. R. Philipp and J. C, Phillips, Phys. Rev. Lett. **8** (1962) 59.

19. H. R. Philipp and H. Ehrenreich, Phys. Rev. Lett. **8** (1962) 92.

20. D. Brust, J. C. Phillips and F. Bassani, Phys. Rev. Lett. **9** (1962) 94.

21. H. R. Philipp and H. Ehrenreich, Phys. Rev. **129** (1963) 1550; in Optical Properties of III - V compounds, Semiconductors and Semimetals, Vol.3, R. K. Willardson and A. C. Beer, Eds (Academic Press, N. Y.,1967).

22. M. Cardona and D. L. Greenaway, Phys. Rev. **131** (1963) 98.

23. W. J. Scouler and G. B. Wright, Phys. Rev. **133** (1964) A736.

24. M. Cardona and D. L. Greenaway, Phys. Rev. **133** (1964) A1685.

25. M. Cardona and G. Harbeke, Phys. Rev. **137** (1965) A1467.

26. M. Cardona, M. Weinstein and G. A. Wolff, Phys. Rev. **140** (1965) A633.

27. M. Cardona, J. Appl. Phys. **36** (1965) 2181.

28. F. H. Pollak in II - IV Semiconducting Compounds, D. G. Thomas, Ed. (Benjamin, 1967), p.552.

29. M. Cardona, in Optical Properties of Solids, S. Nudelman and S. S. Mitra, Eds (Plenum, 1969), p.137.

30. M. Cardona and R. Haensel, Phys. Rev. B **1** (1970) 2605.

31. W. Gudat, E. E, Koch, P. Y. Yu, M. Cardona and C. M. Penchina, Phys. Stat. Solidi (b) **52** (1972) 505.

32. D. J. Chadi, J. P. Walter, M. L. Cohen, Y. Petroff and M. Balkanski, Phys. Rev. B **5** (1972) 3058.

33. J. L. Freeouf, Phys. Rev. B **7** (1973) 3810.

34. M. Grynberg, R. LeToullec and M. Balkanski, Phys. Rev. B **9** (1974) 517.

35. A. Manabe, H. Noguchi and A.Mitsuishi, Phys. Stat. Solidi (b) **90** (1978) 157.

36. A. Rodzik and A. Kisiel, J. Phys. C **16** (1983) 203.

37. D. M. Roessler, Brit. J. Appl. Phys. **16** (1965) 1359.

38. E. O. Kane, J. Phys. Chem. Solids **1** (1957) 249; in Band Theory and Transport Properties, Handbook on Semiconductors, Vol.1, W. Paul, Ed. (North Holland, 1982), p.193.

39. H. Arwin, D. E. Aspnes and D. R. Rhiger, J. Appl. Phys. **54** (1983) 7132.

40. L. Viña, C. Umbach, M. Cardona and L. Vodopyanov, Phys Rev. B **29** (1984) 6752.

41. D. J. Chadi and R. M. White, Phys. Rev. B **11** (1975) 5077.

42. J. R. Chelikowsky and M. L. Cohen, Phys. Rev. B **14** (1976) 556.

43. M. Podgórny and M. T. Czyżyk, Solid State Comm. **32** (1979) 413.

44. M. T. Czyżyk and M. Podgórny, Phys. Stat. Solidi (b) **98** (1980) 507.

45. C. S. Wang and B. M. Klein, Phys. Rev. B **24** (1981) 3417.

46. K. C. Hass, H. Ehrenreich and B. Velický, Phys. Rev. B **27** (1983) 1088.

47. W. Szuszkiewicz, A. M. Witowski and M. Grynberg, Phys. Stat. Solidi (b) **87** (1978) 637.

48. D. E. Aspnes and A. A. Studna, Phys. Rev. B **27** (1983) 985.

49. C. J. Summers and J. G. Broerman, Phys. Rev. B **21** (1980) 559.

50. D. Sherrington and W. Kohn, Phys. Rev. Lett. **21** (1968) 153.

51. W. Bardyszewski, J. Phys. Chem. Solids **44** (1983) 813.

52. D. M. Roessler, Brit. J. Appl. Phys. **16** (1965) 1119.

53. D. M. Roessler, Brit. J. Appl. Phys. **17** (1966) 1313.

54. W. J. Scouler, Phys. Rev. **178** (1969) 1353.

55. P. O. Nilsson and L. Munkby, Phys. Kondens. Materie **10** (1969) 290.

56. B. W. Veal and A. P. Paulikas, Phys. Rev. B **10** (1974) 1280.

57. R. K. Ahrenkiel, J. Opt. Soc. Am. **61** (1971) 1651.

58. L. D. Landau and E. M. Lifshitz, Electrodynamics of Continuous Media (Pergamon, 1960), p.259,282.

59. H. Bode, Network Analysis and Feedback Amlifier Design (Van Nostrand Company, Inc., Princeton, 1945).

60. P. W. Langhoff and M. Karplus, J. Chem Phys. **53** (1970) 233.

61. P. W. Langhoff and M. Karplus, J. Opt. Soc. Am. **59** (1969) 863.

62. L. Salem, Mol. Phys. **3** (1960) 441; C. Mavroyannis and M. J. Stephen, ibid. **5** (1962) 629; K. T. Tang, J. Chem. Phys. **49** (1968) 4727.

63. L. W. Bruch, Surf. Sci. **125** (1983) 194.

64. S. Rauber, J. R. Klein, M. W. Cole and L. W. Bruch, Surf. Sci. **123** (1982) 173.

65. P. Esser and W. Göpel, Surf. Sci. **97** (1980) 309.

66. H. J. Dresser, T. E. Madey and J. T. Yates Jr., Surf. Sci. **42** (1974) 533.

Chapter II:

1. E. W. Müller and T. T. Tsong, Progr. Surface Sci. **4** (1973) 1.

2. T. T. Tsong and E. W. Müller, Phys. Rev. Lett. **25** (1970) 911; J. Chem. Phys. **55** (1971) 2884.

3. R. G. Forbes and M. K. Wafi, Surf. Sci. **93** (1980) 12.

4. R. G. Forbes, Progr. Surface Sci. **10** (1980) 249; Vacuum **31** (1981) 567.

5. T. T. Tsong, Surf. Sci. **140** (1984) 377.

6. W. A. Steele, The Interaction of Gases with Solid Surfaces (Pergamon, New York, 1974).

7. E. Zaremba and W. Kohn, Phys. Rev. B **15** (1977) 1769.

8. E. W. Müller, Phys. Rev. **102** (1956) 618.

9. R. Gomer and L. W. Swanson, J. Chem. Phys. **38** (1963) 1613.

10. R. Haydock and D. R. Kingham, Surf. Sci. **103** (1981) 239; Surf. Sci. **104** (1981) L194; J. Phys. B **14** (1981) 385.

11. D. R. Kingham, Surf. Sci. **116** (1982) 273.

12. D. R. Kingham, H. H. H. Homeier, C. M. C. de Castilho, Surf. Sci. **152/153** (1985) 55.

13. L. M. Kahn and S. C. Ying, Solid State Commun. **16** (1975) 799; Surf. Sci. **59** (1976) 333.

14. D. Tomanek, H. J. Kreuzer and J. H. Block, Surf. Sci. **157** (1985) L315.

15. A. B. Anderson and R. G. Parr, J. Chem. Phys. **53** (1970) 3375.

16. A. B. Anderson, J. Chem. Phys. **60** (1974) 2477.

17. A. B. Anderson, J. Chem. Phys. **62** (1975) 1187.

18. A. B. Anderson, J. Chem. Phys. **63** (1975) 4430.

19. K. Yates, Hückel Molecular Orbital Theory (Academic Press, New York, 1978).

20. D. W. Bullet, in Solid State Physics, Advances in Research and Applications, Vol.35, H. Ehrenreich, F. Seitz and D. Turnbull, Eds (Academic Press, New York, 1980).

21. J. P. Lowe, Quantum Chemistry (Academic Press, Orlando, 1978), Chap.10.

22. R. Hoffmann, J. Chem. Phys. **39** (1963) 1397; **40** (1964) 2047, 2474, 2480, and 2745.

23. W. Lotz, J. Opt. Soc. Am. **60** (1970) 206; C. E. Moore, Atomic Energy Levels, Natl. Bur. Std., Circ. 467 (U. S. Govt. Printing Office, Washington, 1958).

24. E. Clementi and D. L. Raimondi, J. Chem. Phys. **38** (1963) 2686; H. Basch and H. B. Gray, Theoret. Chim. Acta (Berlin) **4** (1966) 367; J. W. Richardson, W. C. Nieuwpoort, R. R. Powell and W. F. Edgell, J. Chem. Phys. **36** (1962) 1057.

25. R. G. Gordon and Y. S. Kim, J. Chem. Phys. **56** (1972) 3122, and references therein.

26. P. J. Feibelman, Progr. Surface Sci. **12** (1982) 287.

27. W. Schmickler and D. Henderson, Phys. Rev. B **30** (1984) 3081.

28. P. Gies and R. R. Gerhardts, Phys. Rev. B **31** (1985) 6843; **33** (1986) 982.

29. J. P. Hobson, CRC Critical Review in Solid State Sciences **4** (1974) 221.

30. R. S. Mulliken, J. Chem. Phys. **23** (1955) 1833, 1841, 2338, and 2343.

31. F. E. Harris and H. H. Michels, J. Chem. Phys. **43** (1965) S165; **45** (1966) 116; Adv. Chem. Phys. **13** (1967) 205; F. E. Harris, Rev. Mod. Phys. **35** (1963) 558.

32. See, for example, A. R. Edmonds, Angular Momentum in Quantum Mechanics (Princeton University Press, Princeton, 1960), Chap.4; M. E. Rose, Elementary Theory of Angular Momentum (John Wiley, N. Y., 1957), Chap.4.

33. See, for example, G. Arfken, Mathematical Methods for Physicists (Academic Press, N.Y.,1970), Chap.11-12.

34. F. J. Corbató, J. Chem. Phys. **24** (1956) 452.

35. P. Rabinowitz, Math. Comp. **14** (1960) 47; H. H. Michels, ibid. **17** (1963) 237.

36. P. Hohenberg and W. Kohn, Phys. Rev. **136** (1964) B864; W. Kohn and L. J. Sham, ibid. **140** (1965) A1133.

37. N. D. Lang and W. Kohn, Phys. Rev. B **3** (1971) 1215; **7** (1973) 354.

Chapter III:

1. E. W. Müller, in Methods of Surface Analysis, A. W. Czanderna, Ed. (Elsevier, Amsterdam, 1975); E. W. Müller and T. T. Tsong, Field Ion Microscopy (American Elsevier, N. Y., 1969).
2. J. P. Lowe, Quantum Chemistry (Academic Press Inc., Orlando, 1978), Chap.10.
3. H. J. Kreuzer and Z. W. Gortel, Physisorption Kinetics, in Springer Series in Surface Sciences, Vol.1 (Springer-Verlag, Berlin, 1986), Chap.9.
4. F. C. Tompkins, Chemisorption of Gases on Metals (Academic Press, London, 1978), Sect.27.
5. B. Liu, J. Chem. Phys. **58** (1973) 1925.
6. P. Siegbahn, J. Chem. Phys. **68** (1978) 2457.
7. N. Ernst and J. H. Block, Phys. Rev. B **29** (1984) 7092.
8. T. T. Tsong and T. J. Kinkus, Phys. Rev. B **29** (1984) 529.